This is a non-peer reviewed preprint submitted to *EarthArXiv*

Source Representation and Earthquake-Ocean Coupling in Tsunami Generation by the 2020 Samos Normal-Faulting Earthquake

Fabian Kutschera[1], **Alice-Agnes Gabriel**[1,2]

[1]Institute of Geophysics and Planetary Physics, Scripps Institution of Oceanography, University of California San Diego, La Jolla, USA
[2]Department of Earth and Environmental Sciences, Ludwig-Maximilians-Universität München, Munich, Germany

Key Points:

- We compare tsunami generation from an instantaneous Okada source, one-way linked kinematic and dynamic ruptures, and full coupling.
- After 50 s, time-dependent models agree within 0.1 m in water deeper than 100 m, whereas a static source yields smaller tsunami crests.
- Fully coupled models resolve early near-source seismo-acoustic waves, whereas one-way linking efficiently models the large-scale tsunami.

Corresponding author: Fabian Kutschera, fkutschera@ucsd.edu

Abstract

The 2020 M_W 7.0 Samos normal-faulting earthquake produced damaging ground shaking and a destructive local tsunami. We construct a three-dimensional kinematic rupture model from a finite-fault inversion and use its shear stress changes to inform two dynamic rupture models. We initialize a non-linear shallow-water tsunami simulation with instantaneous Okada displacement and source one-way linked simulations with evolving seafloor deformation from the kinematic and dynamic rupture models. Fully coupled three-dimensional earthquake-tsunami simulations resolve rupture and elastic, acoustic, and gravity waves together. The coupled sea surface wavefield contains the developing tsunami, dispersive oceanic Rayleigh waves, first-mode ocean acoustic waves, and signals consistent with dispersive Scholte waves. We track crests and troughs over time as the respective means of the most extreme 0.1 percent of positive and negative sea surface height anomalies. For each time-dependent source, following transient seismo-acoustic waves, the one-way linked and fully coupled models agree within 0.10 m on both metrics from 50 to 360 s in water deeper than 100 m. At 6 min, all models share a leading drawdown with trough metrics near −0.5 m, whereas the instantaneous Okada source yields a crest metric of 0.35 m, compared with 0.5–0.6 m for time-dependent sources. Instantaneous sourcing, common in hazard assessment, may therefore underestimate tsunami crests from moderate normal-faulting earthquakes. The preferred dynamic rupture source captures the main tsunami periods at Syros, with larger tide gauge mismatches elsewhere. At Samos, full coupling resolves the early near-source seismo-acoustic wavefield, whereas time-dependent one-way linking provides an efficient estimate of the large-scale tsunami.

Plain Language Summary

Offshore earthquakes can move the seafloor and generate tsunamis, yet the first minutes of tsunami generation are challenging to constrain. We study the 2020 Samos normal-faulting earthquake in the Aegean Sea by comparing models that represent the earthquake source and ocean response with different levels of complexity. All models of the tsunami agree closely on its leading wave drawdown. A simpler model that applies the final seafloor displacement all at once produces a peak tsunami crest about a third smaller. A more complex three-dimensional simulation coupling the solid Earth with the water in a single simulation shows how sound and seismic waves travel through the ocean and along the seafloor, in addition to the tsunami. These waves overlap with the developing tsunami near the source, so early sea-level measurements may record signals beyond the tsunami itself. Our results show why modeling complexity should be matched to the scientific question: full coupling is valuable near the earthquake source, whereas simpler methods can efficiently simulate tsunami propagation farther away.

1 Introduction

Normal faulting earthquakes have increasingly been recognized as capable of generating destructive tsunamis across various tectonic settings: in outer-rise regions, this tsunamigenic potential has been demonstrated by the 1933 M_W 8.4 Sanriku earthquake in the Japan Trench (Kanamori, 1971), the 1977 M_W 8.3 Sumba earthquake along the Sunda Trench (Spence, 1986; Lynnes & Lay, 1988), and the 2010 M_W 7.4 Bonin Islands earthquake along the Izu-Bonin-Mariana system (Cheng et al., 2026). Outer-rise normal faults continue to present complex tsunami hazards offshore Japan (Lay et al., 2011; Obana et al., 2018; Baba et al., 2020) and other regions, such as the Central American subduction zone (Álvarez-Gómez et al., 2012). Beyond the outer rise, forearc normal faults may host tsunamigenic earthquakes (Bécel et al., 2017; Philippon et al., 2024). This hazard extends to submerged low-angle normal faults, which can produce tsunamigenic coseismic subsidence despite an unfavorable orientation for slip (Cummins et al., 2020; Biemiller et al., 2023).

However, (1) normal-faulting tsunamigenesis remains comparatively understudied relative to subduction zone events (e.g., Bilek & Lay, 2018), and (2) normal-faulting earthquakes have distinct, shallow rupture dynamics because the free surface alters rupture propagation on dipping faults (Oglesby et al., 1998). To investigate how normal-faulting source complexity affects the tsunami excitation, we turn to the Aegean Sea region, which is subject to active tectonic deformation (e.g., Taymaz et al., 2007; Reilinger et al., 2010; Royden & Papanikolaou, 2011). Situated between the Eurasian, African, and Anatolian plates (Fig. 1a; Bird, 2003), the Aegean Sea microplate is characterized by back-arc extension and crustal stretching (e.g., Sachpazi et al., 2016; Meng et al., 2021). This extension has resulted in frequent moderate-to-large earthquakes that regularly trigger local and regional tsunamis, such as the 1949 M_W 6.7 Chios earthquake (Altinok et al., 2005; Melis et al., 2020) and the 2017 M_W 6.6 Bodrum–Kos earthquake (Karasözen et al., 2018; Dogan et al., 2019; Ganas et al., 2019). The largest tsunami in the Aegean Sea in the 20th century was triggered by the 1956 M_W ∼7.7 Amorgos earthquake (Papadopoulos & Pavlides, 1992; Beisel et al., 2009; Okal et al., 2009; Leclerc et al., 2024). Yet, the extent to which rupture dynamics contribute to tsunami excitation in these normal-faulting events remains poorly understood.

The focus of this study is the 2020 M_W 7.0 Samos earthquake, a normal-faulting event in the Aegean Sea that generated a larger-than-expected tsunami (e.g., Hu et al., 2022). The event itself occurred close to the island of Samos in the eastern Aegean Sea (Fig. 1b), was the deadliest earthquake in 2020 (Mavroulis et al., 2022), causing 119 fatalities and widespread structural damage in Greece and Turkey, and generated a damaging local tsunami (Triantafyllou et al., 2021; Dogan et al., 2021; Kalligeris et al., 2022). The earthquake source characteristics, kinematic rupture process, and fault geometry have been analyzed using regional strong ground motion waveforms, teleseismic, and geodetic data (e.g., Cetin et al., 2020; Chousianitis & Konca, 2021; Lentas et al., 2021; Akinci et al., 2021; Taymaz et al., 2022).

Several studies analyzed the 2020 Samos tsunami propagation using finite-fault earthquake models and shallow water equation (SWE) tsunami simulations. Heidarzadeh et al. (2021) identified long-lasting tsunami oscillations due to basin effects, and Hu et al. (2022) further investigated how local tsunami resonance contributed to the unusually large tsunami height. C. Ren et al. (2022) inverted for time-dependent (kinematic) slip on a two-segment-fault geometry, sourcing linear SWE tsunami simulations. Sun et al. (2024) performed a joint inversion of high-rate GNSS, strong ground motion, and InSAR data to obtain kinematic slip on a single north-dipping fault plane and performed tsunami simulations using 2D depth-averaged, non-linear SWE. Using elastic dislocation theory (Okada, 1985) to describe the earthquake source, they investigated how bathymetry resolution affects tsunami duration and amplitude. Taymaz et al. (2022) explored the rupture dynamics of the 2020 Samos earthquake in a simplified full-space model, excluding free-surface effects.

Whereas tsunami simulations typically use instantaneous sources based on the Okada method (Levin & Nosov, 2015; Saito, 2019; Løvholt et al., 2026), differences between static (instantaneous), kinematic (time-dependent with prescribed spatio-temporal evolution of slip), and dynamic rupture (time-dependent, spontaneous rupture) earthquake sources have increasingly been investigated to better understand tsunami generation complexity (e.g., Z. Ren et al., 2019; Kutschera, Gabriel, et al., 2024; Sementsov et al., 2025; Melgar, 2026; Behrens, 2026). With fully-coupled earthquake-tsunami simulations (Maeda & Furumura, 2013), we can simultaneously solve for the elastic wave propagation in the solid Earth, as well as oceanic acoustic and gravity (i.e., tsunami) wave generation. This tsunami modeling technique has been applied for different types of sources in various tectonic settings (Maeda et al., 2013; Noguchi et al., 2016; Lotto et al., 2018; Du & Ma, 2025; Wirp et al., 2026; Henneking et al., 2026), but, to the best of the authors' knowledge, not yet to a predominantly normal-faulting dynamic rupture source.

In this study, we analyze the tsunami generation of the 2020, M_W 7.0 Samos normal-faulting earthquake by systematically increasing the modeled complexity of tsunami generation. We compare four types of tsunami simulations, based on (i) instantaneous sourcing with non-linear SWE, (ii) a kinematic, time-dependent earthquake model combined with non-linear SWE, (iii) a dynamic rupture model similarly linked to the non-linear SWE, and (iv) 3D fully-coupled earthquake dynamic rupture and tsunami simulations. To enable this comparison, we develop 3D dynamic rupture simulations of the Samos earthquake with bathymetry and topography, which are informed by a prior kinematic source inversion (Plicka et al., 2022) and produce realistic ground motions. The dynamic rupture models break bilaterally and up-dip, before transitioning into unilateral, westward rupture. We validate the simulated ground motions against observed, near-field peak ground velocities. The spontaneous rupture models showcase the sensitivity of peak ground motion to different assumptions on the spatial distribution of initial normal stress and rupture dynamics. In fully-coupled dynamic rupture-tsunami simulations, which capture the physically consistent tsunami generation, we observe large amplitudes of seismo-acoustic waves, including oceanic Rayleigh waves, signals consistent with Scholte waves, and ocean acoustic modes during the tsunami generation. Comparing static, kinematic, and dynamic sources for tsunami generation, we observe close agreement in the tsunami leading wave behavior, and closely matching tsunami extrema between time-dependent one-way linked and fully coupled tsunami simulations. Tsunami trough extrema from the instantaneous sourcing are driven by the source timing, whereas smaller peak crests for the Okada model persist despite the timing difference. In addition, trailing waves are affected by the tsunami modeling technique, which we interpret as a consequence of 3D frequency dispersion and water-column low-pass filtering of shorter-wavelength seafloor deformation.

2 Methods

Following the workflow illustrated in Fig. 2, this section is structured as follows: We first introduce the modeling software used in this study (Section 2.1), before we describe the reference finite-fault model (Section 2.2) used to constrain the fault geometry for all earthquake rupture simulations and slip for the kinematic source simulation. Next, we detail the 3D kinematic rupture model setup (Kinematic Rupture Model A) in Section 2.3 and the 3D dynamic rupture setup (Dynamic Rupture Models B & C; Table 1) in Section 2.4. In Section 2.5, we describe non-linear shallow water versus fully coupled tsunami modeling techniques. Although our simulations extend beyond the near field, our analysis focuses on the tsunami generation phase. We conclude with details on the computational mesh (Section 2.6).

2.1 Modeling software used in this study

In this study, we use the open-source software SeisSol (`https://github.com/SeisSol`; Gabriel et al., 2025) to simulate 3D kinematic rupture (Section 2.3), dynamic rupture (Section 2.4), and fully-coupled earthquake-tsunami models (Section 2.5.1). SeisSol is based on the arbitrary high-order derivative discontinuous Galerkin method (ADER-DG; e.g., Käser & Dumbser, 2006; Dumbser & Käser, 2006). Here, high-order time integration together with high-order space discretization and local time stepping (Breuer et al., 2016) provides high-order accuracy for modeled time-dependent ground motions (Käser et al., 2008; Pelties et al., 2012). SeisSol has been verified against community benchmark problems, including a recent 3D fully-coupled setup (e.g., Pelties et al., 2014; R. A. Harris et al., 2018; Kutschera et al., 2025), and validated in dynamic rupture scenarios of varying scale and complexity (e.g., Uphoff et al., 2017; Ulrich, Gabriel, et al., 2019).

In addition to fully-coupled tsunami simulations with SeisSol, we use the open-source software GeoClaw (`https://github.com/clawpack/geoclaw`; Clawpack Development Team, 2024) for tsunami simulations (Section 2.5.2). GeoClaw is a subset of Clawpack

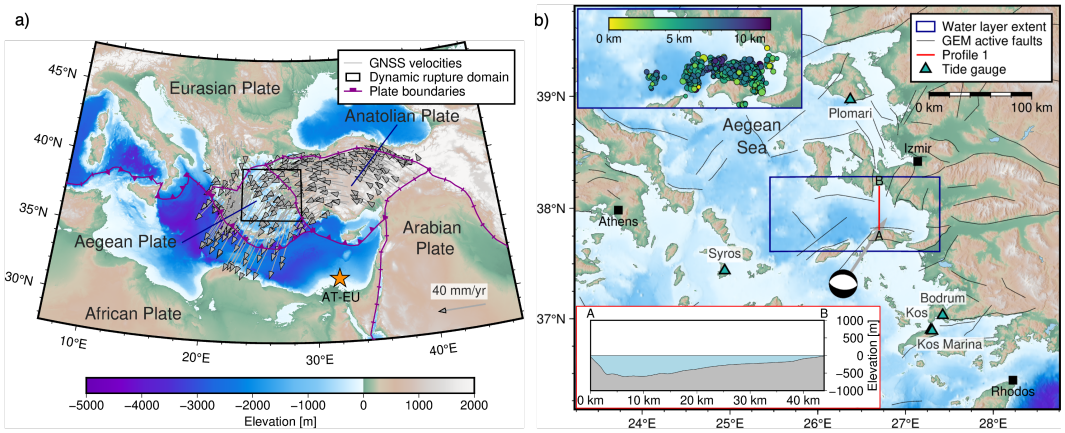


Figure 1. a) Present-day circular counterclockwise kinematic motion of 346 regional GNSS stations (England et al., 2016) relative to the Anatolia-Eurasia (AT-EU) Euler pole (orange star; Le Pichon & Kreemer, 2010). Plate boundaries are indicated by purple lines (Bird, 2003) and show that the Aegean Sea plate is bounded by several larger tectonic plates, namely the Eurasian plate to the north, the African plate to the south and west, and the Anatolian plate to the east. The black rectangle marks the area of the earthquake dynamic rupture domain as visualized in b). b) Aegean Sea region with active faults from the GEM Global Active Faults Database (GEM GAF-DB; Styron & Pagani, 2020) shown as black lines. The earthquake focal mechanism for the M_W 7.0 Samos earthquake is obtained from the GCMT catalog (Dziewonski et al., 1981; Ekström et al., 2012). Relocated aftershocks from 30 October until 1 December 2020 (Kiratzi et al., 2022) are color-coded with depth (top-left figure inset). The blue rectangle shows the extent of the ocean acoustic water layer as used for 3D fully coupled earthquake-tsunami modeling (see Fig. 2). Teal triangles indicate five of the seven sea level monitoring stations (Flanders Marine Institute (VLIZ), Intergovernmental Oceanographic Commission (IOC), 2026) and the bottom-left figure inset shows the bathymetric profile from GEBCO Bathymetric Compilation Group (2022) along the north-south-trending trace A–B (red line; Profile 1).

and solves the 2D depth-averaged non-linear shallow water equations based on the finite volume method and utilizes adaptive mesh refinement (LeVeque et al., 2011; Berger et al., 2011; Mandli et al., 2016). GeoClaw has been extensively validated (LeVeque & George, 2008; Gonzalez et al., 2011), including against observations near Hawaii from the 2011 Tōhoku earthquake and tsunami (Arcos & LeVeque, 2015).

2.2 Reference kinematic finite-fault slip model

Multiple finite-fault models exist for the 2020 M_W 7.0 Samos earthquake (e.g., Cetin et al., 2020; Taymaz et al., 2022; Sun et al., 2024). Finite-fault inversions are known to be prone to variability in terms of inferred slip distribution (e.g., Beresnev, 2003; Mai, Schorlemmer, et al., 2016; Wong et al., 2024). Thus, rather than comparing all existing fault slip models for the Samos earthquake, we select one reference model that is in agreement with the broader regional stress field (Konstantinou et al., 2017). We choose the kinematic model of Plicka et al. (2022), which uses displacement waveforms from local strong motion stations, filtered in the frequency range of 0.02 to 0.15 Hz, and static GNSS displacement data from Ganas et al. (2021). They use a linear multiple time-window earthquake slip inversion approach with k^{-2} smoothing (LinSlipInv; Gallovič et al., 2015). LinSlipInv has been applied to various events near Greece, such as the 2015 M_W 6.4 Lefkada earthquake (Sokos et al., 2016) and the 2018 M_W 6.8 Zakynthos earthquake (Sokos et al., 2020).

The fault geometry of Plicka et al. (2022) has rectangular (planar) dimensions (100×24 km), a strike angle of 265°, a 40° dip angle towards the north, and a rake angle of -110°. It is composed of 480 sub-faults, each spanning 2.5×2.0 km along-strike and along-dip, respectively. This fault geometry is consistent with the spatial distribution of relocated aftershocks (Cetin et al., 2020; Kiratzi et al., 2022; Fountoulakis et al., 2023) and with GNSS observations (Ganas et al., 2021). Moreover, Heidarzadeh et al. (2021) and Hu et al. (2022) have shown that tsunami simulations using a north-dipping fault plane reproduce tsunami observations better than the south-dipping fault geometries. In addition to the fault geometry of Plicka et al. (2022), we utilize its rake, sub-fault total slip, and time-window slip distributions (Section 2.3).

2.3 Kinematic source simulation

Prescribing the spatio-temporal evolution of slip on a predefined fault is known as kinematic rupture simulation (e.g., Haskell, 1964; E. Tinti et al., 2021). Here, we impose the slip rate as a boundary condition on the fault plane. To avoid numerical artifacts, we utilize a pseudo-friction law that suppresses smearing and aliasing effects, following the approach of E. Tinti, Spudich, and Cocco (2005) and Causse et al. (2014).

To integrate the finite-fault model of Plicka et al. (2022) and obtain our kinematic source simulation with SeisSol (hereinafter Kinematic Rupture Model A), we convert the finite-fault model (Section 2.2) from its .fsp format (Mai, Shearer, et al., 2016) into ASAGI files (Rettenberger et al., 2016). ASAGI, a parallel server for adaptive geoinformation, handles the parallel data access, allowing SeisSol to efficiently access the underlying data during the simulation. Here, we infer the rupture onset time and duration of the positive slip acceleration by identifying the first time window exceeding a threshold slip value of 1 mm and the window corresponding to peak slip, respectively. During this conversion process, the finite-fault slip distribution is spatially up-sampled by a factor of 10 using a cubic interpolation method. We choose this interpolation to ensure that the coarse input data from the finite-fault model is smooth enough to be resolved by the high-order ADER-DG discretization. Note that preserving the seismic moment and average slip is not strictly guaranteed by construction during this interpolation, but rather enforced using an iterative post-processing optimization loop inspired by E. Tinti, Spudich, and Cocco (2005) and verified post-upsampling (Table 2).

The temporal evolution of slip for individual sub-faults is parameterized by regularized Yoffe functions (E. Tinti, Fukuyama, et al., 2005). These functions are constructed by convolving the original Yoffe function (Nielsen & Madariaga, 2003) with a triangular function. Following E. Tinti, Fukuyama, et al. (2005), we assign a constant value of 1.27 to the ratio of the time to peak slip velocity to the half-duration of the triangular function to uniquely define the regularized Yoffe parameters across all sub-faults.

2.4 Dynamic rupture model setup

2.4.1 Initial stress

Dynamic rupture simulations allow the earthquake dynamics to evolve spontaneously based on the model's initial conditions in a self-consistent way. The initial stress setup can be obtained in several ways, for example by iteratively updating dynamic stress drop and strength excess (Pulido & Dalguer, 2009). We use the on-fault stress changes of the Kinematic Rupture Model A to inform two dynamic rupture simulations (hereinafter Dynamic Rupture Models B & C). Specifically, we use the shear stress change in the dip direction at the end of Kinematic Rupture Model A, which is larger by a factor of two than the normal stress change or stress change in the strike direction, a simplification consistent with the predominantly dip-slip mechanism. However, rather than using this stress change directly, the initial shear traction in the dip direction τ_d is computed by subtracting the imported kinematic shear stress change from a background traction proportional to the dynamic friction coefficient μ_d (Section 2.4.2) and the initial effective normal stress σ_n' (defined as negative in compression following SeisSol convention). Specifically, $\tau_d = \mu_d \sigma_n' - \Delta\tau_{d,\mathrm{A}}$, where $\Delta\tau_{d,\mathrm{A}}$ denotes the imported dip-direction shear stress change from Kinematic Rupture Model A. At the 6.35 km hypocentral depth (Section 2.4.3), $\sigma_n' \approx -32$ MPa and $\Delta\tau_{d,\mathrm{A}} \approx 8.3$ MPa, resulting in an initial shear traction of approximately -14.7 MPa following SeisSol convention. For simplicity, the initial shear traction in the strike direction is set to zero ($\tau_s = 0$ MPa). This omits the right-lateral strike-slip component present in the reference kinematic model of (Plicka et al., 2022) (rake of -110°). However, prescribing a pure normal-faulting initial rake setup of -90° for the dynamic rupture models, following the definition of Aki and Richards (2002), remains consistent with the rake angle uncertainty across various agency moment tensor solutions, also summarized by e.g., Plicka et al. (2022), including the USGS W-phase (U.S. Geological Survey, 2020) and Global Centroid Moment Tensor (GCMT) solutions (Dziewonski et al., 1981; Ekström et al., 2012).

The difference between the two Dynamic Rupture Models B and C is the governing initial effective normal stress. For Dynamic Rupture Model B, we prescribe a uniform initial effective normal stress of $\sigma_n' = -32$ MPa (recall following SeisSol convention, normal stress is negative in compression), which is smaller than the often used 50 MPa (Ramos et al., 2022; Taymaz et al., 2022). However, our models require a smaller effective normal stress due to the shallower nucleation depth. In addition, 32 MPa lowers the overall static fault shear strength to account for elevated pore-fluid pressure at shallow depths. To have a more realistic representation of σ_n', a depth-dependent effective normal stress as a function of gravity g, depth z, and density ρ is used for Dynamic Rupture Model C inspired by (E. Tinti et al., 2021). We prescribe $\sigma_n' = \min\left(-10\ \mathrm{MPa}, (\rho(z) - 2785\ \mathrm{kg\ m^{-3}}) \cdot g \cdot z\right)$, where z is negative downward and $\rho(z)$ is the local solid Earth density as used by (Plicka et al., 2022). Because $\rho(z)$ is defined via a 1D layered subsurface model (Section 2.6), $\sigma_n'(z)$ exhibits step-wise increases across layers, increasing compressive normal stress with depth. At the 6.35-km nucleation depth, $\rho = 3300\ \mathrm{kg/m^3}$. Thus, the resulting effective normal stress for Dynamic Rupture Model C is $\sigma_n' \approx -32$ MPa at the nucleation depth, similar to Dynamic Rupture Model B. This formulation implies an over-hydrostatic pore-fluid pressure gradient of $\approx$ 27.3 MPa km^{-1} that reduces the lithostatic overburden (Rice, 1992; Madden et al., 2021) and enforces at least 10 MPa compressive effective normal stress near the free

surface. Consequently, the magnitude of the compressive effective normal stress is smaller near the surface and increases with depth.

2.4.2 Friction and fault strength

We use a linear slip weakening (LSW) friction law (e.g., Ida, 1972) with on-fault cohesion to obtain the fault strength τ_c and model frictional yielding and dynamic slip evolution.

$$\tau_c = C_0 + \mu \cdot |\sigma_n'| \,. \tag{1}$$

Here, C_0 is the on-fault cohesion of 0.4 MPa, taken from Taymaz et al. (2022), representing the positive magnitude of the cohesion parameter, which is prescribed as negative following SeisSol convention. Cohesion is also added during forced rupture. The friction coefficient, given by $\mu = \min(\mu_{\text{nuc}}, \mu_{\text{lsw}})$, depends on the nucleation friction coefficient μ_{nuc} (Section 2.4.3) and the slip-weakening friction coefficient μ_{lsw}, given by the linear slip-weakening friction law,

$$\mu_{lsw}(\delta) = \mu_s - \frac{\mu_s - \mu_d}{D_c} \min(\delta, D_c) \,, \tag{2}$$

which is a function of the accumulated fault slip $\delta(t)$ at each point on the fault. Here, μ_{lsw} decreases linearly from the static friction coefficient (μ_s) to the dynamic friction coefficient (μ_d) over a characteristic slip-weakening distance (D_c). Once the accumulated slip exceeds D_c, friction remains at the dynamic level (e.g., Andrews, 1976; Ma et al., 2008; Ramos et al., 2022). Similar to Taymaz et al. (2022), we choose $\mu_s = 0.5$, but prescribe $\mu_d = 0.2$, which is slightly smaller (Table 1), since a lower dynamic friction coefficient facilitates sustained dynamic rupture and slip accumulation on normal faults (e.g., Mosconi et al., 2025; Margolis et al., 2026). Through trial-and-error simulations targeting the observed seismic moment through the accumulation of fault slip, we find that a lower D_c of 0.1 m is required, because reducing D_c lowers the fracture energy, facilitating rupture propagation at a given stress level. At the hypocenter (Section 2.4.3), the initial shear traction magnitude of approximately 14.7 MPa (Section 2.4.1) lies between the static and dynamic frictional strength contributions (excluding cohesion), which are $\mu_s|\sigma_n'| \approx 16.0$ MPa and $\mu_d|\sigma_n'| \approx 6.4$ MPa, respectively.

2.4.3 Hypocenter and nucleation

Plicka et al. (2022) used a fixed depth of 6 km to obtain a well-posed finite-fault inversion and derived a stable relocated epicenter location of 37.900°N and 26.817°E with a spread of ±1 km by testing a variety of different velocity models. Since Kinematic Rupture Model A and subsequently the Dynamic Rupture Models B and C use the inferred fault geometry of Plicka et al. (2022), the deduced location of the epicenter is transformed from the World Geodetic Reference System (WGS84) to the local reference system and then projected vertically with depth until the intersection with the fault plane is found, which appears at 6.35 km. This depth and the previously transformed coordinates represent the hypocenter location chosen for the rupture initiation of the Dynamic Rupture Models B & C. This nucleation depth further aligns with the regional seismicity and aftershocks observed following the mainshock (30 October – 1 December 2020; Supporting Information, Fig. S1), with 989 events relocated during this period, predominantly at depths shallower than 10 km (Kiratzi et al., 2022).

We initiate rupture smoothly in time and space by time-dependently reducing μ_{nuc} within a circular nucleation patch (e.g., R. A. Harris et al., 2018). The process closely follows Li et al. (2023), who chose an increasing circular region centered at the predetermined hypocenter to start the spontaneous dynamic rupture. The fault strength can

also be reduced in an ellipsoid placed at the focus to achieve a smaller forced nucleation area (E. Tinti et al., 2021). However, this was not necessary in this study because the radius of the nucleation zone (r_{crit}) is sufficiently small (1.5 km) to allow rupture to become entirely self-sustaining outside the forced region (Galis et al., 2015) and is in the range of plausible nucleation radii for a moment magnitude 7.0 earthquake (Beroza & Ellsworth, 1996).

$$T(r) = \begin{cases} \frac{r}{0.7v_S} + \frac{0.081r_{crit}}{0.7v_S}\left(\frac{1}{1-(r/r_{crit})^2} - 1\right), & r \leq r_{crit} \\ 10^9, & r > r_{crit} \end{cases} \tag{3}$$

Eq. 3 gives the rupture initiation time $T(r)$, where r represents the radial distance to the hypocenter. The forced rupture expands at a speed of $0.7 \cdot v_S = 2.66$ km s^{-1}, where $v_S = 3.8$ km s^{-1} is used, larger than the actual local shear-wave velocity of 3.5 km s^{-1} at the nucleation depth (Novotný et al., 2001). Within the nucleation patch ($r \leq r_{crit}$), once forced weakening begins, μ_{nuc} drops linearly in time from μ_s to μ_d. The imposed reduction in μ_{nuc} therefore lowers the local fault strength below the magnitude of the initial shear traction, allowing rupture to initiate. Outside the zone of forced rupture, T is equal to 10^9 s, which implies that forced rupture does not occur outside the 1.5 km radius. Thus, rupture propagation beyond r_{crit} is entirely self-sustaining and governed purely by spontaneous slip-weakening friction $\mu_{lsw}(\delta)$. This gradual transition ensures that the spontaneous rupture overtakes the forced rupture smoothly, minimizing artifacts such as spurious oscillations.

Table 1. Overview of earthquake dynamic rupture modeling parameters. *The depth-dependent initial effective normal stress $|\sigma_n'|$ for Dynamic Rupture Model C is chosen in such a way that at the hypocenter depth of 6.35 km, the same value as in Dynamic Rupture Model B ($|\sigma_n'|$ =32 MPa) prevails.

	Dynamic Rupture Model B	Dynamic Rupture Model C	Taymaz et al. (2022)
Static friction coefficient (μ_s)	0.5	0.5	0.5
Dynamic friction coefficient (μ_d)	0.2	0.2	0.3
Critical slip-weakening distance (D_c) [m]	0.1	0.1	0.3
Nucleation radius (r_{crit}) [km]	1.5	1.5	1.5
Cohesion ($\|C_0\|$) [MPa]	0.4	0.4	0.4
Initial effective normal stress ($\|\sigma_n'\|$) [MPa]	32.0	depth-dependent*	50.0

2.5 Tsunami modeling techniques used in this study

Conventional earthquake-tsunami modeling is commonly based on so-called two-step approaches (e.g., Abrahams et al., 2023). Here, earthquake modeling is conducted first, followed by modeling the ensuing tsunami. Simplified, but faster workflows employ the "Okada" method (Okada, 1985, 1992) with an instantaneous sourcing of the tsunami

by the final static displacement of an earthquake model (e.g., Ohta et al., 2012; Sepúlveda & Liu, 2016; Kutschera, Jia, et al., 2024). To enable a better comparison, we infer the vertical displacement from our reference finite-fault slip model by evaluating the generalized internal deformation formulation of Okada (1992) at the surface ($z = 0$), thus, equivalent to Okada (1985), where we assume a Poisson's ratio of 0.25.

A more advanced technique takes the time-dependent earthquake ground displacement to initialize sea surface perturbations using a (non-linear) shallow water solver referred to as one-way linking (Ulrich, Vater, et al., 2019; Madden et al., 2021; Kutschera, Gabriel, et al., 2024). We apply this technique to our kinematic and dynamic rupture models (Section 2.5.2), but this remains a two-step process. Alternatively, the time-dependent seafloor velocity (Saito & Furumura, 2009; Saito & Tsushima, 2016; Saito, 2019) or the sea surface velocity (i.e., superposition method from Saito (2019); Saito et al. (2019), yielding the complete wavefield) can be taken as forcing to trigger the tsunami in a simulation. The reader is referred to Abrahams et al. (2023) for more information. However, not always are two steps required: the state-of-the-art fully coupled method (Section 2.5.1) can simultaneously solve for earthquake rupture and tsunami generation in a single 3D numerical simulation.

2.5.1 Fully coupled 3D earthquake-tsunami modeling

The fully coupled method combines earthquake rupture and tsunami generation in a single simulation, capturing 3D elastic, acoustic, and gravity wave propagation, including dispersion effects, simultaneously (e.g., Maeda & Furumura, 2013; Lotto & Dunham, 2015; Wilson & Ma, 2021). At the elastic-acoustic interface (that is, the seafloor), continuity of the normal velocity and traction exists (Sochacki et al., 1991; Wilcox et al., 2010). At the same time, a linearized free surface boundary condition accounting for gravity restoring forces (Krenz et al., 2021) is utilized at the sea surface to capture the tsunami excitation in SeisSol. The method has been developed for coupled earthquake-tsunami modeling of the 2018 Sulawesi earthquake and tsunami (Krenz et al., 2021) and applied to earthquake-tsunami scenarios in North Iceland (Kutschera, Gabriel, et al., 2024), suited to investigate the initial tsunami generation and the full ocean-acoustic wavefield with all its complexity. By explicitly resolving 3D wave propagation through the water column, the fully coupled formulation reproduces the wavenumber-dependent reduction of the sea surface response to short-wavelength seafloor deformation, which scales as $1/\cosh(kH)$ for wavenumber k and water depth H. In conventional tsunami sourcing frameworks, this effect may be approximated by applying a "Kajiura" filter (Kajiura, 1963), which we do not apply here (Section 2.5.3). For the local water depths considered here ($H \approx$ 400 m on average), the reduction is negligible at the dominant 10–20 km deformation wavelengths ($\lesssim$3%), but reaches ∼11% at 5 km and ∼47% at 2 km wavelength.

Water does not support shearing motion. Thus, the shear modulus is $\mu = 0$, allowing for only (compressional) acoustic wave propagation, such that the shear wave velocity is $v_S = 0$. Additionally, a (to first-order steady-state) density of 1025 kg m^{-3}, representative of salt water, is assumed in the water layer. However, a strictly constant density would imply an incompressible fluid and not allow for compressional waves. Therefore, the steady-state density is complemented with density perturbations only depending on the pressure based on a linearized equation of state (Krenz et al., 2021).

Each fully coupled earthquake-tsunami scenario is run for 6 min of simulated time. SeisSol can model the initial tsunami generation with high accuracy in time and space; however, fully coupled earthquake-tsunami simulations are currently not suited for modeling inundation and tsunami run-up, and can not capture long-term tsunami propagation. The latter is caused by the selection of a smaller water layer (Section 2.6) since an acoustic medium covering the whole offshore domain would (1) result in high computational costs required for the small element size within the acoustic medium and (2) lead

to ongoing meshing challenges posed by the mesh generation process itself, with the crucial but non-trivial intersection of bathymetry and topography with the sea surface (Wirp et al., 2026). Therefore, the surface output (i.e., ground displacement) of SeisSol is additionally used to inform GeoClaw (Section 2.5.2).

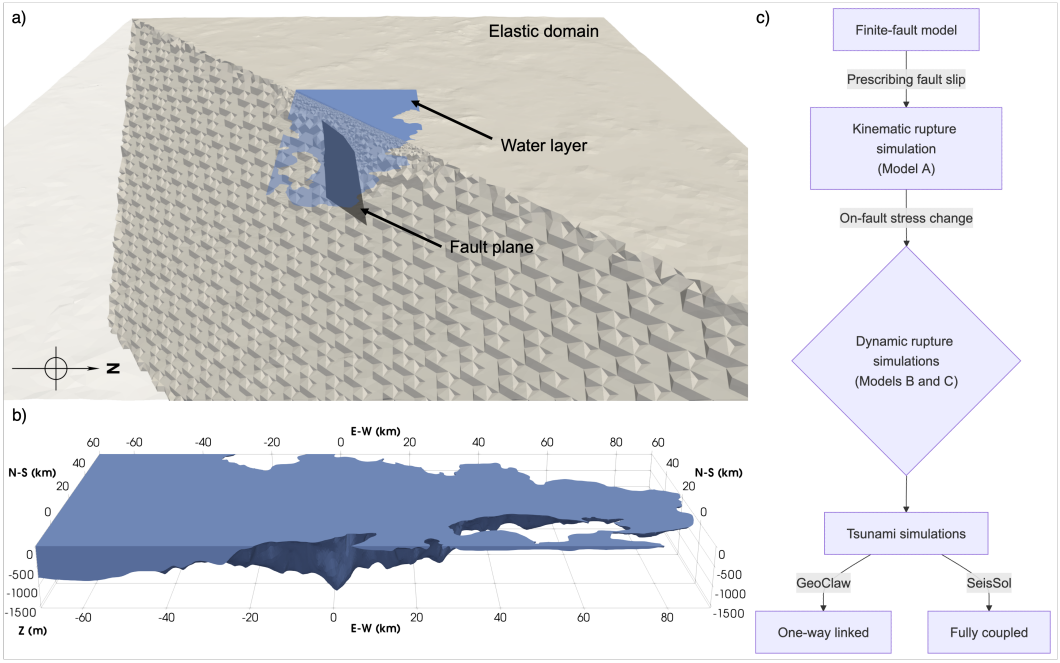


Figure 2. a) Transect of the three-dimensional unstructured tetrahedral mesh for the elastic domain (gray), including the water layer (blue) and the north-dipping fault plane (black) of Plicka et al. (2022). The fault plane has a strike/dip of 265°/40° and intersects the seafloor. The static mesh refinement is visible near the fault plane and the transected domain. b) Vertically exaggerated dimension of the 3D water layer, where we prescribe a rigidity of $\mu = 0$. c) Workflow of this study: we start with the finite-fault model of Plicka et al. (2022) and prescribe its spatio-temporal slip distribution in the Kinematic Rupture Model A. We compute and use the on-fault shear stress change in dip direction of this model to inform the two spontaneous Dynamic Rupture Models B & C, which in turn inform tsunami simulations using two different methods: (i) 2D depth-averaged non-linear shallow water equations (GeoClaw; Berger et al. (2011)) following a two-step approach and (ii) 3D fully coupled earthquake-tsunami modeling where earthquake rupture and tsunami generation are simultaneously solved for in a single simulation using SeisSol (Gabriel et al., 2025).

2.5.2 One-way linked 2D tsunami modeling

Before informing the one-way linked tsunami simulations with the time-dependent seafloor displacement of the SeisSol earthquake rupture models, the displacement field is first converted from a Cartesian-based coordinate system into a geographic coordinate system, and from the unstructured SeisSol output (Section 2.6) to a structured format, where we account for the contribution of the horizontal displacement to the vertical displacement (Tanioka & Satake, 1996). To allow a fair comparison with the fully coupled model, this vertical displacement is required with high temporal resolution, where we take the first 50 s at 0.1 s increments, well beyond when each earthquake rupture has concluded. For the remainder of the one-way linked GeoClaw tsunami simulations ($t > 50$ s),

the displacement is held at its respective 50 s value, with all seismic waves having left the source region. Next, a 2D Hann filter with a width of $\approx 0.30^\circ$ in both longitude and latitude is applied along the outer boundaries of the displacement region to avoid spurious signals from the permanent seafloor deformation (Ulrich et al., 2022).

Our one-way linked tsunami modeling spans the Aegean Sea and covers $5^\circ \times 5^\circ$, with longitude ranging from 23°E to 28°E and latitude from 35°N to 40°N. We model the tsunami propagation over a simulation time of 4 hr. We use three adaptive mesh refinement (AMR) levels. The coarsest grid has a resolution of 3000 m ($\sim$1.5 arcmin). The spatial refinement ratios are 2 and 30 in both spatial directions. These ratios yield a resolution of 1500 m ($\sim$48 arcsec) for the intermediate AMR level of two, and a high spatial refinement resolution of 50 m ($\sim$1.62 arcsec) at AMR level three. This level three refinement is enforced within the bay of Samos, which encloses the water layer from the fully coupled models, for the first 6 min. Although the used GEBCO bathymetry resolution is coarser at 15 arcsec ($\approx$370 to 460 m; GEBCO Bathymetric Compilation Group, 2022) and this high level of refinement does not add any new bathymetry information, we chose this refinement to be roughly consistent with the higher-order SeisSol scheme and discretization (Section 2.6). Starting at 35 min through the end of the simulations, level three refinement is also enforced for $0.1^\circ \times 0.1^\circ$ squares surrounding each of the seven tide gauges. To solve the non-linear shallow water equations on a latitude–longitude spherical grid, we use GeoClaw with an unsplit, second-order Lax–Wendroff wave propagation method (LeVeque et al., 2011), with transverse wave corrections and a Monotonized Centered (MC) limiter. Additionally, we use GeoClaw with a variant of the f-wave formulation (Bale et al., 2003; George, 2008), maintaining well-balancing. We assume bottom friction has negligible effect in deeper water and restrict the Manning coefficient (0.025) to water depths shallower than 200 m, where it is coupled via first-order Godunov source splitting. Non-reflecting outflow boundary conditions are applied along all domain edges. The water density is prescribed as 1025 kg m^{-3}, and the Coriolis forcing is disabled. Synthetic sea surface elevation time series on the finest temporal refinement level in GeoClaw are recorded with an average temporal sampling interval of ~ 0.22 s. Each one-way linked tsunami simulation was run on 16 threads and required $\sim$43 CPUh, not taking into account writing output at 1 s increments for the first 6 min of simulated time. The observed tide gauge records at seven stations in the Aegean Sea are filtered similarly to Kutschera, Jia, et al. (2024), where we first remove the first-order background sea level trends using a Locally Weighted Scatterplot Smoothing (LOWESS; Cleveland, 1979) algorithm with a smoothing fraction of 0.1, before we apply a 300 s zero-phase low-pass filter.

2.5.3 Sea surface height anomaly post-processing

We define the sea surface height anomaly (ssha) as the deviation of the sea surface from being at rest for both one-way linked and fully coupled modeling. We apply a 4th-order isotropic 2D spatial Butterworth low-pass filter with a cut-off wavelength of $\lambda_c = 2$ km to the modeled ssha. Wirp et al. (2021) showed that such a Fourier filter applied to the time-dependent seafloor movement efficiently suppresses seismic wave signals. We apply this filter to all modeled sea surface height anomalies across the different tsunami modeling frameworks. We do not apply a classical Kajiura filter (Kajiura, 1963). Similar to the Kajiura filter, which mimics the wavenumber-dependent reduction of the sea surface response across the water column, our spatial low-pass filter dampens short-wavelength (high-wavenumber) signals. In contrast to the Kajiura filter, which scales this reduction with wavenumber for a representative, constant water depth, our Butterworth filter applies a uniform spatial threshold across the entire domain and is applied to the ssha instead of the seafloor motion. To compare modeled tsunami excitation across frameworks, we restrict our analysis to offshore regions deeper than 100 m. This bathymetric masking is necessary because the linearized gravity-restoring boundary condition used in the fully coupled approach breaks down near-shore (Section 2.5.1), which can be assessed using the non-dimensional Ursell number $U = \frac{\eta\lambda^2}{H^3}$ (Ursell, 1953), where η is the wave

amplitude (or ssha), λ the wavelength, and H the water depth. Assuming wavelengths $\lambda \approx 2$–5 km for trailing waves, together with wave amplitudes $\eta \approx 0.25$–0.5 m, we obtain high Ursell numbers ($U \sim 10^2$–10^4) in very shallow coastal waters ($H \leq 20$ m). This indicates a strongly non-linear shallow-water regime. In contrast, at water depths $H \geq 100$ m, Ursell numbers for trailing waves drop to $\mathcal{O}(1$–$10)$, indicating that non-linear and dispersive effects are of comparable strength. Both frameworks remain applicable in this regime, whereas the non-dispersive shallow water equations approach the limit of their validity for these trailing waves, consistent with the framework differences we identify in Section 4.

2.6 Computational mesh

By utilizing unstructured tetrahedral elements, SeisSol resolves complex bathymetry and the fault geometry needed for realistic earthquake-tsunami modeling in the Aegean Sea. Here, we use the gridded bathymetry data of GEBCO Bathymetric Compilation Group (2022). For consistency, the same bathymetry is used for all one-way linked tsunami simulations (Section 2.5.2). The fault plane of Plicka et al. (2022) (Section 2.2) is intersected with this bathymetry, and the part above the seafloor is removed. Plicka et al. (2022) adapted the 1D velocity-density model of Novotný et al. (2001), obtained from inversion of observed group-velocity dispersion curves for Love and Rayleigh wave propagation from northwestern Turkey to western Greece, traversing the Aegean Sea. Thus, we use the same adapted subsurface model for all subsequent earthquake rupture modeling, where the material parameters are projected to the next upper node in the computational mesh.

Krenz et al. (2021) implemented the possibility to include a 3D water layer in a SeisSol earthquake rupture simulation. This requires the discretization of the water volume (acoustic medium) above the solid Earth (elastic medium). The size of the elastic domain is 474 km × 399 km × 202 km, whereas the water layer has a maximum depth of 1.58 km and a maximal length and width of 160 km and 76 km (Fig. 2). Absorbing lateral boundary conditions are prescribed along open-water edges to allow fast-propagating seismo-acoustic waves to exit the domain. Along coastlines, the water layer terminates against the solid Earth topography. A target discretization of $h = 200$ m is used for the fault plane and the water layer, together with a fourth-order ($\mathcal{O}4$) accurate scheme in time and space (polynomial degree $p = 3$) for all SeisSol simulations. For the cohesive zone, this means an effective on-fault resolution of $h/(p+2) = 40$ m, which adequately resolves the median cohesive zone width of ~ 200 m and ensures that even the 5th percentile width of ~ 75 m is sampled by nearly two sub-elemental integration points (e.g., Day et al., 2005; de la Puente et al., 2009; Madden et al., 2021). For the complex 3D volumetric water layer, this discretization translates into elements of variable size, with a minimum edge length of ∼64 m and a maximum of ∼400 m. Over 97.7% of all elements fall within the 100–300 m range, confirming that the nominal 200 m resolution governs the discretization across the domain, which we adopt for any discussion on maximum resolved frequencies. Assuming a ≤10 % envelope misfit following (Käser et al., 2008) and average velocities of 3044 m s^{-1} for Rayleigh, 1500 m s^{-1} for acoustic, and 68 m s^{-1} for tsunami waves, we resolve at least 5.5 Hz of the Rayleigh, 2.7 Hz of the acoustic, and 0.1 Hz of the tsunami wavefield. Here, we followed Käser et al. (2008) and adopted the $N_\lambda = 2.76$ elements per wavelength required for the used ADER-DG $\mathcal{O}4$ scheme, which means the minimum resolved wavelength ($\lambda_{\min}$) is $\lambda_{\min} = N_\lambda \cdot h \approx 550$ m for all wave types in the water layer. The total number of elements for the mesh is ∼20 million elements, out of which 7 million elements represent the water layer exclusively. Here, water depths shallower than 200 m are discretized by ∼3 million elements (about 43% of the total water layer). A single fully coupled simulation (6 min of simulated time) required up to ∼32,000 CPUh, using 64 nodes (that is 3072 cores) on the supercomputer SuperMUC-NG in Munich. Each dynamic rupture simulation is also run without the water layer to inform the respective one-way linked simulation (Section 2.5.2). Upon re-

moving the water layer, a 13-million-element mesh remains, representing the elastic domain only.

3 Results

3.1 Earthquake rupture

3.1.1 Prescribed and spontaneous slip evolution

The three earthquake kinematic and dynamic rupture models A–C all have a comparable slip distribution and produce similar moment magnitudes of 7.03, 6.99, and 6.97, respectively (Table 2). The Kinematic Rupture Model A has a peak slip of 2.44 m (Fig. 3), consistent with the finite-fault model of Plicka et al. (2022). The dynamic rupture models evolve spontaneously, without prescribing the slip or slip rate in time and space (Fig. 4, Movie S1). Despite their spontaneous evolution, Dynamic Rupture Models B and C produce similar peak slips of 2.60 m and 2.46 m, respectively. The average slip for the ruptured area, where we consider the part of the fault that experienced at least 0.2 m of slip, is 0.86 m, 1.00 m, and 1.02 m for Models A–C, respectively. All rupture models yield surface-breaking slip. However, the amount of near-surface slip differs slightly. The Kinematic Rupture Model A has localized surface-breaking slip near the northernmost coast of Samos, whereas both dynamic rupture models produce extended surface-breaking slip, preserving the overall pattern of the slip distribution around the hypocenter. Dynamic Rupture Models B & C both arrest laterally due to the imposed stress changes, whereas Dynamic Rupture Model C also arrests with depth before reaching the deeper end of the fault plane due to the increasing normal stress with depth. The source time functions (STFs) of the Dynamic Rupture Models B & C are, however, ∼2–3 s shorter than the STF of the finite-fault slip model of Plicka et al. (2022), whereas the STF of the Kinematic Rupture Model A is ∼3 s longer (Fig. 4). This is linked to the rupture duration of the respective models, ranging between ∼17 s and 23 s (Table 2).

3.1.2 Generated seafloor displacement

The permanent subsidence patterns of all four models (Okada, Kinematic Rupture Model A, and Dynamic Rupture Models B & C) are entirely offshore and show good agreement to first order (Fig. 3b), which allows the comparison of increased tsunami modeling complexity (Section 3.2). Second-order, local differences originate from variations in rupture propagation. For example, due to the extended near-surface slip of both dynamic rupture models, their surface-breaking seafloor displacements extend beyond the western edge of Samos Island. Peak seafloor subsidence values are -0.78 m for the Okada solution without any topography based on the finite-fault model (Plicka et al., 2022), and -0.86 m, -0.87 m, and -0.84 m for rupture models A–C (including topography, but prior to the "Tanioka"-correction; Tanioka & Satake, 1996), respectively (Table 2). Here, the Tanioka-correction for rupture models A–C only contributes about 1% to the peak subsidence, but increases the very small peak uplift (≈10 cm) by 20–67% (Table 2), because horizontal displacement projects onto the steeper bathymetric slopes north of Samos. We therefore apply it to all one-way linked sources.

3.1.3 Ground motion comparison

The three earthquake rupture models A–C include the propagation of seismic waves, generating ground motion. Here, we focus on the vertical peak ground velocity (PGV_V) and horizontal peak ground velocity (PGV_H), defined as $PGV_V = \max|v_z(t)|$ and $PGV_H = \max(\max|v_x(t)|, \max|v_y(t)|)$, where $v_x(t)$, $v_y(t)$, and $v_z(t)$ represent the east-west, north-south, and vertical velocity components, respectively. In addition, we compute the orientation-independent horizontal ground motions without geometric means (RotD50) after Boore (2010), not to be confused with the GMRotD50 measure that takes into account the ge-

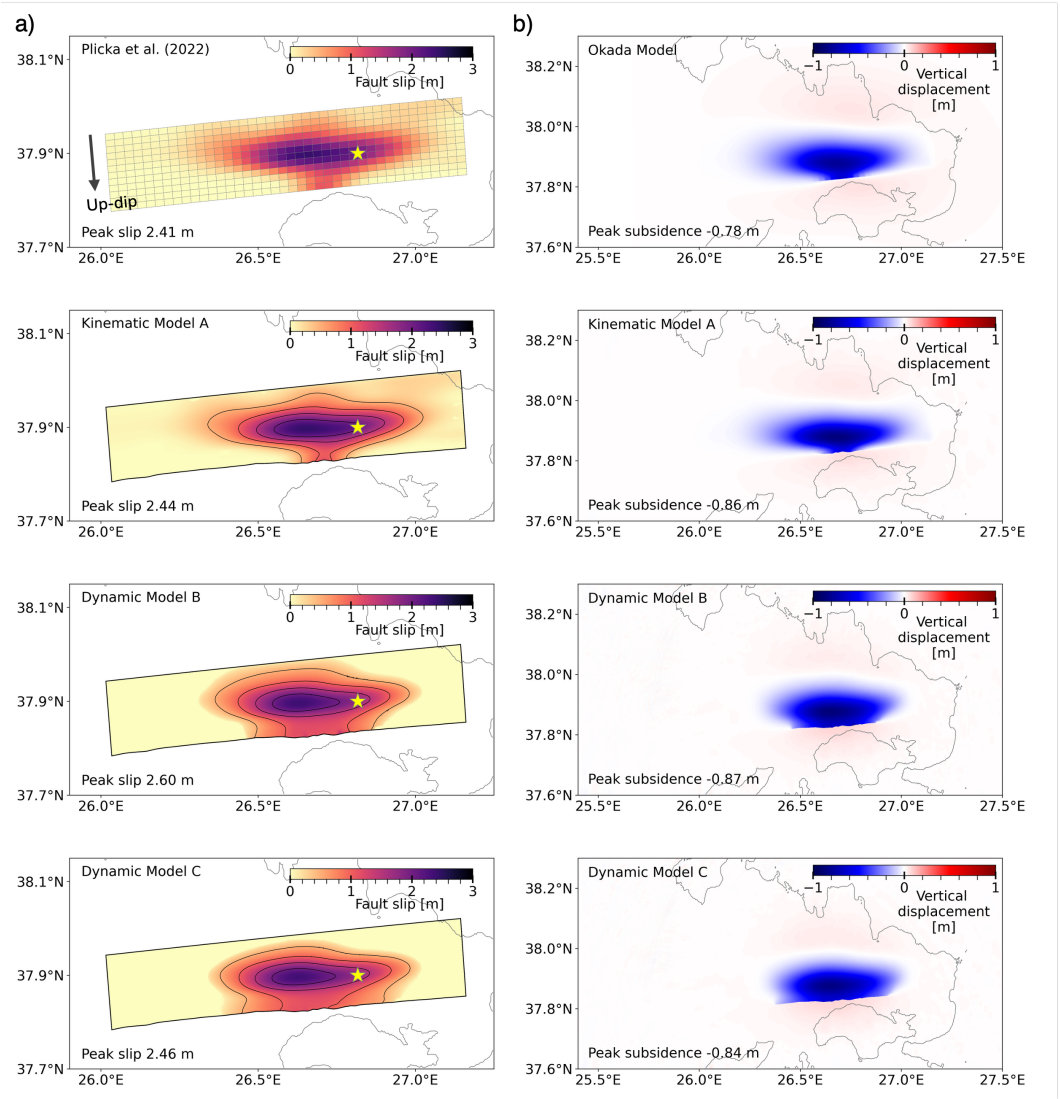


Figure 3. a) Fault slip distributions of the considered models, showing similar large-scale slip features east and west of the preferred epicenter of Plicka et al. (2022), marked by the yellow star. The finite-fault slip model of Plicka et al. (2022) informs Kinematic Rupture Model A, whose on-fault shear stress change in dip direction serves as an initial condition for the two spontaneous Dynamic Rupture Models B and C. The black contour lines at 0.5 m increments represent the fault slip. b) Vertical ground displacements of each model, characterized by comparable overall subsidence but smaller near-surface variations, with a wider pattern of displacement for the Dynamic Rupture Models B & C. Shown are static displacements computed with the Okada method (Okada, 1985) from the finite-fault model of Plicka et al. (2022), and the final time-dependent displacements of the three earthquake rupture models A–C.

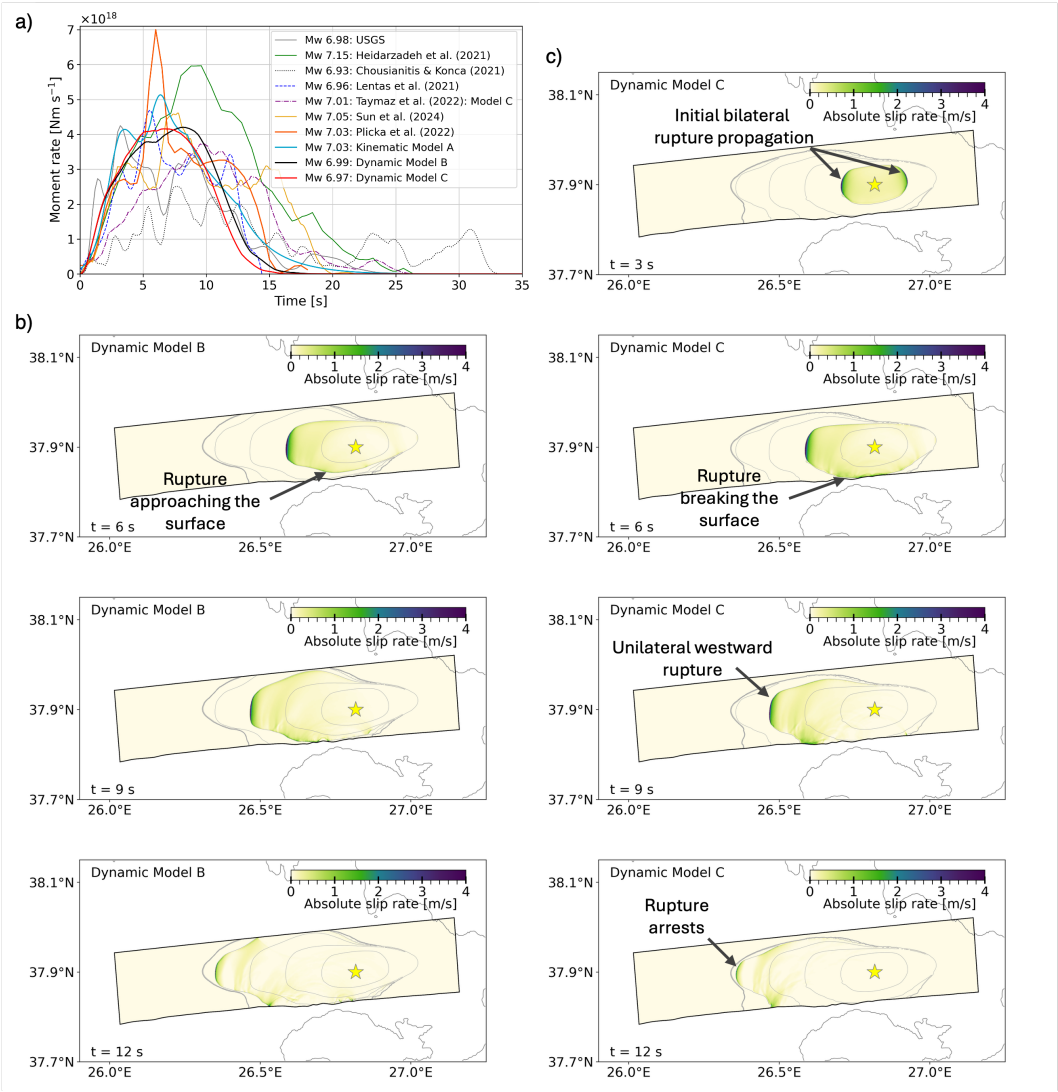


Figure 4. a) Comparison of moment rate functions from previous studies (U.S. Geological Survey, 2020; Heidarzadeh et al., 2021; Chousianitis & Konca, 2021; Lentas et al., 2021; Taymaz et al., 2022; Sun et al., 2024; Plicka et al., 2022) with those from Kinematic Rupture Model A and Dynamic Rupture Models B & C. Note that the moment rates of Plicka et al. (2022) and of the Kinematic Rupture Model A have been shifted 2 s earlier for shape comparison only (and are not taken into account in the duration analysis). b, c) Overview of the simulated rupture propagation for the Dynamic Rupture Models B & C, respectively. The snapshots of the absolute slip rate show how the rupture evolves spontaneously, with an initial bilateral rupture propagation, followed by an up-dip propagation with surface-breaking slip, before the rupture continues to break unilaterally to the west until it arrests. The gray contours are the 3 s isochrones of the rupture time.

Table 2. Overview of fault kinematics and ground deformation results for the Kinematic Rupture (KR) Model A and the Dynamic Rupture (DR) Models B & C. *Considering those parts of the fault where the slip exceeds 0.2 m. †As obtained by applying the method of Okada (1985) without topography to the finite-fault slip model of Plicka et al. (2022).

	Plicka et al. (2022)	KR Model A	DR Model B	DR Model C
Moment magnitude M_W	7.03	7.03	6.99	6.97
Peak slip [m]	2.41	2.44	2.60	2.46
Average slip [m] *	0.86	0.86	1.00	1.02
Rupture area [km^2]*	1315	1287	1045	987
Rupture duration [s]	∼20	∼23	∼18	∼17
Peak uplift [m]	0.06†	0.06	0.10	0.09
Peak subsidence [m]	-0.78†	-0.86	-0.87	-0.84
Peak up. after Tanioka [m]	–	0.10	0.12	0.12
Peak sub. after Tanioka [m]	–	-0.86	-0.88	-0.84

ometric means (Boore et al., 2006). We restrict our comparison of simulated ground motions to observed records at seven near-source and coastal strong ground motion stations, as reported by (Askan et al., 2021). These stations include five stations (0905, 0911, 3528, 3533, 3536) operated by the Disaster and Emergency Management Presidency of Turkey (AFAD), one station (SMG1) operated by the Institute of Engineering Seismology and Earthquake Engineering of Greece (ITSAK), and one station (SAMA) operated by the Institute of Geodynamics of the National Observatory of Athens, Greece (NOA-IG/GEIN). Askan et al. (2021) reported that AFAD has processed the Turkish stations using a second-order Butterworth bandpass filter (0.1–25 Hz), which we adopt for the calculation of our ground motion maps (Fig. 5). However, the observations at stations SMG1 and SAMA were processed with different low-cut frequencies of 0.05 Hz and 0.22 Hz, respectively (Askan et al., 2021). Thus, we filter the simulated waveforms at these two stations using their respective low-cut frequencies before comparing them with the observed ground motions.

As the Kinematic Rupture Model A is informed by the finite-fault model constructed for the frequency range of 0.02 Hz to 0.15 Hz, its generated ground motions are overall smaller compared to those of the dynamic rupture models (Fig. 5). The shaking from the two dynamic rupture models is of similar magnitude, aside from local differences due to rupture directivity, e.g., at station 0905, where Dynamic Rupture Model C (5.20 cm s^{-1}) fits the observed vertical velocity (4.56 cm s^{-1}; Askan et al., 2021) better than Dynamic Rupture Model B (11.68 cm s^{-1}). To evaluate the overall fit of each model across the $N = 7$ stations, we calculate the root mean squared error $\left(RMSE(y,\hat{y}) = \sqrt{\frac{1}{N}\sum_{i=1}^{N}(y_i - \hat{y}_i)^2}\right)$, where y and $\hat{y}$ denote the observed and simulated peak velocities at station i, respectively. The RMSE between the observed PGV$_V$ of Askan et al. (2021) and the simulated vertical peak ground velocities of each rupture at the seven stations shown in Fig. 5 is 3.03 cm s^{-1}, 3.20 cm s^{-1}, and 1.75 cm s^{-1} for models A–C, respectively. The lower PGV$_V$ RMSE for Model C is predominantly driven by station 0905, which alone contributes ∼70% of Model B's squared PGV$_V$ RMSE. Excluding station 0905 causes Models B and C to be nearly indistinguishable in terms of vertical ground motion fit. Note that Model A's ground motions are band-limited by the 0.02–0.15 Hz inversion range of the reference model. Thus, its ground motion RMSE values are not directly comparable to the broadband dynamic models and are reported here mainly for completeness. The RMSE values for the RotD50 velocities are slightly larger due to the generally stronger horizontal shaking, especially those observed at stations SMG1 and SAMA, with RMSE values

of 7.34 cm s^{-1}, 7.02 cm s^{-1}, and 7.06 cm s^{-1}, for models A–C, respectively. Thus, horizontal ground motion misfits are essentially tied between Models B and C. Consistent for all rupture models is that the modeled RotD50 velocities at the sites are on average 15%, 18%, and 16% smaller than the modeled PGV_H of models A–C, respectively (Supporting Information, Fig. S2). Ultimately, we select Model C as the preferred dynamic rupture model, primarily due to its physical realism (incorporating depth-dependent initial effective normal stress; Section 2.4), but supported by the lower PGV_V RMSE driven by the ground motion directivity towards station 0905.

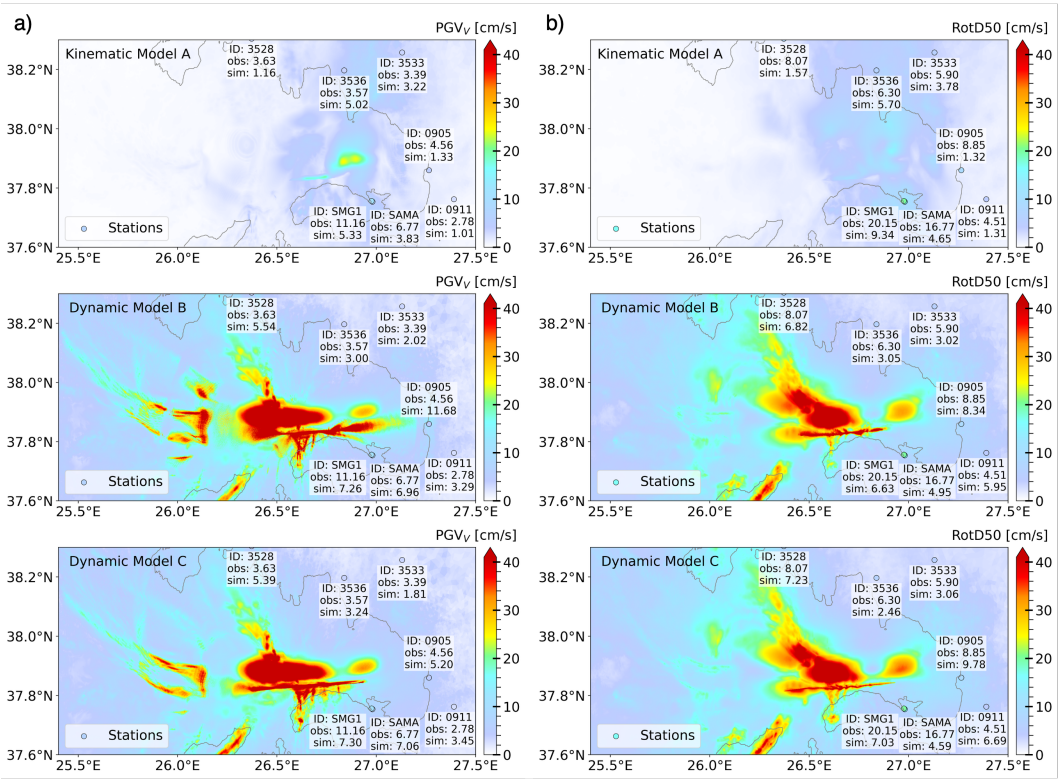


Figure 5. Ground motion comparison for the Kinematic Rupture Model A and two Dynamic Rupture Models B & C, evaluated against observations from Askan et al. (2021) at seven near-source coastal stations (that is, the location of the water layer). a) Vertical peak ground velocities (PGV_V) show how each rupture model reproduces the observed onshore vertical motions, with implications for the subsequent analysis of offshore vertical sea surface velocities. The root mean squared errors (RMSE) relative to the observations are 3.03 cm s^{-1}, 3.20 cm s^{-1}, and 1.75 cm s^{-1} for models A–C, respectively. b) The orientation-independent horizontal ground motion measure (RotD50; Boore, 2010) indicates that the strongest modeled horizontal motions of the two Dynamic Rupture Models B and C are concentrated offshore, toward the northwest. Background map colors display simulated ground motions processed using a second-order Butterworth bandpass filter, where the low-cut frequency is uniformly 0.1 Hz. Color-filled circles represent observed station values. Annotated values at Greek stations SMG1 and SAMA on Samos Island reflect station-matched low-cut filtering (0.05 Hz and 0.22 Hz, respectively) applied identically to both observed (Askan et al., 2021) and simulated records.

3.2 Tsunami generation and propagation

3.2.1 Tsunami propagation locally

The tsunami propagates from the source about 23 km northward within the first 6 min. The average water depth H over this distance is 470 m along profile 1 and 360 m along profile 2 (Supporting Information, Fig. S3). Using linear shallow-water theory (e.g., Talley et al., 2011; Levin & Nosov, 2015; Kundu et al., 2016), we can obtain an average velocity for the tsunami of about 68 m s^{-1} and 59 m s^{-1} for each profile, respectively. Figs. 6a, S4, S5 and Movies S2–S5 (Supporting Information) show the tsunami evolution following the different tsunami modeling approaches, masked for bathymetry deeper than 100 m and processed with a 2D spatial Butterworth low-pass filter using a cut-off wavelength $\lambda_c = 2$ km. Whether simulated with GeoClaw or SeisSol, all models of the tsunami share the same overall features. For example, at a simulation time of 6 min, we observe a leading wave drawdown of ∼0.4 m amplitude, expected from the normal faulting nature of the event, followed by a smaller ensuing wave crest towards the North (Fig. 6). Note that seismo-acoustic waves have left the acoustic medium by this time, and only the tsunami remains. North of Samos, the largest tsunami crest (∼0.5 m) propagates along the shoreline towards the western edge of the island. Between those two tsunami crests, a broader, more subtle wave drawdown is present. This pattern of the tsunami evolution is shared by all models regardless of the source model and technique used to simulate the tsunami. Because it remains challenging to observe differences by eye, we compute the difference between the various models (Supporting Information, Text S1). The leading wave drawdown of the tsunami is nearly identical between the one-way linked (GeoClaw) and fully coupled (SeisSol) tsunami modeling techniques, as indicated by the fact that no difference can be seen at this location after $t = 6$ min (Fig. 6b).

To quantitatively compare the highest tsunami peaks and troughs, we evaluate the mean of the top 0.1% largest sea surface height anomalies across the first 6 min of modeled tsunami generation. Although we explore the full modeling domain (Supporting Information, Fig. S6), we apply a 100 m water-depth threshold to exclude immediate coastal ssha distributions, where Ursell numbers reach $U \gg 1$ and SeisSol's linearized gravity-restoring free-surface boundary condition loses validity compared to the non-linear SWE used for one-way linked tsunami modeling. Sensitivity tests with varying bathymetric masking and low-pass filtering cut-off wavelengths can be found in the Supporting Information to this article (Fig. S6, S7, S8, S9), where differences between the models become smaller the larger the low-pass cut-off wavelength.

Sea surface height anomaly values are divided into peaks ($\text{ssha}^+ > 0$) and troughs ($\text{ssha}^- < 0$). For each distribution, we determine the 99.9th percentile ($P_{99.9}$), using positive ssha values for peaks and the absolute values of negative ssha for troughs, and calculate the mean of values in the corresponding most extreme 0.1% tail. The resulting conditional means, $\langle \text{ssha} \rangle^+_{99.9}$ and $\langle \text{ssha} \rangle^-_{99.9}$, retain their respective signs and provide representative measures of extreme crest and trough amplitudes. These metrics are annotated in each panel showing tsunami generation for the respective model and modeling technique, where we denote the (point-wise) difference field as $\langle \Delta\text{ssha} \rangle^{\pm}_{99.9}$, not to be confused with taking the difference of individual time series of the tsunami extrema. For the subtle wave drawdown following the leading trough and the tsunami peak near Samos island, the fully coupled tsunami simulations show additional wave packets not present in the one-way linked simulations. These shorter-wavelength, point-wise differences can reach ±0.1–0.2 m. The statistics are calculated after unifying the SeisSol and GeoClaw output formats (Supporting Information, Text S1).

In deeper water (>100 m), tracking of $\langle \text{ssha} \rangle^{\pm}_{99.9}$ over the first 6 min provides insights on how modeling approaches differ (Fig. 7). Although suppressed due to the low-pass filter applied, in the fully coupled Dynamic Rupture Models B & C, faster-propagating seismo-acoustic waves cause signals on the sea surface during the first ∼50 s of gener-

ation, which becomes more prominent when taking the difference for the respective models between the 3D fully coupled results using SeisSol and the 2D non-linear SWE results using GeoClaw. By excluding the initial 50 s and evaluating the tsunami extrema for 50–360 s, peak crest and trough metrics ($\langle \mathrm{ssha} \rangle^{\pm}_{99.9}$) agree within 0.10 m of each other across all time-dependent source models (i.e., Kinematic Model A and Dynamic Models B & C), with no systematic bias between these modeling frameworks.

For the Okada model, where we also compute $\langle \mathrm{ssha} \rangle^{\pm}_{99.9}$, we find larger discrepancies compared to the time-dependent tsunami modeling techniques. Over the same t =50–360 s window, comparing the instantaneous Okada solution to both 3D SeisSol and 2D GeoClaw time-dependent models indicates differences of up to ∼0.3 m (e.g., Fig. 8). However, part of this discrepancy reflects the timing difference between the modeled trough extrema and should not be interpreted as a persistent amplitude difference. For example, at $t = 360$ s, the trough amplitudes are nearly identical among all models (≈-0.5 m), despite the Okada model lacking contributions of the horizontal displacement to the vertical as well as a heterogeneous subsurface. In contrast, the Okada peak tsunami crest reaches only 0.35 m, compared with ∼0.5–0.6 m for all other models. Since the crests of all time-dependent models are still increasing at this time, the smaller Okada peak crest cannot be explained by the "earlier" instantaneous source. This indicates a difference in the generated crest amplitude that extends beyond the temporal offset between the source frameworks.

3.2.2 Seismic, acoustic, and gravity wave excitation

The addition of the water layer atop the elastic, solid Earth introduces a higher level of complexity in terms of physical waves generated by the self-consistent dynamic rupture process. For example, without a water layer, we expect "standard" solid Earth Rayleigh waves, which are generated due to the solid-air interface, that is, the (stress) free surface, propagating at approximately 92% of the shear wave velocity (Rayleigh, 1885). Due to the layered Earth model used, we expect them to be dispersive. An overlying water layer may also cause wave reverberations, as observed for trapped P-waves from Chilean earthquakes (Schwarze et al., 2026).

Another type of wave excitation that can be expected in fully coupled earthquake-tsunami simulations due to the presence of the elastic-acoustic (solid-fluid) interface are signals consistent with Scholte waves (Scholte, 1947). Scholte waves represent interface waves trapped at a solid–fluid boundary, forming an analogue to Stoneley waves that propagate along solid–solid boundaries (Stoneley, 1924). Such interface waves decay exponentially away from the solid–fluid interface (Rauch, 1980; Meegan et al., 1999) and are typically characterized by a phase velocity c_{Sch} that is slower than the acoustic speed of water c_0 and the shear speed of the solid (Vinh, 2013). Whereas interface waves at a homogeneous half-space interface are non-dispersive, in our modeling domain, signals consistent with Scholte waves exhibit strong dispersion, which we attribute to the layered subsurface velocity structure of the solid Earth and the finite water depth atop.

The overlying water column also alters the characteristics of the standard Rayleigh waves, commonly referred to as oceanic Rayleigh waves (c_{oR}) in this case. As discussed by Abrahams et al. (2023), these can be viewed as the generalization of acoustic wave modes in a rigid-bottomed ocean when accounting for the elasticity of the solid. Noguchi et al. (2016) have shown that oceanic Rayleigh waves travel slightly slower than Rayleigh waves modeled without a water layer. It is important to understand that such oceanic Rayleigh waves still propagate energy primarily within the upper layers of the solid Earth. However, through the elastic-acoustic coupling at the seafloor, the vertical component of the oceanic Rayleigh wave's elliptical motion dynamically perturbs the seafloor and creates a pressure wave in the water, which can reach the sea surface efficiently. The phase velocity of the water signals associated with oceanic Rayleigh waves is dispersive and gen-

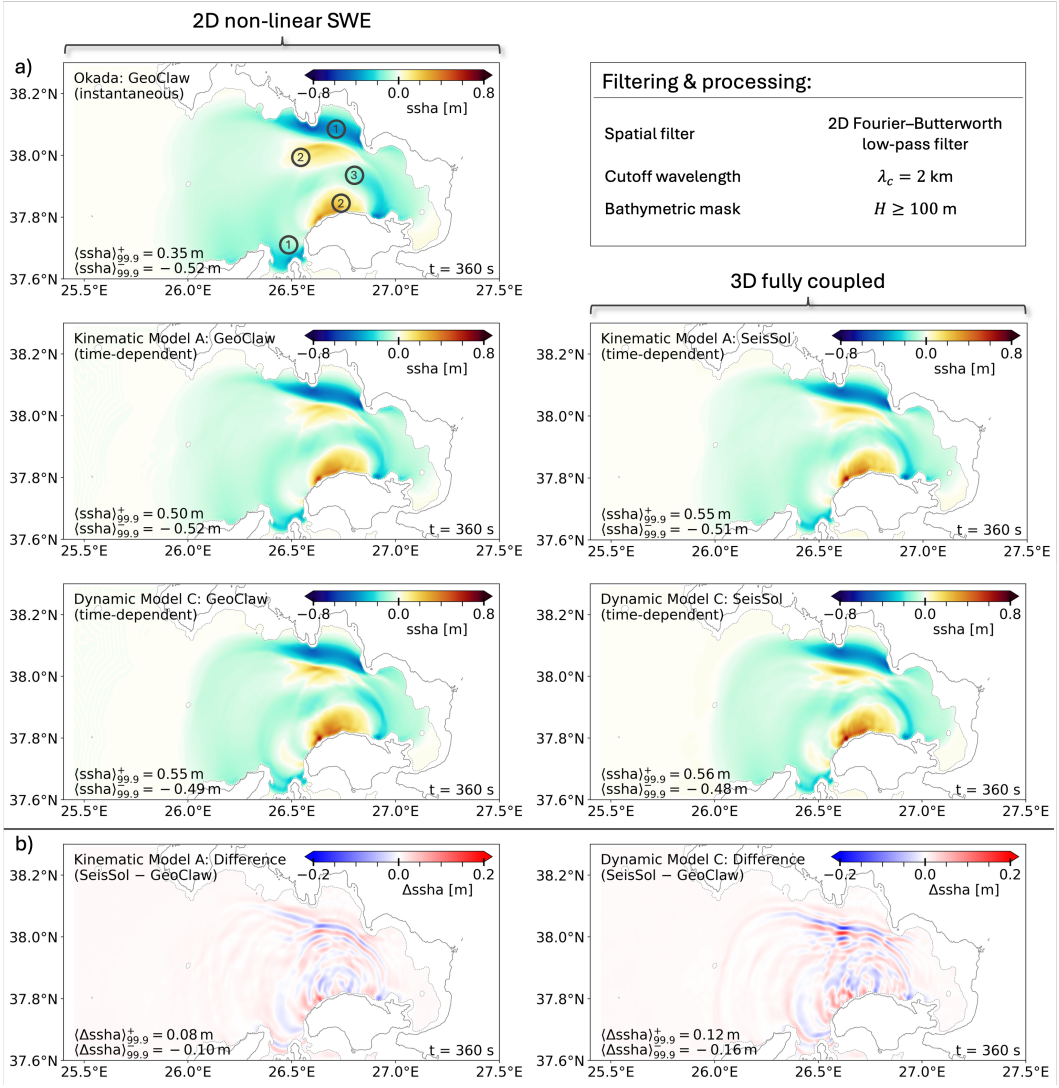


Figure 6. a) Snapshots of tsunami generation after 6 min, masked for bathymetry deeper than 100 m and processed with a 2D spatial Butterworth low-pass filter using a cut-off wavelength $\lambda_c = 2$ km, showing similar large-scale features across models: (1) an initial leading wave drawdown, followed by (2) peak tsunami crests, and (3) subtle sea surface depression in between. First column: three models of the tsunami using the non-linear shallow water equation (SWE) solver GeoClaw (Berger et al., 2011), informed by the instantaneous Okada displacement (Okada, 1985), and the time-dependent seafloor displacements of the Kinematic Rupture Model A and Dynamic Rupture Model C. Second column: fully coupled (3D time-dependent) tsunami generation with SeisSol (Gabriel et al., 2025) from the Kinematic Rupture Model A and the Dynamic Rupture Model C. Snapshots of the tsunami as generated by the Dynamic Rupture Model B are shown in Fig. S5 in Supporting Information. Annotations in the lower-left corner indicate the conditional mean sea surface height anomaly (ssha) of the most extreme 0.1% of wave crests and troughs. b) Differences in the generated tsunamis after 6 min between fully coupled (SeisSol) and one-way linked (GeoClaw) simulations of the same rupture models. Here, ssha metrics are calculated from the difference field between the fully coupled and one-way linked simulations.

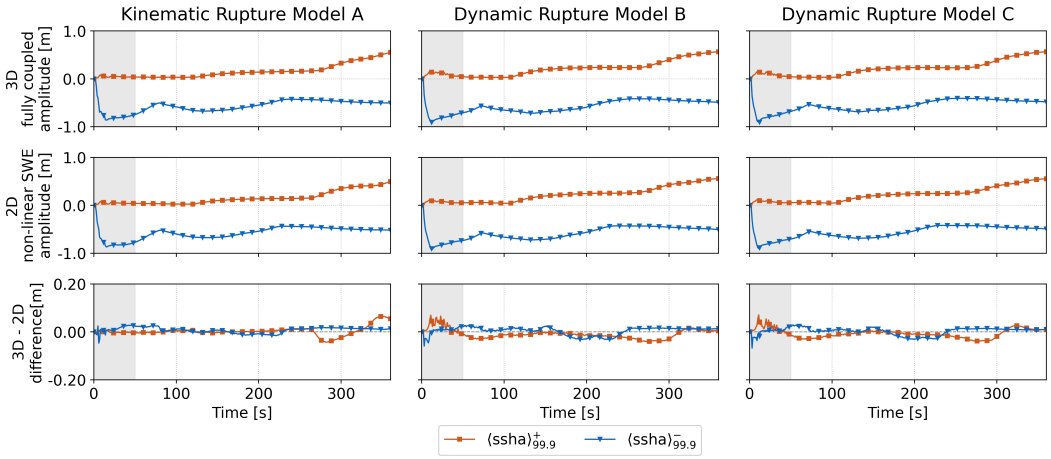


Figure 7. The top 0.1% largest sea surface height anomaly (ssha) amplitudes across the first 6 min of modeled tsunami generation. We use the Kinematic Rupture Model A and Dynamic Rupture Models B & C as sources for 3D fully coupled earthquake-tsunami and 2D non-linear shallow water equation (SWE) tsunami modeling. We mask each result for bathymetry deeper than 100 m and apply a 2D spatial Butterworth low-pass filter with a cut-off wavelength $\lambda_c = 2$ km. The trough metric ($\langle \text{ssha} \rangle^-_{99.9}$) tracks the initial time-dependent sea surface depression as a result of the normal-faulting earthquake, whereas the crest metric ($\langle \text{ssha} \rangle^+_{99.9}$) indicates low initial amplitudes before tsunami wave polarity reversal. Taking the difference, the imprint of seismo-acoustic waves (i.e., the "spikes") from the respective fully coupled simulation on both metrics can be seen during the first 50 s (gray shaded region).

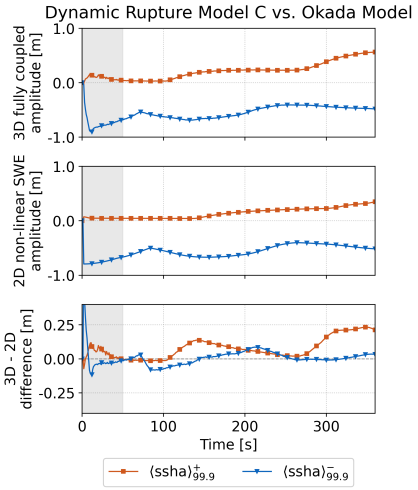


Figure 8. The top 0.1% largest sea surface height anomaly (ssha) amplitudes across the first 6 min of modeled tsunami generation, similar to Fig. 7. Here, we show the Dynamic Rupture Model C as a time-dependent source for 3D fully coupled earthquake-tsunami modeling, and the static Okada Model that informs 2D non-linear shallow water equations (SWE). We mask each result for bathymetry deeper than 100 m and apply a 2D spatial Butterworth low-pass filter with a cut-off wavelength $\lambda_c = 2$ km. The trough metric ($\langle \text{ssha} \rangle^-_{99.9}$) tracks the initial sea surface depression as a result of the normal-faulting earthquake, with an instantaneous drop for the Okada Model.

erally bounded between the Scholte and the standard Rayleigh wave velocities, that is $c_{Sch} < c_{oR} < c_R$ (Biot, 1952).

Fig. 9 and Fig. S10 show the space-time evolution of the sea surface vertical velocities (ssvv) when using the different modeling approaches for the two profiles in the north-south direction (Supporting Information, Fig. S3). All signals analyzed in the following correspond to those simulated at the sea surface, but reflect the underlying (dynamic) processes at the seafloor due to the shallow water depth. In the case of the instantaneous Okada-based tsunami generation, the wavefield is characterized by a clear wavefront that propagates without sudden, major changes in velocity, consistent with the relatively smooth bathymetry along profile 1. For Fig. S10 in Supporting Information and profile 2, a local depression in the bathymetry causes a bend in the simulated wavefront, leading to a short-lasting increase in the tsunami speed, as expected from linear shallow-water theory. No seismic waves are present in the Okada-based approach. As a result, no waves other than the tsunami exist, with occasional smaller tsunami reflections from the northern shoreline of Samos island. For Kinematic Rupture Model A, sea surface imprints of the prescribed time-dependent seafloor motion can be seen in the one-way linked simulation. However, as the kinematic rupture is prescribed, those signals may not necessarily reflect the true physical nature of seismic wave generation.

Recall that the Dynamic Rupture Models B & C share overall similar slip (Section 3.1.1), seafloor displacement (Section 3.1.2), and similar leading wave drawdown (this section). However, Dynamic Rupture Model C may be considered more realistic due to the depth-dependent initial normal stress and a slightly better fit to observed onshore vertical peak velocities (Section 3.1.3). Thus, we subsequently focus our analysis of the tsunami on Dynamic Rupture Model C, and provide tsunami simulation results of Dynamic Rupture Model B in the supplement.

For the time-dependent one-way linked tsunami simulation based on the Dynamic Rupture Model C, the first-arriving seismic waves, which translate into a transient disturbance of the sea surface, reflect those velocities associated with the first-arriving P-wave. This becomes even clearer in the fully coupled Dynamic Rupture Model C, where the fastest sea surface vertical velocities follow theoretical travel time curves of P- and solid Earth Rayleigh waves computed with TauP and ObsPy (Crotwell et al., 1999; Beyreuther et al., 2010), given the 1D velocity structure used for the elastic medium. For both the one-way linked Dynamic Rupture Model C and the fully coupled Dynamic Rupture Model C, (oceanic) Rayleigh wave dispersion due to the layered subsurface structure of the elastic medium imprints as transient signals at the sea surface. In the fully coupled models, it is evident that additional dispersive seismic wave signals, which we identify as so-called Scholte waves (Section 4), and acoustic waves are present in between these first-arriving signals and the much slower tsunami.

The ocean acoustic wavefield supports multiple modes. Following Abrahams et al. (2023), we calculate the minimum group velocities of ocean acoustic modes 1 and 2 using thickness-weighted average material parameters from the upper four layers (to a depth of 16 km) of the velocity model from Novotný et al. (2001) for the underlying solid Earth. The minimum group velocity of ocean acoustic mode 1 is 1.125 km s^{-1}, and its signature is more apparent when bandpass-filtering the space-time evolution between 0.5 and 2.0 Hz (Supporting Information, Fig. S11). Although we also calculate the minimum group velocity of ocean acoustic mode 2 (Supporting Information, Fig. S12), signals attributable to this higher-order mode cannot be clearly identified in the simulations. Signals consistent with the aforementioned Scholte waves are more visible when bandpass-filtering between 0.1 and 0.5 Hz (Fig. 9c).

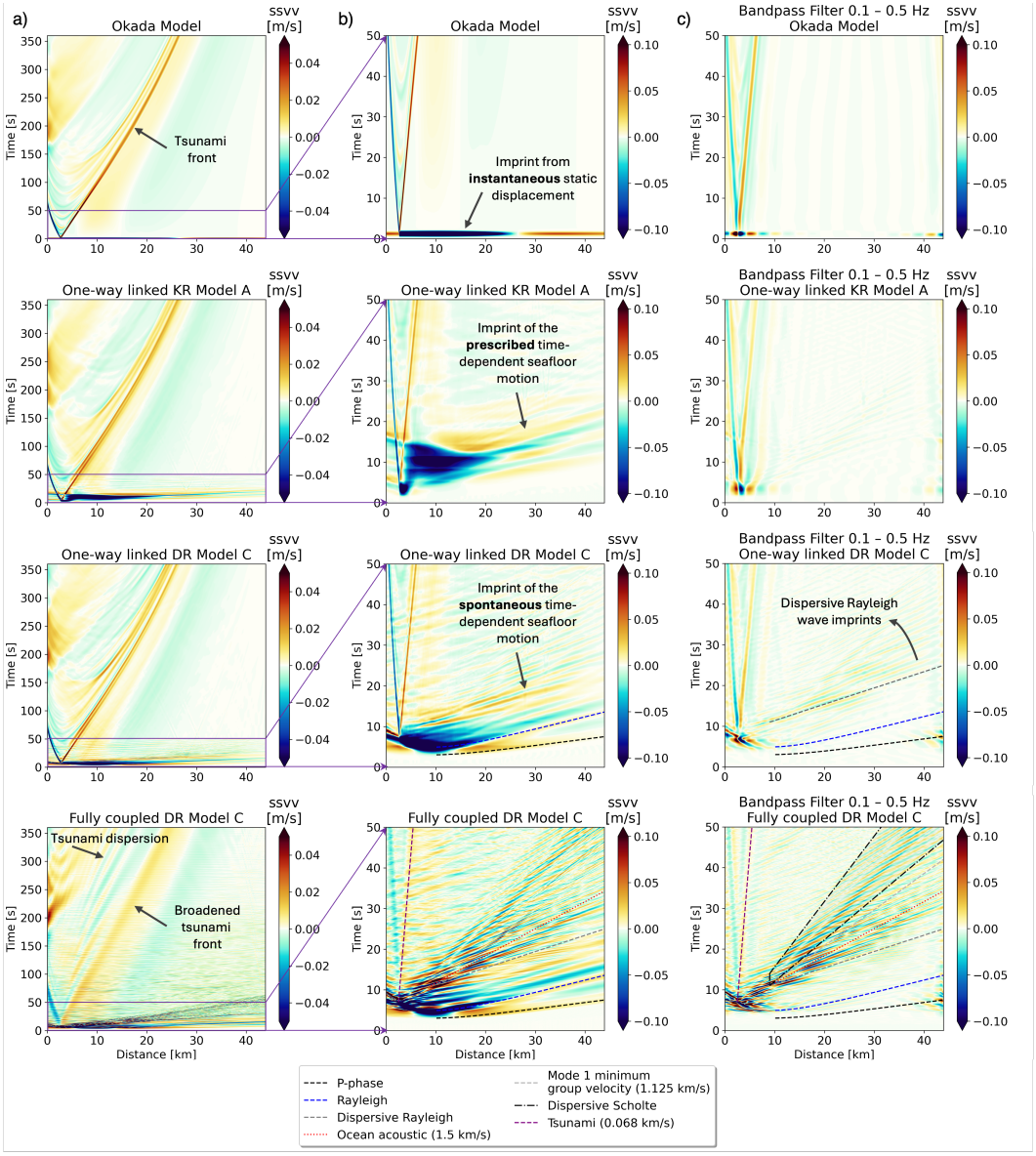


Figure 9. Space-time evolution of the tsunami generation along Profile 1 (see Fig. 1) for a) the first 6 min of simulation time, focusing on the tsunami (gravity wave) front. b) The first 50 s highlight the additional complexity of seismo-acoustic waves present in fully coupled models. Recall that the first 50 s of simulated time of the Kinematic Rupture (KR) Model A and Dynamic Rupture (DR) Model C are equally used for the time-dependent sourcing of the one-way linked GeoClaw simulations, whereas the fully coupled simulations are inherently time-dependent. c) Same scale as b), but with a bandpass filter of 0.1–0.5 Hz applied, highlighting signals consistent with dispersive Scholte waves in the fully coupled simulation, which are absent in the one-way linked simulations. Ocean acoustic modes are not clearly distinguishable in this frequency band. c) The same 50-second window using a 0.1 to 0.5 Hertz bandpass filter. This filtered view highlights signals consistent with dispersive Scholte waves in the fully coupled simulation. Ocean acoustic modes are not clearly distinguishable in this frequency band.

3.2.3 Spectral analysis of tsunami generation

Whereas the space–time evolution provides an intuitive visualization of the temporal evolution of wave signals across distance, an f–k analysis offers a complementary perspective by decomposing the wavefield into its spectral components (Supporting Information, Text S1). This analysis allows a clearer identification of dispersion characteristics, propagation velocities, and the presence or absence of different wave types. Fig. 10 shows the results of the two-dimensional f-k spectrum for the Okada modeling results, one-way linked Kinematic Rupture Model A, one-way linked Dynamic Rupture Model C, and fully coupled Dynamic Rupture Model C. All simulations using the non-linear shallow water equations show a clear non-dispersive tsunami signal. Neither the Okada simulation nor the one-way linked simulations include acoustic waves, but both of them show an imprint of the permanent seafloor displacement. In the spectra for the one-way linked Models A & C, we can see seismic wave signals attributed to P-waves and dispersive Rayleigh waves. Their signature overlaps with the frequencies held by acoustic waves in the fully coupled model. In the fully coupled model, dominant acoustic wave energy propagates along the ocean acoustic sound speed $c_0 = 1500$ m s^{-1} and is mostly constrained below $\sim$3 Hz, in close agreement with the nominal acoustic resolution limit (2.7 Hz; Section 2.6). However, fainter, lower-amplitude acoustic energy does extend to higher frequencies and may lie beyond numerical resolution, reflecting, e.g., numerical dispersion, and is therefore not interpreted further. At the mode 1 minimum group velocity (slower than c_0), physical wavelengths fall below our minimum resolved wavelength at frequencies above $\sim$2.0 Hz, defining the resolution limit for this specific branch. Conversely, the spectral energy extending up to $\sim$5 Hz appears broader and more diffuse, forming a smeared-out signature rather than a single discrete dispersion branch. Finally, we note that the tsunami signal is less clear in the fully coupled spectrum and does not follow the simple theoretical line ($k = 2\pi f/v$) when informed by the average tsunami propagation speed calculated earlier. However, this is to be expected from the dispersive nature of the tsunami in the fully coupled modeling framework.

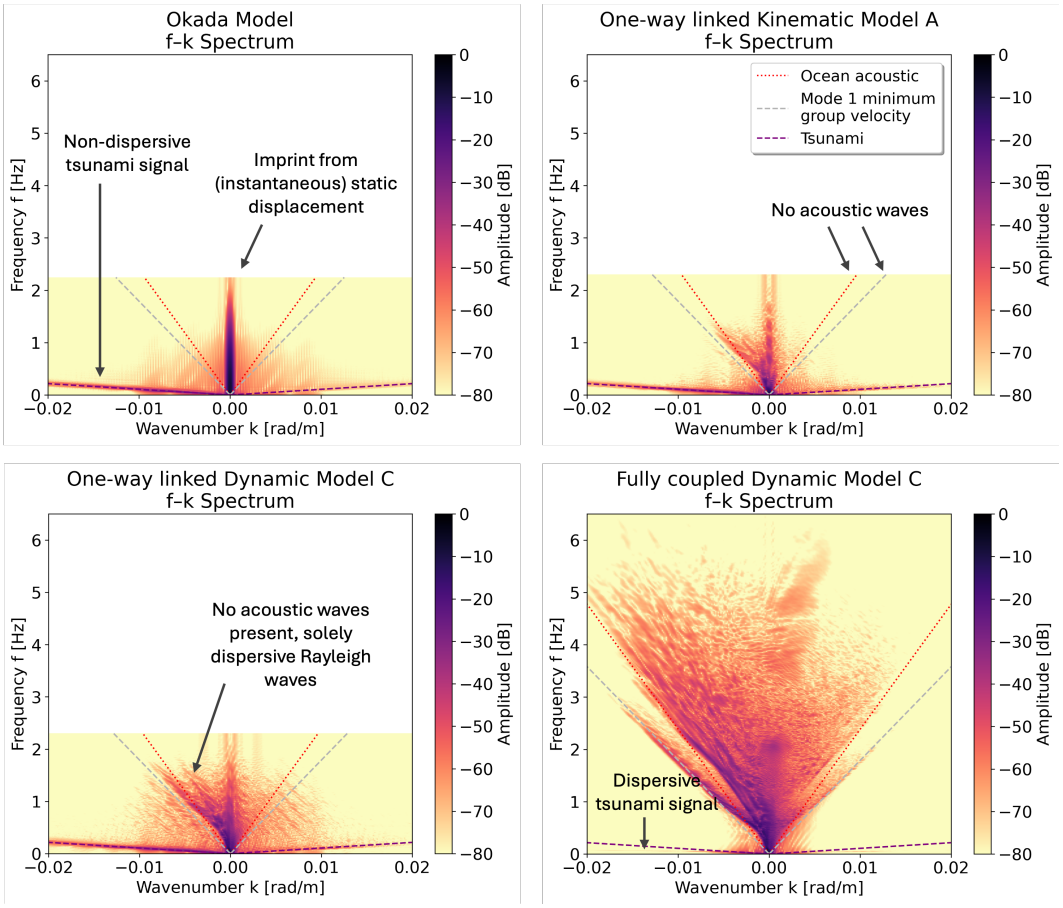


Figure 10. Frequency–wavenumber (f–k) spectrum of the simulated vertical velocity wavefields using the different tsunami modeling approaches. Amplitudes are normalized, converted to decibels, and clipped at –80 dB. Constant-velocity (non-dispersive) reference lines ($k = 2\pi f/v$) are overlaid for selected wave speeds from Fig. 9. The Okada and one-way linked models show a clear non-dispersive tsunami signal, but no acoustic wave excitation. For the tsunamis simulated with the non-linear shallow water equations (e.g., Okada and one-way linked models), the maximum frequency is limited by the Nyquist frequency of ∼2.3 Hz. In contrast, the fully coupled Dynamic Rupture Model C shows signals consistent with highly dispersive oceanic Rayleigh and Scholte waves as well as acoustic waves and a faint dispersive tsunami signal, highlighting the complexity of coupled elastic-acoustic (that is, solid-fluid) interactions.

4 Discussion

4.1 Tsunamigenesis in the Mediterranean Sea

Normal-faulting tsunamigenesis remains comparatively understudied relative to subduction zone events, including in the Mediterranean Sea, where tsunami modeling studies have mostly concentrated on the Hellenic Arc subduction system (S. Tinti et al., 2005; Lorito et al., 2008; Yolsal-Çevikbilen & Taymaz, 2012; Wirp et al., 2026). This region is characterized by high rates of seismicity (Benetatos et al., 2004; Herman et al., 2015) and has hosted (pre-)historic, devastating events (e.g., Stiros, 2001; England et al., 2015), including the AD 365 and AD 1303 tsunamigenic earthquakes. However, seismicity and tectonic deformation in this region are also driven by active normal faults (e.g., Mouslopoulou et al., 2015, 2025). The 2020 M_W 7.0 Samos earthquake, which ruptured in the extension-driven Aegean Sea region further north of the Hellenic Arc, serves as a well-documented event through which normal faulting tsunami generation can be studied in detail.

We systematically increase the tsunami modeling complexity for this offshore earthquake, from conventional instantaneous Okada-type sourcing using non-linear shallow water equations to both time-dependent kinematic and dynamic rupture sources and 3D fully coupled earthquake-tsunami simulations, untangling different contributions during tsunami generation. For that purpose, we utilize the planar fault geometry of Plicka et al. (2022), but do not consider potential secondary, adjacent faults (Fountoulakis et al., 2023).

4.2 Comparison of Samos rupture characteristics with existing source models

The earthquake rupture models considered here all reproduce the observed moment magnitude, with M_W of 7.03, 6.99, and 6.97, for Kinematic Rupture Model A and the Dynamic Rupture Models B & C, respectively. With peak slips between 2.4–2.6 m, these models are very consistent with the ∼2.4 m of maximum inferred slip by Plicka et al. (2022) and fall within the range of other inferred fault slip estimates. For example, Lentas et al. (2021) obtained a maximum slip of 2.5 m, Chousianitis and Konca (2021) of 4.6 m, and Kiratzi et al. (2022) of 3.5 m, whereas Karakostas et al. (2021) inverted a maximum slip of only 1 m. The north-dipping model of Hu et al. (2022) has 3.6 m of peak slip, the preferred kinematic model of Taymaz et al. (2022) shows 3.2 m, and the kinematic slip model of Sun et al. (2024) has ∼3.3 m of peak slip.

The rupture duration of the Dynamic Rupture Models B & C is ∼18 s and ∼17 s, respectively, close to the shorter estimates of the rupture duration for the Samos earthquake (Fig. 4). Here, shorter rupture durations include ∼16 s from Kiratzi et al. (2022), and ∼15 s from Lentas et al. (2021) as well as Karakostas et al. (2021), where the latter had an additional, much smaller, distinct later pulse. Longer inferences of rupture durations include those of Chousianitis and Konca (2021), where the rupture duration is ∼32 s, but with most of the seismic moment release within the first 20 s, which is also the rupture duration obtained by Sun et al. (2024) and Plicka et al. (2022). The preferred kinematic rupture of Taymaz et al. (2022) lasts 26 s, but their dynamic rupture simulation based on this model only sustains for nearly 16 s after nucleation, thus more in line with our dynamic rupture simulations. One difference is that the dynamic rupture model of Taymaz et al. (2022) was simulated in a full space without a free surface, whereas we include the complex bathymetry and topography of the region, which can have large effects on the dynamics of earthquake rupture (e.g., Oglesby et al., 1998, 2000). However, note that the moment rate functions of the earthquake rupture models considered here appear smoother than those of previous studies (Fig. 4). We attribute this to the smoothing of the finite-fault slip model of Plicka et al. (2022) (with subfault dimensions of 2.5×2.0 km along-strike and along-dip) when it is used as input for the kinematic rup-

ture simulation and subsequently dynamic rupture simulations with SeisSol (each with 200 m on-fault resolution). Moreover, we use regularized Yoffe functions of slightly asymmetric shape for Kinematic Rupture Model A, which better represent the physically expected rapid slip onset followed by a longer slip-rate decay compared to symmetric source time functions (e.g., Latour et al., 2025). However, this representation may introduce an additional component of smoothing to the moment rate.

The dynamic rupture models exhibit spatially variable rake, in contrast to the constant -110° rake prescribed in Kinematic Rupture Model A (Supporting Information, Fig. S13), inherited directly from the reference finite-fault model of Plicka et al. (2022). Specifically, although both dynamic rupture models prescribe pure normal faulting (-90° rake), Dynamic Rupture Models B & C develop minor secondary strike-slip motion during rupture propagation. Such dynamic rake rotation has been inferred from curved geological slip indicators, is governed by transient dynamic stress concentrations at the propagating rupture front, and is modulated by the background stress state (Guatteri & Spudich, 1998; Spudich et al., 1998; Kearse et al., 2019; Kearse & Kaneko, 2020). This secondary strike-slip motion is more pronounced near the surface in Dynamic Model C due to its depth-dependent initial effective normal stress setup.

Ultimately, we select Dynamic Rupture Model C as the preferred dynamic rupture model primarily due to its higher physical realism through incorporating depth-dependent initial effective normal stress, supported by directivity evidence at station 0905 where Model B (uniform initial effective normal stress) overshoots the observed vertical peak ground velocity by ∼2.6 times. However, we note that no geotechnical layer and site-specific V_{s30} velocities (i.e., average shear wave velocity in the upper 30 m), viscoelastic attenuation (e.g., Day, 1998; Kristek & Moczo, 2003; Taufiqurrahman et al., 2022), or nonlinear wave propagation effects (e.g., Bonilla et al., 2005; Roten et al., 2014; Niu et al., 2025) have been incorporated into our models, which may affect the simulated ground motions. Despite our simulations omitting such effects, our modeled vertical and horizontal ground motions agree to first order with the observed peak velocity records reported by Askan et al. (2021) across near-source coastal stations, with stations SMG1 and SAMA marking exceptions for horizontal ground motion measures. This comparison suggests that shallow site effects can contribute locally, but that the overall ground motion and peak velocities in the near-source region may still be dictated by fault geometry, rupture directivity, and linear wave propagation. In addition, the simulated ground motions from the dynamic rupture models show elevated shaking across areas characterized by steeper topography, such as Ikaria island west-southwest of Samos and Mount Kerkis in western Samos. Although such an effect of topography on ground motion has been reported for mountainous terrain (e.g., Lee et al., 2009; Hartzell et al., 2013), we lack corresponding observations for validation and note that the velocity in the shallowest layer of the used 1D velocity model (Novotný et al., 2001) is simply extended to all elevations above sea level. Similarly, a bathymetric rise north of Ikaria island results in enhanced vertical peak ground velocities, which may have important implications for secondary hazards such as landslide-generated tsunamis.

4.3 Tsunami generation, propagation, and comparison with tsunami models

Earlier studies have modeled the tsunami generated by the 2020 Samos earthquake using finite-fault models (e.g., Heidarzadeh et al., 2021; Hu et al., 2022; C. Ren et al., 2022; Sun et al., 2024). Although not the focus of this study, we compare tide gauge observations across the Aegean Sea with the simulated one-way linked tsunami waveforms based on Dynamic Rupture Model C (Supporting Information, Figs. S14, S15). The tidal-trend removal at the tide gauges is detailed in Section 2.5.2. Despite the relatively coarse bathymetry grid adopted here (GEBCO Bathymetric Compilation Group, 2022), which we choose for a consistent comparison between one-way linked and fully coupled mod-

els, the one-way linked Dynamic Rupture Model C captures the overall tsunami wave periods and relative amplitudes at tide gauge Syros. However, an initial arrival discrepancy is present at this station, likely due to instrumental malfunction missing the early part of the recording as reported by C. Ren et al. (2022). Unfortunately, no tide gauges closer to the source were available at the time of the Samos earthquake and tsunami, highlighting the need for a denser offshore instrumentation network in the Aegean Sea. Coverage could be improved with (a) the placement of more tide gauges, (b) submerged fiber-optic sensing techniques (i.e., distributed acoustic sensing; DAS) for tsunami detection (e.g., Xiao et al., 2024; Tonegawa & Araki, 2024; Becerril et al., 2026), or (c) SWOT-based tsunami analysis (Roger et al., 2026; Sepúlveda et al., 2026), although the latter may be complicated due to the presence of the many small islands within the Aegean Sea.

Bathymetric resolution is well known to influence tsunami simulations (e.g., Sepúlveda et al., 2020; Gibbons et al., 2022; Felix et al., 2024). For the 2020 Samos event, Sun et al. (2024) have already investigated different levels of bathymetric resolution and showed that simulated peak amplitudes at Syros can differ by nearly 170% when using a 3.75 arcsec instead of 15 arcsec resolution (Supporting Information, Fig. S15). The one-way linked Dynamic Rupture Model C fails to accurately reproduce tsunami waveforms at stations other than Syros. This mismatch can likely be attributed not only to a coarser bathymetric resolution adopted here, but also to the use of non-dispersive shallow water equations in the one-way linked setup. Future work may explore the use of a Boussinesq-type dispersive system for shallow water equations, such as the Serre-Green-Naghdi equations in GeoClaw (Berger & LeVeque, 2024), with a strong dispersion directivity for $M_W < 8$ earthquakes (Glimsdal et al., 2013). We note that dispersion is accounted for in the fully coupled simulation. However, computational limitations and meshing challenges posed by the many small islands in the Aegean prevented extending the coupled model to the region, capturing these far-field stations (Wirp et al., 2026). We also note that we did not include off-fault plasticity, which may enhance the vertical seafloor displacement (e.g., Ma, 2023; Biemiller et al., 2023; Wirp et al., 2026). Another factor tsunami generation remains sensitive to is dynamic source complexity, such as dynamic rake rotation (Kutschera, Gabriel, et al., 2024), which is present in the two Dynamic Rupture Models B & C. Although both dynamic rupture simulations produce extended surface-breaking slip compared to the Kinematic Rupture Model A and its more localized surface rupture, the lack of direct offshore surface-rupture observations leaves the extent of shallow slip unvalidated, and thus also affects tsunami amplitude estimates.

For water depth $H > 100$ m, tracking peak crests and troughs ($\langle \text{ssha} \rangle^{\pm}_{99.9}$) across the first 6 min shows close agreement between 3D fully coupled and 2D time-dependent non-linear shallow water equation tsunami simulations, with the crest and trough metrics matching within 0.10 m across all time-dependent source models without a systematic amplitude bias once transient seismo-acoustic waves have left the source area. In contrast, assuming an instantaneous Okada source increases tsunami extrema discrepancies relative to time-dependent models by a factor of ~ 3 (up to ~ 0.30 m), driven by the smaller Okada peak crest rather than by a persistent trough difference (Section 3.2). Additionally, we observe smaller discrepancies in the evolving wavefield between time-dependent frameworks, corresponding to trailing waves. We interpret these localized (pointwise) wavefield differences as driven by two main physical and hydrodynamic processes that differ between modeling frameworks: First, 3D fully coupled modeling inherently includes the water-column low-pass filtering of short-wavelength seafloor deformation (Section 2.5.1). Second, physical frequency dispersion in the 3D water layer spreads wave energy in time and space, smoothing trailing wave crests compared to non-dispersive shallow water equations. In addition, differing near-shore treatment may influence offshore wavefields through shoreline reflections, although of minor influence here given the bathymetric masking and short initial simulation time comparison. Lastly, numerical discretization and any type of mesh refinement can, in principle, affect tsunami amplitude esti-

mates. In our simulations, the sea surface height anomaly differences for $H > 100$ m between the one-way linked and fully coupled models do not show a systematic bias toward higher or lower amplitudes. Instead, deviations remain localized and oscillate around zero, indicating that although discretization differences inherent to the numerical schemes exist, they are unlikely to be the primary cause of the observed wavefield differences.

4.4 Seismic, acoustic, and interface waves contributions during tsunami excitation

By design, shallow water equations (SWE) do not include ocean acoustic waves. They may capture tsunami dispersion through the Boussinesq approximation, which can be of importance to constrain the presence of shallow slip (e.g., Wilson & Ma, 2021; Sepúlveda et al., 2026). However, here we use the non-linear SWE without tsunami dispersion instead, which we inform by (i) instantaneous Okada-displacement and the time-dependent seafloor displacement of the earthquake (ii) kinematic and (iii) dynamic rupture models. For the Okada model using SWE, only the tsunami can be present, without additional contributions from seismic or acoustic waves. Note that no bathymetry is incorporated when calculating the Okada displacement, which can affect the ground deformation (Langer et al., 2019), especially in areas with steep bathymetric gradients (Hsu et al., 2011). On the contrary, even a noticeable variation (± 0.1) from the assumed Poisson's ratio of 0.25 changes the modeled subsidence by only $\sim \pm 4$ cm (Supporting Information, Fig. S16). For the Kinematic Rupture Model A with bathymetry, simulated using SWE, transient sea surface signals can be forced by P waves reaching the seafloor and Rayleigh waves propagating along the solid surface, whereas Scholte waves and ocean acoustic modes remain absent. These latter-occurring signals are only excited in the (iv) fully coupled earthquake–tsunami simulations, where the presence of an elastic–acoustic interface permits their generation. The dynamic rupture models include Rayleigh wave dispersion due to the layered solid Earth (elastic medium). With an added water layer (acoustic medium) on top of the solid medium in the fully coupled modeling framework, we can account for tsunami dispersion (e.g., Lotto & Dunham, 2015; Wilson & Ma, 2021; Kutschera, Gabriel, et al., 2024). Due to the presence of an elastic-acoustic (solid-fluid) interface in the 3D fully coupled earthquake-tsunami simulations, we expect the presence of signals consistent with Scholte waves, which have long been found to develop at such an interface (Scholte, 1947).

As the fault continues to break and the rupture propagates, seismic waves are continuously emitted. Rayleigh waves, which travel along a free surface, such as the solid-air interface, are well-known; other types of waves propagating along a material property discontinuity are discussed less frequently. Scholte waves have also been observed for glacier ablation processes (Gräff et al., 2025). From theoretical considerations (e.g., Vinh, 2013), we know that the Scholte wave velocity is always smaller than the P-wave velocity c_P, the Rayleigh wave velocity c_R, and acoustic wave velocity c_0, that is $c_{Sch} < \min(c_P, c_R, c_0)$, which helps to discern the various signals when plotting the space-time evolution of sea surface vertical velocities. Strong Scholte waves can be generated either from a source located at the seafloor or by interactions with a non-uniform bathymetry (Zheng et al., 2013). It is important to note that even though we expect a decay of these large amplitudes away from the elastic-acoustic interface, the shallow local bathymetry (generally <500 m) allows the corresponding pressure signals to propagate all the way to the sea surface (Section 3.2.2).

In our f-k spectrum for the fully coupled Dynamic Rupture Model C, we observe that the frequency content of dispersive oceanic Rayleigh waves and signals consistent with dispersive Scholte waves overlap. However, since Scholte waves trapped at the solid-fluid interface share characteristics with oceanic Rayleigh waves, they also inherit the same frequency content as the generating Rayleigh waves. Thus, it is expected that their contributions are challenging to distinguish in the f-k spectrum. In contrast, for the one-

way linked GeoClaw simulations, all transient signals have to originate from body waves and dispersive Rayleigh waves, since neither acoustic nor Scholte waves are permitted. In the f-k spectrum for the fully coupled model, we further observe that ocean acoustic waves may be partially hidden among such seismic wave signals. However, by filtering the corresponding space-time evolution in different frequency bands, individual signals can be more easily discerned. In our case, a bandpass filter between 0.1 and 0.5 Hz highlights dispersive Scholte waves, whereas a bandpass filter at slightly higher frequencies of 0.5–2.0 Hz causes the signature associated with ocean acoustic mode 1 to appear more clearly.

The tsunami extrema in the time-dependent frameworks agree within 0.10 m after the first ∼50 s, during which transient seismo-acoustic waves are most apparent. The instantaneous Okada source differs by up to ∼0.3 m, a factor of three larger but still modest compared with the framework dependence reported previously. Earlier 3D fully coupled studies focus on large-magnitude, long-duration megathrust events (e.g., Maeda et al., 2013; Wilson & Ma, 2021; Du & Ma, 2025; Wirp et al., 2026; Henneking et al., 2026) and multi-fault strike-slip earthquakes with pronounced surface rupture (e.g., Krenz et al., 2021; Kutschera, Gabriel, et al., 2024). The Samos models presented here rupture a single planar normal fault over ∼17–23 s and ∼1000 km^2, with only localized surface rupture beneath shallow water depths.

Abrahams et al. (2023) show that the applicability of different modeling frameworks depends on source duration and horizontal dimension relative to tsunami propagation timescales and water depth. For their example with $H = 4$ km water depth, shallow water equation simulations overestimate tsunami amplitudes by a factor of two when no Kajiura-type filter is applied. This is governed by the non-dimensional product kH via the non-hydrostatic correction $1/\cosh(kH)$ (Section 2.5.1). For the 10–20 km deformation wavelengths and $H \approx 400$ m relevant here, $kH \lesssim 0.25$ and the correction stays below ∼3%. At $H = 4$ km, a 20 km deformation wavelength gives $kH \approx 1.26$ and an overestimation factor of ∼1.9, consistent with the factor of two reported by Abrahams et al. (2023). The shallow bathymetry north of Samos therefore places this event in a regime where the modeling frameworks are expected to converge. This agreement is not an artifact of our post-processing, since the metrics remain comparable without the 2 km spatial low-pass filter (Supporting Information, Fig. S7). Separating the individual contributions of bathymetry, source duration, and rupture geometry requires further work on segmented or multi-fault normal-faulting ruptures and on longer rupture durations (e.g., Biemiller et al., 2023; Leclerc et al., 2024).

4.5 Implications for tsunami early warning and hazard assessment

Accurate and timely understanding of tsunami generation from offshore earthquakes remains a critical challenge for hazard assessment and early warning systems (Rea et al., 2025). For the 2020 Samos event, the Italian tsunami alert center issued a watch alert 8 min after the origin time of the earthquake (Amato et al., 2021). These initial minutes of the tsunami excitation, involving the complex seafloor deformation and displacement of the water column together with the radiation of seismo-acoustic waves, are often poorly constrained due to a lack of dense offshore observational networks (e.g., Schmidt et al., 2019). This sparsity hinders the precise estimation of the initial sea surface characteristics and poses a challenge for real-time tsunami early warning (Satake, 2014). Recent observations show that Comprehensive Nuclear-Test-Ban Treaty Organization (CTBTO) hydrophones and ocean bottom DAS can provide complementary observations of earthquake-generated T-waves and support the detection of submarine earthquakes (Wu et al., 2023; Shen & Wu, 2024). Our results indicate that one-way linked approaches are computationally more efficient than fully coupled earthquake-tsunami modeling and yield comparable tsunami extrema beyond the first ∼50 s in water deeper than 100 m. However, they cannot capture the full physical complexity in the near-source region of a shallow

offshore rupture. Thus, for any detailed reconstructions of (shallow) tsunamigenic events, where different ocean acoustic modes, (dispersive) seismic wave signals, and gravity waves need to be differentiated, the fully coupled method should be used. Furthermore, if tsunami early warning systems were based on the detection of ocean acoustic (Cecioni et al., 2014; Kadri et al., 2025) rather than gravity waves and associated pressure changes as captured e.g., by the Deep-ocean Assessment and Reporting of Tsunamis (DART) system (Gonzalez et al., 1998; Mungov et al., 2013), a one-way linked method is no longer sufficient, and simulated signals in fully coupled models may help in the identification of real-world signals.

5 Conclusions

We present two 3D dynamic rupture models with magnitudes of M_W 6.99 and M_W 6.97 for the 2020 M_W 7.0 Samos earthquake that incorporate realistic bathymetry. The preferred dynamic rupture model is set up using a depth-dependent initial effective normal stress and matches observed near-source vertical peak ground velocities with a root mean squared error of 1.75 cm s^{-1}. Its advantage over a dynamic rupture model assuming uniform, depth-independent initial effective normal stress is driven by fitting station 0905. We systematically increase tsunami generation modeling complexity by using a reference finite-fault slip model, a kinematic model, and both dynamic rupture models as tsunami sources of increasing physical consistency. We compare tsunami modeling techniques that cover conventional instantaneous Okada-informed non-linear shallow water equations, time-dependent one-way linked non-linear shallow water equations, and 3D fully coupled elastic-acoustic-gravity simulations.

In the fully coupled simulations, we identify dispersive oceanic Rayleigh waves, signals consistent with dispersive Scholte waves, and mode 1 ocean acoustic waves superimposed onto the gravity-driven tsunami. All time-dependent earthquake-tsunami modeling techniques yield comparable final seafloor subsidence and nearly identical tsunami leading wave characteristics with similar trailing large-scale features. Transient discrepancies in the evolving wavefield are restricted to smaller, trailing waves, which we interpret as driven by 3D frequency dispersion and water-column low-pass filtering of short-wavelength seafloor deformation. To compare tsunami extrema across modeling frameworks, we use the means of the most extreme 0.1% of positive and negative sea surface height anomalies. For each time-dependent source, peak crests and troughs of the one-way linked and fully coupled simulations agree within 0.10 m between 50 and 360 s in water deeper than 100 m. The Okada peak tsunami troughs are driven by the source timing, whereas the smaller Okada peak crest (0.35 m against 0.5–0.6 m) persists despite the timing difference. Since instantaneous Okada sourcing is common in tsunami hazard assessment, this crest difference is relevant beyond the Samos event.

The Samos earthquake highlights that normal-faulting events in regions of active crustal extension can produce tsunamis whose initial generation contains superimposed seismic, acoustic, and gravity wave contributions. For events with source and bathymetric scales comparable to Samos, time-dependent one-way linked shallow water equation frameworks offer an efficient approach for estimating large-scale tsunami generation and propagation. However, agreement in large-scale tsunami characteristics does not imply equivalence of the initial near-source wavefields, which may vary for longer rupture durations, segmented or multi-fault ruptures, or substantially different water depths.

Open Research

The open-source software SeisSol (`www.seissol.org`, commit a5b4269; Gabriel et al., 2025), available from GitHub (`https://github.com/SeisSol`), has been used for 3D dynamic rupture and fully coupled earthquake-tsunami modeling. We used GeoClaw version 5.11.0 (Clawpack Development Team, 2024), also available from GitHub (`https://`

github.com/clawpack/geoclaw), for non-linear shallow water equation tsunami simulations. The finite-fault model of Plicka et al. (2022) can be found online at SRCMOD (http://equake-rc.info/srcmod; Mai & Thingbaijam, 2014). We follow the steps of Ulrich et al. (2022) to convert the SeisSol output to GeoClaw input. The SeisSol and tsunami input files required to run the simulations can be obtained from https://doi.org/10.5281/zenodo.18637304 (Kutschera & Gabriel, 2026). This includes a smaller test scenario for the preferred Samos dynamic rupture-only model in this study, which can be run on Quakeworx, a science gateway for seismic simulations with community access (https://quakeworx.org; Chourasia et al., 2024; Rekoske et al., 2026). Additional SeisSol training material is available at https://github.com/SeisSol/Training. Surface displacements were calculated based on the elastic dislocation model of Okada (1985) using the okada4py Python implementation (Jolivet, 2024), available from GitHub (https://github.com/jolivetr/okada4py), which wraps the generalized internal deformation formulation of Okada (1992). Tsunami waveforms are obtained from the Flanders Marine Institute (VLIZ), Intergovernmental Oceanographic Commission (IOC) (2026) (http://www.ioc-sealevelmonitoring.org) and the TAD (Tsunami Alert Device) server of the European Commission's Joint Research Centre (JRC; https://webcritech.jrc.ec.europa.eu). Statsmodels (Seabold & Perktold, 2010), scikit-learn (Pedregosa et al., 2011), NumPy (C. R. Harris et al., 2020), pandas (McKinney, 2010), and ObsPy (Beyreuther et al., 2010; Krischer et al., 2015) were used for data processing, Matplotlib (Hunter, 2007) and PyGMT (Tian et al., 2026) for plotting. We used Gmsh (Geuzaine & Remacle, 2009), SimModeler by Simmetrix (https://www.simmetrix.com), and PUMGen (https://github.com/SeisSol/PUMGen) for mesh generation. All links were last accessed on 16 July 2026. We incorporate the topography and bathymetry data by GEBCO Bathymetric Compilation Group (2022) using the following projection: `+proj=tmerc +datum=WGS84 +k=0.9996 +lon_0=26.25 +lat_0=37.75`. The Supporting Information to this article contains additional text (Text S1) and figures (Figures S1–S16). Supporting Movies S1–S5 are uploaded separately.

Acknowledgments

We thank František Gallovič, Ignacio Sepúlveda, Eric Dunham, Lauren Abrahams, Thomas Ulrich, and Aniko Wirp for fruitful discussions. We also appreciate the exchanges with Bo Li, Duo Li, and Mathilde Marchandon in the early stages of this work. FK and AAG acknowledge support from the National Science Foundation (NSF, Quakeworx, Grant OAC-2311208 and OAC-2139536), the National Aeronautics and Space Administration (NASA, Grant 80NSSC20K0495), the Cascadia Region Earthquake Science Center (CRESCENT), which is funded by NSF Cooperative Agreement EAR-2225286, the Statewide California Earthquake Center (SCEC), which is funded by NSF Cooperative Agreement EAR-2225216 and USGS Cooperative Agreement G26AC00077-00, and Horizon Europe (DT-GEO, grant No. 101058129). AAG acknowledges additional support from the National Science Foundation (NSF, Grant nos. EAR-2121568, RISE-2531036, OAC-2603524), the U.S. Geological Survey (Award G26AP00141), Horizon Europe (Grant nos. 101291194, 101093038, 101058518), and Pacific Gas and Electric Company (PG&E). We acknowledge the Gauss Centre for Supercomputing e.V. (www.gauss-centre.eu, project pn49ha) for funding this project by providing computing time on the GCS Supercomputer SuperMUC-NG at Leibniz Supercomputing Centre (www.lrz.de) and appreciate the computing infrastructure available at the Department of Earth and Environmental Sciences at Ludwig Maximilian University of Munich, Geophysics (Oeser et al., 2006). The authors declare no conflicts of interest relevant to this study.

References

Abrahams, L. S., Krenz, L., Dunham, E. M., Gabriel, A.-A., & Saito, T. (2023). Comparison of methods for coupled earthquake and tsunami modelling. *Geo-*

physical Journal International, *234*(1), 404–426. doi: 10.1093/gji/ggad053

Aki, K., & Richards, P. G. (2002). *Quantitative Seismology* (2nd ed.). University Science Books.

Akinci, A., Cheloni, D., & Dindar, A. A. (2021). The 30 October 2020, M7.0 Samos Island (Eastern Aegean Sea) Earthquake: Effects of source rupture, path and local-site conditions on the observed and simulated ground motions. *Bulletin of Earthquake Engineering*, *19*(12), 4745–4771. doi: 10.1007/S10518-021-01146-5

Altinok, Y., Alpar, B., Özer, N., & Gazioglu, C. (2005). 1881 and 1949 earthquakes at the Chios-Cesme Strait (Aegean Sea) and their relation to tsunamis. *Natural Hazards and Earth System Sciences*, *5*(5), 717–725. doi: 10.5194/nhess-5-717-2005

Álvarez-Gómez, J. A., Gutiérrez Gutiérrez, O. Q., Aniel-Quiroga, Í., & González, M. (2012). Tsunamigenic potential of outer-rise normal faults at the Middle America trench in Central America. *Tectonophysics*, *574–575*, 133–143. doi: 10.1016/j.tecto.2012.08.014

Amato, A., Avallone, A., Basili, R., Bernardi, F., Brizuela, B., Graziani, L., ... Volpe, M. (2021). From Seismic Monitoring to Tsunami Warning in the Mediterranean Sea. *Seismological Research Letters*, *92*(3), 1796–1816. doi: 10.1785/0220200437

Andrews, D. J. (1976). Rupture velocity of plane strain shear cracks. *Journal of Geophysical Research*, *81*(32), 5679–5687. doi: 10.1029/JB081I032P05679

Arcos, M. E., & LeVeque, R. J. (2015). Validating Velocities in the GeoClaw Tsunami Model Using Observations near Hawaii from the 2011 Tohoku Tsunami. *Pure and Applied Geophysics*, *172*(3-4), 849–867. doi: 10.1007/s00024-014-0980-y

Askan, A., Gülerce, Z., Roumelioti, Z., Sotiriadis, D., Melis, N. S., Altindal, A., ... Margaris, B. (2021). The Samos Island (Aegean Sea) M7.0 earthquake: Analysis and engineering implications of strong motion data. *Bulletin of Earthquake Engineering*, *20*(14), 7737–7762. doi: 10.1007/S10518-021-01251-5

Baba, T., Chikasada, N., Nakamura, Y., Fujie, G., Obana, K., Miura, S., & Kodaira, S. (2020). Deep Investigations of Outer-Rise Tsunami Characteristics Using Well-Mapped Normal Faults Along the Japan Trench. *Journal of Geophysical Research: Solid Earth*, *125*(10), e2020JB020060. doi: 10.1029/2020JB020060

Bale, D. S., LeVeque, R. J., Mitran, S., & Rossmanith, J. A. (2003). A Wave Propagation Method for Conservation Laws and Balance Laws with Spatially Varying Flux Functions. *SIAM Journal on Scientific Computing*, *24*(3), 955–978. doi: 10.1137/S106482750139738X

Bécel, A., Shillington, D. J., Delescluse, M., Nedimović, M. R., Abers, G. A., Saffer, D. M., ... Kuehn, H. (2017). Tsunamigenic structures in a creeping section of the Alaska subduction zone. *Nature Geoscience*, *10*(8), 609–613. doi: 10.1038/ngeo2990

Becerril, C., Sladen, A., Ampuero, J.-P., Preciado-Garbayo, J., Gonzalez-Herraez, M., Kutschera, F., ... Bouchette, F. (2026). Towards Tsunami Early-Warning with Distributed Acoustic Sensing: Expected Seafloor Strains Induced by Tsunamis. *Pure and Applied Geophysics*, *183*, 2035–2059. doi: 10.1007/s00024-026-03940-1

Behrens, J. (2026). R7—ASCETE Coupled Earthquake-Tsunami Modelling. In M. B. Sørensen et al. (Eds.), *Probabilistic Tsunami Hazard and Risk Analysis: A Cookbook* (pp. 447–452). Springer Nature Switzerland. doi: 10.1007/978-3-031-98115-9_16

Beisel, S., Chubarov, L., Didenkulova, I., Kit, E., Levin, A., Pelinovsky, E., ... Sladkevich, M. (2009). The 1956 Greek tsunami recorded at Yafo, Israel, and its numerical modeling. *Journal of Geophysical Research: Oceans*, *114*(C9), 9002. doi: 10.1029/2008JC005262

Benetatos, C., Kiratzi, A., Papazachos, C., & Karakaisis, G. (2004). Focal mechanisms of shallow and intermediate depth earthquakes along the Hellenic Arc. *Journal of Geodynamics*, *37*(2), 253–296. doi: 10.1016/j.jog.2004.02.002

Beresnev, I. A. (2003). Uncertainties in Finite-Fault Slip Inversions: To What Extent to Believe? (A Critical Review). *Bulletin of the Seismological Society of America*, *93*(6), 2445–2458. doi: 10.1785/0120020225

Berger, M. J., George, D. L., LeVeque, R. J., & Mandli, K. T. (2011). The GeoClaw software for depth-averaged flows with adaptive refinement. *Advances in Water Resources*, *34*(9), 1195–1206. doi: 10.1016/j.advwatres.2011.02.016

Berger, M. J., & LeVeque, R. J. (2024). Implicit Adaptive Mesh Refinement for Dispersive Tsunami Propagation. *SIAM Journal on Scientific Computing*, *46*(4), B554-B578. doi: 10.1137/23M1585210

Beroza, G. C., & Ellsworth, W. L. (1996). Properties of the seismic nucleation phase. *Tectonophysics*, *261*(1-3), 209–227. doi: 10.1016/0040-1951(96)00067-4

Beyreuther, M., Barsch, R., Krischer, L., Megies, T., Behr, Y., & Wassermann, J. (2010). ObsPy: A Python Toolbox for Seismology. *Seismological Research Letters*, *81*(3), 530–533. doi: 10.1785/gssrl.81.3.530

Biemiller, J., Gabriel, A.-A., & Ulrich, T. (2023). Dueling dynamics of low-angle normal fault rupture with splay faulting and off-fault damage. *Nature Communications*, *14*(1), 1–12. doi: 10.1038/s41467-023-37063-1

Bilek, S. L., & Lay, T. (2018). Subduction zone megathrust earthquakes. *Geosphere*, *14*(4), 1468–1500. doi: 10.1130/GES01608.1

Biot, M. A. (1952). The interaction of Rayleigh and Stoneley waves in the ocean bottom. *Bulletin of the Seismological Society of America*, *42*(1), 81–93. doi: 10.1785/BSSA0420010081

Bird, P. (2003). An updated digital model of plate boundaries. *Geochemistry, Geophysics, Geosystems*, *4*(3), 2001GC000252. doi: 10.1029/2001GC000252

Bonilla, L. F., Archuleta, R. J., & Lavallée, D. (2005). Hysteretic and Dilatant Behavior of Cohesionless Soils and Their Effects on Nonlinear Site Response: Field Data Observations and Modeling. *Bulletin of the Seismological Society of America*, *95*(6), 2373–2395. doi: 10.1785/0120040128

Boore, D. M. (2010). Orientation-Independent, Nongeometric-Mean Measures of Seismic Intensity from Two Horizontal Components of Motion. *Bulletin of the Seismological Society of America*, *100*(4), 1830–1835. doi: 10.1785/0120090400

Boore, D. M., Watson-Lamprey, J., & Abrahamson, N. A. (2006). Orientation-Independent Measures of Ground Motion. *Bulletin of the Seismological Society of America*, *96*(4A), 1502–1511. doi: 10.1785/0120050209

Breuer, A., Heinecke, A., & Bader, M. (2016). Petascale Local Time Stepping for the ADER-DG Finite Element Method. In *2016 IEEE International Parallel and Distributed Processing Symposium (IPDPS)* (pp. 854–863). doi: 10.1109/IPDPS.2016.109

Causse, M., Dalguer, L. A., & Mai, P. M. (2014). Variability of dynamic source parameters inferred from kinematic models of past earthquakes. *Geophysical Journal International*, *196*(3), 1754–1769. doi: 10.1093/GJI/GGT478

Cecioni, C., Bellotti, G., Romano, A., Abdolali, A., Sammarco, P., & Franco, L. (2014). Tsunami Early Warning System based on Real-time Measurements of Hydro-acoustic Waves. *Procedia Engineering*, *70*, 311–320. doi: 10.1016/j.proeng.2014.02.035

Cetin, K. O., Mylonakis, G., Sextos, A., Stewart, J. P., & 114 contributors. (2020). *Seismological and Engineering Effects of the M 7.0 Samos Island (Aegean Sea) Earthquake* (Tech. Rep.). Geotechnical Extreme Events Reconnaissance Association: Report GEER-069. doi: 10.18118/G6H088

Cheng, A.-C., Suppasri, A., Heidarzadeh, M., & Mas, E. (2026). Long-duration oscillation of a tsunami in the west Japan region following the 21 December

2010 Mw 7.4 Bonin Outer-rise earthquake. *Ocean Engineering*, *365*, 127407. doi: 10.1016/j.oceaneng.2026.127407

Chourasia, A., Youn, C., Silva, F., Oryan, B., Zhao, C., Yun, J., ... Ben-Zion, Y. (2024). Quakeworx: A New Science Gateway for Earthquake Simulation and Data Analysis. In *SCEC Annual Meeting* (Vol. 2024).

Chousianitis, K., & Konca, A. O. (2021). Rupture Process of the 2020 Mw7.0 Samos Earthquake and its Effect on Surrounding Active Faults. *Geophysical Research Letters*, *48*(14), e2021GL094162. doi: 10.1029/2021GL094162

Clawpack Development Team. (2024). *Clawpack Version 5.11.0.* Zenodo. doi: 10.5281/zenodo.13376470

Cleveland, W. S. (1979). Robust Locally Weighted Regression and Smoothing Scatterplots. *Journal of the American Statistical Association*, *74*(368), 829–836.

Crotwell, H. P., Owens, T. J., & Ritsema, J. (1999). The TauP Toolkit: Flexible Seismic Travel-time and Ray-path Utilities. *Seismological Research Letters*, *70*(2), 154–160. doi: 10.1785/gssrl.70.2.154

Cummins, P. R., Pranantyo, I. R., Pownall, J. M., Griffin, J. D., Meilano, I., & Zhao, S. (2020). Earthquakes and tsunamis caused by low-angle normal faulting in the Banda Sea, Indonesia. *Nature Geoscience*, *13*(4), 312–318. doi: 10.1038/s41561-020-0545-x

Day, S. M. (1998). Efficient simulation of constant Q using coarse-grained memory variables. *Bulletin of the Seismological Society of America*, *88*(4), 1051–1062. doi: 10.1785/BSSA0880041051

Day, S. M., Dalguer, L. A., Lapusta, N., & Liu, Y. (2005). Comparison of finite difference and boundary integral solutions to three-dimensional spontaneous rupture. *Journal of Geophysical Research: Solid Earth*, *110*(B12). doi: 10.1029/2005JB003813

de la Puente, J., Ampuero, J.-P., & Käser, M. (2009). Dynamic rupture modeling on unstructured meshes using a discontinuous Galerkin method. *Journal of Geophysical Research: Solid Earth*, *114*(B10). doi: 10.1029/2008JB006271

Dogan, G. G., Annunziato, A., Papadopoulos, G. A., Guler, H. G., Yalciner, A. C., Cakir, T. E., ... Synolakis, C. (2019). The 20th July 2017 Bodrum–Kos Tsunami Field Survey. *Pure and Applied Geophysics*, *176*(7), 2925–2949. doi: 10.1007/S00024-019-02151-1

Dogan, G. G., Yalciner, A. C., Yuksel, Y., Ulutaş, E., Polat, O., Güler, I., ... Kânoğlu, U. (2021). The 30 October 2020 Aegean Sea Tsunami: Post-Event Field Survey Along Turkish Coast. *Pure and Applied Geophysics*, *178*(3), 785–812. doi: 10.1007/S00024-021-02693-3

Du, Y., & Ma, S. (2025). Wedge Inelasticity and Fully Coupled Models of Dynamic Rupture, Ocean Acoustic Waves, and Tsunami in the Japan Trench: The 1896 Sanriku Earthquake. *Journal of Geophysical Research: Solid Earth*, *130*(10), e2025JB032410. doi: 10.1029/2025JB032410

Dumbser, M., & Käser, M. (2006). An arbitrary high-order discontinuous Galerkin method for elastic waves on unstructured meshes - II. The three-dimensional isotropic case. *Geophysical Journal International*, *167*(1), 319–336. doi: 10.1111/j.1365-246X.2006.03120.x

Dziewonski, A. M., Chou, T. A., & Woodhouse, J. H. (1981). Determination of earthquake source parameters from waveform data for studies of global and regional seismicity. *Journal of Geophysical Research: Solid Earth*, *86*(B4), 2825–2852. doi: 10.1029/JB086IB04P02825

Ekström, G., Nettles, M., & Dziewoński, A. M. (2012). The global CMT project 2004–2010: Centroid-moment tensors for 13,017 earthquakes. *Physics of the Earth and Planetary Interiors*, *200–201*, 1–9. doi: 10.1016/j.pepi.2012.04.002

England, P., Houseman, G., & Nocquet, J. M. (2016). Constraints from GPS measurements on the dynamics of deformation in Anatolia and the Aegean. *Journal of Geophysical Research: Solid Earth*, *121*(12), 8888–8916. doi: 10.1002/

2016JB013382

England, P., Howell, A., Jackson, J., & Synolakis, C. (2015). Palaeotsunamis and tsunami hazards in the Eastern Mediterranean. *Philosophical Transactions of the Royal Society A: Mathematical, Physical and Engineering Sciences*, *373*(2053), 20140374. doi: 10.1098/rsta.2014.0374

Felix, R., Hubbard, J., Wilson, K., & Switzer, A. (2024). Heatmap analysis of modeled coastal tsunamis using different bathymetry data resolutions. *Geoscience Letters*, *11*(1), 47. doi: 10.1186/s40562-024-00362-6

Flanders Marine Institute (VLIZ), Intergovernmental Oceanographic Commission (IOC). (2026). *Sea level station monitoring facility.* doi: 10.14284/482

Fountoulakis, I., Evangelidis, C. P., & Ktenidou, O.-J. (2023). Coseismic and Postseismic Imaging of a Composite Fault System: The Samos 2020 Mw 7.0 Sequence. *Bulletin of the Seismological Society of America*, *113*(3), 997–1012. doi: 10.1785/0120220207

Gabriel, A.-A., Kurapati, V., Niu, Z., Schliwa, N., Schneller, D., Ulrich, T., ... Bader, M. (2025). *SeisSol.* Zenodo. doi: 10.5281/zenodo.4672483

Galis, M., Pelties, C., Kristek, J., Moczo, P., Ampuero, J. P., & Mai, P. M. (2015). On the initiation of sustained slip-weakening ruptures by localized stresses. *Geophysical Journal International*, *200*(2), 890–909. doi: 10.1093/GJI/GGU436

Gallovič, F., Imperatori, W., & Mai, P. M. (2015). Effects of three-dimensional crustal structure and smoothing constraint on earthquake slip inversions: Case study of the Mw6.3 2009 L'Aquila earthquake. *Journal of Geophysical Research: Solid Earth*, *120*(1), 428–449. doi: 10.1002/2014JB011650

Ganas, A., Elias, P., Briole, P., Valkaniotis, S., Escartin, J., Tsironi, V., ... Kosma, C. (2021). Co-seismic and post-seismic deformation, field observations and fault model of the 30 October 2020 Mw = 7.0 Samos earthquake, Aegean Sea. *Acta Geophysica*, *69*(3), 999–1024. doi: 10.1007/S11600-021-00599-1

Ganas, A., Elias, P., Kapetanidis, V., Valkaniotis, S., Briole, P., Kassaras, I., ... Moshou, A. (2019). The July 20, 2017 M6.6 Kos Earthquake: Seismic and Geodetic Evidence for an Active North-Dipping Normal Fault at the Western End of the Gulf of Gökova (SE Aegean Sea). *Pure and Applied Geophysics*, *176*(10), 4177–4211. doi: 10.1007/S00024-019-02154-Y

GEBCO Bathymetric Compilation Group. (2022). *GEBCO 2022 Grid.* doi: 10.5285/e0f0bb80-ab44-2739-e053-6c86abc0289c

George, D. L. (2008). Augmented Riemann solvers for the shallow water equations over variable topography with steady states and inundation. *Journal of Computational Physics*, *227*(6), 3089–3113. doi: 10.1016/j.jcp.2007.10.027

Geuzaine, C., & Remacle, J.-F. (2009). Gmsh: A 3-D finite element mesh generator with built-in pre- and post-processing facilities. *International Journal for Numerical Methods in Engineering*, *79*(11), 1309–1331. doi: 10.1002/nme.2579

Gibbons, S. J., Lorito, S., de la Asunción, M., Volpe, M., Selva, J., Macías, J., ... Løvholt, F. (2022). The Sensitivity of Tsunami Impact to Earthquake Source Parameters and Manning Friction in High-Resolution Inundation Simulations. *Frontiers in Earth Science*, *9*, 1412. doi: 10.3389/feart.2021.757618

Glimsdal, S., Pedersen, G. K., Harbitz, C. B., & Løvholt, F. (2013). Dispersion of tsunamis: Does it really matter? *Natural Hazards and Earth System Sciences*, *13*(6), 1507–1526. doi: 10.5194/NHESS-13-1507-2013

Gonzalez, F. I., LeVeque, R. J., Chamberlain, P., Hirai, B., Varkovitzky, J., & George, D. L. (2011). *Validation of the GeoClaw model* (Tech. Rep.). NTHMP MMS Tsunami Inundation Model Validation Workshop.

Gonzalez, F. I., Milburn, H. M., Bernard, E. N., & Newman, J. C. (1998). Deep-ocean assessment and reporting of tsunamis (DART): Brief overview and status report. In *Proceedings of the international workshop on tsunami disaster mitigation.* Tokyo, Japan.

Gräff, D., Lipovsky, B. P., Vieli, A., Dachauer, A., Jackson, R., Farinotti, D., ... Williams, E. F. (2025). Calving-driven fjord dynamics resolved by seafloor fibre sensing. *Nature*, *644*(8076), 404–412. doi: 10.1038/s41586-025-09347-7

Guatteri, M., & Spudich, P. (1998). Coseismic temporal changes of slip direction: The effect of absolute stress on dynamic rupture. *Bulletin of the Seismological Society of America*, *88*(3), 777–789. doi: 10.1785/BSSA0880030777

Harris, C. R., Millman, K. J., van der Walt, S. J., Gommers, R., Virtanen, P., Cournapeau, D., ... Oliphant, T. E. (2020). Array programming with NumPy. *Nature*, *585*(7825), 357–362. doi: 10.1038/s41586-020-2649-2

Harris, R. A., Aagaard, B., Barall, M., Ma, S., Roten, D., Olsen, K., ... Dalguer, L. (2018). A suite of exercises for verifying dynamic earthquake rupture codes. *Seismological Research Letters*, *89*(3), 1146–1162. doi: 10.1785/0220170222

Hartzell, S., Meremonte, M., Ramírez-Guzmán, L., & McNamara, D. (2013). Ground Motion in the Presence of Complex Topography: Earthquake and Ambient Noise Sources. *Bulletin of the Seismological Society of America*, *104*(1), 451–466. doi: 10.1785/0120130088

Haskell, N. A. (1964). Total energy and energy spectral density of elastic wave radiation from propagating faults. *Bulletin of the Seismological Society of America*, *54*(6A), 1811–1841. doi: 10.1785/BSSA05406A1811

Heidarzadeh, M., Pranantyo, I. R., Okuwaki, R., Dogan, G. G., & Yalciner, A. C. (2021). Long Tsunami Oscillations Following the 30 October 2020 Mw 7.0 Aegean Sea Earthquake: Observations and Modelling. *Pure and Applied Geophysics*, *178*(5), 1531–1548. doi: 10.1007/S00024-021-02761-8

Henneking, S., Kutschera, F., Venkat, S., Gabriel, A.-A., & Ghattas, O. (2026). *Real-time probabilistic tsunami forecasting in Cascadia from sparse offshore pressure observations* (No. arXiv:2603.14966). arXiv. doi: 10.48550/arXiv.2603.14966

Herman, M. W., Hayes, G. P., Smoczyk, G. M., Turner, R., Turner, B., Jenkins, J., ... Villaseñor, A. (2015). *Seismicity of the Earth 1900-2013, Mediterranean Sea and vicinity* (Tech. Rep. Nos. Open-File Report 2010–1083-Q, scale 1:10,000,000). U.S. Geological Survey. doi: 10.3133/ofr20101083Q

Hsu, Y.-J., Simons, M., Williams, C., & Casarotti, E. (2011). Three-dimensional FEM derived elastic Green's functions for the coseismic deformation of the 2005 Mw 8.7 Nias-Simeulue, Sumatra earthquake. *Geochemistry, Geophysics, Geosystems*, *12*(7), Q07013. doi: 10.1029/2011GC003553

Hu, G., Feng, W., Wang, Y., Li, L., He, X., Karakaş, Ç., & Tian, Y. (2022). Source Characteristics and Exacerbated Tsunami Hazard of the 2020 Mw 6.9 Samos Earthquake in Eastern Aegean Sea. *Journal of Geophysical Research: Solid Earth*, *127*(5), e2022JB023961. doi: 10.1029/2022JB023961

Hunter, J. D. (2007). Matplotlib: A 2D Graphics Environment. *Computing in Science & Engineering*, *9*(3), 90–95. doi: 10.1109/MCSE.2007.55

Ida, Y. (1972). Cohesive force across the tip of a longitudinal-shear crack and Griffith's specific surface energy. *Journal of Geophysical Research*, *77*(20), 3796–3805. doi: 10.1029/JB077I020P03796

Jolivet, R. (2024). *Jolivetr/okada4py: First release.* Zenodo. doi: 10.5281/zenodo.14170827

Kadri, U., Abdolali, A., & Filimonov, M. (2025). GREAT v1.0: Global Real-time Early Assessment of Tsunamis. *Geoscientific Model Development*, *18*(11), 3487–3507. doi: 10.5194/gmd-18-3487-2025

Kajiura, K. (1963). The Leading Wave of a Tsunami. *Bulletin Earthquake Research Institute*, *41*(3), 535–571. doi: 10.15083/0000033711

Kalligeris, N., Skanavis, V., Charalampakis, M., Melis, N. S., Voukouvalas, E., Annunziato, A., & Synolakis, C. E. (2022). Field survey of the 30 October 2020 Samos (Aegean Sea) tsunami in the Greek islands. *Bulletin of Earthquake Engineering*, *20*(14), 7873–7905. doi: 10.1007/s10518-021-01250-6

Kanamori, H. (1971). Seismological evidence for a lithospheric normal faulting — the Sanriku earthquake of 1933. *Physics of the Earth and Planetary Interiors*, *4*(4), 289–300. doi: 10.1016/0031-9201(71)90013-6

Karakostas, V., Tan, O., Kostoglou, A., Papadimitriou, E., & Bonatis, P. (2021). Seismotectonic implications of the 2020 Samos, Greece, Mw 7.0 mainshock based on high-resolution aftershock relocation and source slip model. *Acta Geophysica*, *69*(3), 979–996. doi: 10.1007/S11600-021-00580-Y

Karasözen, E., Nissen, E., Büyükakpinar, P., Cambaz, M. D., Kahraman, M., Ertan, E. K., ... Özacar, A. A. (2018). The 2017 July 20 Mw 6.6 Bodrum–Kos earthquake illuminates active faulting in the Gulf of Gökova, SW Turkey. *Geophysical Journal International*, *214*(1), 185–199. doi: 10.1093/GJI/GGY114

Käser, M., & Dumbser, M. (2006). An arbitrary high-order discontinuous Galerkin method for elastic waves on unstructured meshes - I. The two-dimensional isotropic case with external source terms. *Geophysical Journal International*, *166*(2), 855–877. doi: 10.1111/j.1365-246X.2006.03051.x

Käser, M., Hermann, V., & de la Puente, J. (2008). Quantitative accuracy analysis of the discontinuous Galerkin method for seismic wave propagation. *Geophysical Journal International*, *173*(3), 990–999. doi: 10.1111/j.1365-246X.2008.03781.x

Kearse, J., & Kaneko, Y. (2020). On-Fault Geological Fingerprint of Earthquake Rupture Direction. *Journal of Geophysical Research: Solid Earth*, *125*(9), e2020JB019863. doi: 10.1029/2020JB019863

Kearse, J., Kaneko, Y., Little, T., & Van Dissen, R. (2019). Curved slickenlines preserve direction of rupture propagation. *Geology*, *47*(9), 838–842. doi: 10.1130/G46563.1

Kiratzi, A., Papazachos, C., Özacar, A., Pinar, A., Kkallas, C., & Sopaci, E. (2022). Characteristics of the 2020 Samos earthquake (Aegean Sea) using seismic data. *Bulletin of Earthquake Engineering*, *20*, 7713–7735. doi: 10.1007/s10518-021-01239-1

Konstantinou, K. I., Mouslopoulou, V., Liang, W.-T., Heidbach, O., Oncken, O., & Suppe, J. (2017). Present-day crustal stress field in Greece inferred from regional-scale damped inversion of earthquake focal mechanisms. *Journal of Geophysical Research: Solid Earth*, *122*(1), 506–523. doi: 10.1002/2016JB013272

Krenz, L., Uphoff, C., Ulrich, T., Gabriel, A.-A., Abrahams, L. S., Dunham, E. M., & Bader, M. (2021). 3D acoustic-elastic coupling with gravity: The dynamics of the 2018 Palu, Sulawesi earthquake and tsunami. In *Proceedings of the International Conference for High Performance Computing, Networking, Storage and Analysis* (pp. 1–14). Association for Computing Machinery. doi: 10.1145/3458817.3476173

Krischer, L., Megies, T., Barsch, R., Beyreuther, M., Lecocq, T., Caudron, C., & Wassermann, J. (2015). ObsPy: A bridge for seismology into the scientific Python ecosystem. *Computational Science & Discovery*, *8*(1), 014003. doi: 10.1088/1749-4699/8/1/014003

Kristek, J., & Moczo, P. (2003). Seismic-Wave Propagation in Viscoelastic Media with Material Discontinuities: A 3D Fourth-Order Staggered-Grid Finite-Difference Modeling. *Bulletin of the Seismological Society of America*, *93*(5), 2273–2280. doi: 10.1785/0120030023

Kundu, P. K., Cohen, I. M., & Dowling, D. R. (2016). Chapter 8 - Gravity Waves. In P. K. Kundu, I. M. Cohen, & D. R. Dowling (Eds.), *Fluid Mechanics (Sixth Edition)* (pp. 349–407). Academic Press. doi: 10.1016/B978-0-12-405935-1.00008-3

Kutschera, F., & Gabriel, A.-A. (2026). *Supplementary material for "Source Representation and Earthquake-Ocean Coupling in Tsunami Generation by the 2020 Samos Normal-Faulting Earthquake".* Zenodo. doi: 10.5281/zenodo.18637304

Kutschera, F., Gabriel, A.-A., Dunham, E. M., Harris, R., Barall, M., Bachelot, L., ... Zhang, W. (2025). The CRESCENT/SCEC/USGS Tsunami Benchmarks: 3D Fully Coupled Earthquake Dynamic Rupture and Tsunami Simulations with Varying Bathymetric Complexity. In *Abstract (T43E-0182) presented at AGU25, 15-19 Dec.* AGU Annual Meeting 2025.

Kutschera, F., Gabriel, A.-A., Wirp, S. A., Li, B., Ulrich, T., Abril, C., & Halldórsson, B. (2024). Linked and fully coupled 3D earthquake dynamic rupture and tsunami modeling for the Húsavík–Flatey Fault Zone in North Iceland. *Solid Earth*, *15*(2), 251–280. doi: 10.5194/se-15-251-2024

Kutschera, F., Jia, Z., Oryan, B., Wong, J. W. C., Fan, W., & Gabriel, A.-A. (2024). The Multi-Segment Complexity of the 2024 Mw 7.5 Noto Peninsula Earthquake Governs Tsunami Generation. *Geophysical Research Letters*, *51*(21), e2024GL109790. doi: 10.1029/2024GL109790

Langer, L., Gharti, H. N., & Tromp, J. (2019). Impact of topography and three-dimensional heterogeneity on coseismic deformation. *Geophysical Journal International*, *217*(2), 866–878. doi: 10.1093/gji/ggz060

Latour, S., Lebihain, M., Bhat, H. S., Twardzik, C., Bletery, Q., Hudnut, K. W., & Passelègue, F. (2025). Direct estimation of earthquake source properties from a single CCTV camera. *Science*, *390*(6772), 463–467. doi: 10.1126/science.adz1705

Lay, T., Ammon, C. J., Kanamori, H., Kim, M. J., & Xue, L. (2011). Outer trench-slope faulting and the 2011 Mw 9.0 off the Pacific coast of Tohoku Earthquake. *Earth, Planets and Space*, *63*(7), 713–718. doi: 10.5047/eps.2011.05.006

Leclerc, F., Palagonia, S., Feuillet, N., Nomikou, P., Lampridou, D., Barrière, P., ... Escartin, J. (2024). Large seafloor rupture caused by the 1956 Amorgos tsunamigenic earthquake, Greece. *Communications Earth & Environment*, *5*(1), 1–8. doi: 10.1038/s43247-024-01839-0

Lee, S.-J., Komatitsch, D., Huang, B.-S., & Tromp, J. (2009). Effects of Topography on Seismic-Wave Propagation: An Example from Northern Taiwan. *Bulletin of the Seismological Society of America*, *99*(1), 314–325. doi: 10.1785/0120080020

Lentas, K., Gkarlaouni, C. G., Kalligeris, N., & Melis, N. S. (2021). The 30 October 2020, MW = 7.0, Samos earthquake: Aftershock relocation, slip model, Coulomb stress evolution and estimation of shaking. *Bulletin of Earthquake Engineering*, *20*(2), 819–851. doi: 10.1007/S10518-021-01260-4

Le Pichon, X., & Kreemer, C. (2010). The Miocene-to-Present Kinematic Evolution of the Eastern Mediterranean and Middle East and Its Implications for Dynamics. *Annual Review of Earth and Planetary Sciences*, *38*, 323–351. doi: 10.1146/ANNUREV-EARTH-040809-152419

LeVeque, R. J., & George, D. L. (2008). High-Resolution Finite Volume Methods for the Shallow Water Equations With Bathymetry and Dry States. In *Advances in Coastal and Ocean Engineering* (Vol. 10, pp. 43–73). World Scientific. doi: 10.1142/9789812790910_0002

LeVeque, R. J., George, D. L., & Berger, M. J. (2011). Tsunami modelling with adaptively refined finite volume methods. *Acta Numerica*, *20*, 211–289. doi: 10.1017/S0962492911000043

Levin, B. W., & Nosov, M. A. (2015). *Physics of Tsunamis* (2nd ed.). Springer International Publishing. doi: 10.1007/978-3-319-24037-4

Li, B., Gabriel, A.-A., Ulrich, T., Abril, C., & Halldorsson, B. (2023). Dynamic Rupture Models, Fault Interaction and Ground Motion Simulations for the Segmented Húsavík-Flatey Fault Zone, Northern Iceland. *Journal of Geophysical Research: Solid Earth*, *128*(6), e2022JB025886. doi: 10.1029/2022JB025886

Lorito, S., Tiberti, M. M., Basili, R., Piatanesi, A., & Valensise, G. (2008). Earthquake-generated tsunamis in the Mediterranean Sea: Scenarios of potential threats to Southern Italy. *Journal of Geophysical Research: Solid*

Earth, *113*(B1), 2007JB004943. doi: 10.1029/2007JB004943

Lotto, G. C., & Dunham, E. M. (2015). High-order finite difference modeling of tsunami generation in a compressible ocean from offshore earthquakes. *Computational Geosciences*, *19*(2), 327–340. doi: 10.1007/S10596-015-9472-0

Lotto, G. C., Jeppson, T. N., & Dunham, E. M. (2018). Fully Coupled Simulations of Megathrust Earthquakes and Tsunamis in the Japan Trench, Nankai Trough, and Cascadia Subduction Zone. *Pure and Applied Geophysics*, *176*(9), 4009–4041. doi: 10.1007/S00024-018-1990-Y

Løvholt, F., Murphy, S., Lorito, S., Romano, F., Harbitz, C. B., Selva, J., ... Denamiel, C. (2026). Source Modelling. In M. B. Sørensen et al. (Eds.), *Probabilistic Tsunami Hazard and Risk Analysis: A Cookbook* (pp. 157–222). Springer Nature Switzerland. doi: 10.1007/978-3-031-98115-9_4

Lynnes, C. S., & Lay, T. (1988). Source Process of the Great 1977 Sumba Earthquake. *Journal of Geophysical Research: Solid Earth*, *93*(B11), 13407–13420. doi: 10.1029/JB093iB11p13407

Ma, S. (2023). Wedge plasticity and a minimalist dynamic rupture model for the 2011 MW 9.1 Tohoku-Oki earthquake and tsunami. *Tectonophysics*, *869*, 230146. doi: 10.1016/j.tecto.2023.230146

Ma, S., Custódio, S., Archuleta, R. J., & Liu, P. (2008). Dynamic modeling of the 2004 Mw 6.0 Parkfield, California, earthquake. *Journal of Geophysical Research: Solid Earth*, *113*(B2), 2301. doi: 10.1029/2007JB005216

Madden, E. H., Bader, M., Behrens, J., Van Dinther, Y., Gabriel, A. A., Rannabauer, L., ... Van Zelst, I. (2021). Linked 3-D modelling of megathrust earthquake-tsunami events: From subduction to tsunami run up. *Geophysical Journal International*, *224*(1), 487–516. doi: 10.1093/GJI/GGAA484

Maeda, T., & Furumura, T. (2013). FDM Simulation of Seismic Waves, Ocean Acoustic Waves, and Tsunamis Based on Tsunami-Coupled Equations of Motion. *Pure and Applied Geophysics*, *170*(1), 109–127. doi: 10.1007/s00024-011-0430-z

Maeda, T., Furumura, T., Noguchi, S., Takemura, S., Sakai, S., Shinohara, M., ... Lee, S. J. (2013). Seismic- and Tsunami-Wave Propagation of the 2011 Off the Pacific Coast of Tohoku Earthquake as Inferred from the Tsunami-Coupled Finite-Difference Simulation. *Bulletin of the Seismological Society of America*, *103*(2B), 1456–1472. doi: 10.1785/0120120118

Mai, P. M., Schorlemmer, D., Page, M., Ampuero, J.-P., Asano, K., Causse, M., ... Zielke, O. (2016). The Earthquake-Source Inversion Validation (SIV) Project. *Seismological Research Letters*, *87*(3), 690–708. doi: 10.1785/0220150231

Mai, P. M., Shearer, P., Ampuero, J.-P., & Lay, T. (2016). Standards for Documenting Finite-Fault Earthquake Rupture Models. *Seismological Research Letters*, *87*(3), 712–718. doi: 10.1785/0220150204

Mai, P. M., & Thingbaijam, K. K. S. (2014). SRCMOD: An Online Database of Finite-Fault Rupture Models. *Seismological Research Letters*, *85*(6), 1348–1357. doi: 10.1785/0220140077

Mandli, K. T., Ahmadia, A. J., Berger, M., Calhoun, D., George, D. L., Hadjimichael, Y., ... LeVeque, R. J. (2016). Clawpack: Building an open source ecosystem for solving hyperbolic PDEs. *PeerJ Computer Science*, *2*(8), e68. doi: 10.7717/peerj-cs.68

Margolis, A., Oglesby, D., Wu, B., Kyriakopoulos, C., & Ryan, K. (2026). Quantifying the Effects of the Value of Absolute Friction and Geometrical Symmetry on Dip-Slip Faults. *Bulletin of the Seismological Society of America*, 1–11. doi: 10.1785/0120250289

Mavroulis, S., Ilgac, M., Tunçağ, M., Lekkas, E., Püskülcü, S., Kourou, A., ... Karveleas, N. (2022). Emergency response, intervention, and societal recovery in Greece and Turkey after the 30th October 2020, MW = 7.0, Samos (Aegean Sea) earthquake. *Bulletin of Earthquake Engineering*, *20*(14), 7933–7955. doi:

10.1007/s10518-022-01317-y

McKinney, W. (2010). Data Structures for Statistical Computing in Python. In S. van der Walt & J. Millman (Eds.), *Proceedings of the 9th Python in Science Conference* (pp. 56–61). doi: 10.25080/Majora-92bf1922-00a

Meegan, G. D., Hamilton, M. F., Il'inskii, Yu. A., & Zabolotskaya, E. A. (1999). Nonlinear Stoneley and Scholte waves. *The Journal of the Acoustical Society of America*, *106*(4), 1712–1723. doi: 10.1121/1.427920

Melgar, D. (2026). Consideration of rupture kinematics increases tsunami amplitudes in far-field hazards assessments. *Seismica*, *2*(4). doi: 10.26443/seismica.v2i4.1668

Melis, N. S., Okal, E. A., Synolakis, C. E., Kalogeras, I. S., & Kânoğlu, U. (2020). The Chios, Greece Earthquake of 23 July 1949: Seismological Reassessment and Tsunami Investigations. *Pure and Applied Geophysics*, *177*(3), 1295–1313. doi: 10.1007/S00024-019-02410-1

Meng, J., Sinoplu, O., Zhou, Z., Tokay, B., Kusky, T., Bozkurt, E., & Wang, L. (2021). Greece and Turkey Shaken by African tectonic retreat. *Scientific Reports*, *11*(1), 1–10. doi: 10.1038/s41598-021-86063-y

Mosconi, F., Tinti, E., Casarotti, E., Gabriel, A.-A., Rinaldi, A. P., Dal Zilio, L., & Cocco, M. (2025). Modeling the 3D Dynamic Rupture of Microearthquakes Induced by Fluid Injection. *Journal of Geophysical Research: Solid Earth*, *130*(3), e2024JB029621. doi: 10.1029/2024JB029621

Mouslopoulou, V., Begg, J. G., Polonia, A., Nicol, A., Reston, T. J., Cesca, S., ... Gasperini, L. (2025). Hellenic Subduction System and Upper-Plate Structures Revealed by Deep High-Resolution Seismic-Reflection Profiles and Seafloor Bathymetry. *Tectonics*, *44*(9), e2025TC008943. doi: 10.1029/2025TC008943

Mouslopoulou, V., Nicol, A., Begg, J., Oncken, O., & Moreno, M. (2015). Clusters of megaearthquakes on upper plate faults control the Eastern Mediterranean hazard. *Geophysical Research Letters*, *42*(23), 10,282–10,289. doi: 10.1002/2015GL066371

Mungov, G., Eblé, M., & Bouchard, R. (2013). DART® Tsunameter Retrospective and Real-Time Data: A Reflection on 10 Years of Processing in Support of Tsunami Research and Operations. *Pure and Applied Geophysics*, *170*(9), 1369–1384. doi: 10.1007/s00024-012-0477-5

Nielsen, S., & Madariaga, R. (2003). On the Self-Healing Fracture Mode. *Bulletin of the Seismological Society of America*, *93*(6), 2375–2388. doi: 10.1785/0120020090

Niu, Z., Gabriel, A.-A., Wolf, S., Ulrich, T., Lyakhovsky, V., & Igel, H. (2025). A Discontinuous Galerkin Method for Simulating 3D Seismic Wave Propagation in Nonlinear Rock Models: Verification and Application to the Mw 7.8 2015 Gorkha, Nepal Earthquake. *Journal of Geophysical Research: Solid Earth*, *130*(7), e2025JB031378. doi: 10.1029/2025JB031378

Noguchi, S., Maeda, T., & Furumura, T. (2016). Ocean-influenced Rayleigh waves from outer-rise earthquakes and their effects on durations of long-period ground motion. *Geophysical Journal International*, *205*(2), 1099–1107. doi: 10.1093/gji/ggw074

Novotný, O., Zahradník, J., & Tselentis, G.-A. (2001). Northwestern Turkey Earthquakes and the Crustal Structure Inferred from Surface Waves Observed in Western Greece. *Bulletin of the Seismological Society of America*, *91*(4), 875–879. doi: 10.1785/0120000116

Obana, K., Nakamura, Y., Fujie, G., Kodaira, S., Kaiho, Y., Yamamoto, Y., & Miura, S. (2018). Seismicity in the source areas of the 1896 and 1933 Sanriku earthquakes and implications for large near-trench earthquake faults. *Geophysical Journal International*, *212*(3), 2061–2072. doi: 10.1093/gji/ggx532

Oeser, J., Bunge, H. P., & Mohr, M. (2006). Cluster Design in the Earth Sciences Tethys. *Lecture Notes in Computer Science (including subseries Lecture Notes*

in Artificial Intelligence and Lecture Notes in Bioinformatics), *4208 LNCS*, 31–40. doi: 10.1007/11847366_4

Oglesby, D. D., Archuleta, R. J., & Nielsen, S. B. (1998). Earthquakes on Dipping Faults: The Effects of Broken Symmetry. *Science*, *280*(5366), 1055–1059. doi: 10.1126/science.280.5366.1055

Oglesby, D. D., Archuleta, R. J., & Nielsen, S. B. (2000). The Three-Dimensional Dynamics of Dipping Faults. *Bulletin of the Seismological Society of America*, *90*(3), 616–628. doi: 10.1785/0119990113

Ohta, Y., Kobayashi, T., Tsushima, H., Miura, S., Hino, R., Takasu, T., ... Umino, N. (2012). Quasi real-time fault model estimation for near-field tsunami forecasting based on RTK-GPS analysis: Application to the 2011 Tohoku-Oki earthquake (Mw 9.0). *Journal of Geophysical Research: Solid Earth*, *117*(B2), 2011JB008750. doi: 10.1029/2011JB008750

Okada, Y. (1985). Surface deformation due to shear and tensile faults in a half-space. *Bulletin of the Seismological Society of America*, *75*(4), 1135–1154. doi: 10.1785/BSSA0750041135

Okada, Y. (1992). Internal deformation due to shear and tensile faults in a half-space. *Bulletin of the Seismological Society of America*, *82*(2), 1018–1040. doi: 10.1785/BSSA0820021018

Okal, E. A., Synolakis, C. E., Uslu, B., Kalligeris, N., & Voukouvalas, E. (2009). The 1956 earthquake and tsunami in Amorgos, Greece. *Geophysical Journal International*, *178*(3), 1533–1554. doi: 10.1111/j.1365-246X.2009.04237.x

Papadopoulos, G. A., & Pavlides, S. B. (1992). The large 1956 earthquake in the South Aegean: Macroseismic field configuration, faulting, and neotectonics of Amorgos Island. *Earth and Planetary Science Letters*, *113*(3), 383–396. doi: 10.1016/0012-821X(92)90140-Q

Pedregosa, F., Varoquaux, G., Gramfort, A., Michel, V., Thirion, B., Grisel, O., ... Duchesnay, E. (2011). Scikit-learn: Machine learning in Python. *Journal of Machine Learning Research*, *12*, 2825–2830.

Pelties, C., de la Puente, J., Ampuero, J.-P., Brietzke, G. B., & Käser, M. (2012). Three-dimensional dynamic rupture simulation with a high-order discontinuous Galerkin method on unstructured tetrahedral meshes. *Journal of Geophysical Research: Solid Earth*, *117*(B2). doi: 10.1029/2011JB008857

Pelties, C., Gabriel, A.-A., & Ampuero, J.-P. (2014). Verification of an ADER-DG method for complex dynamic rupture problems. *Geoscientific Model Development*, *7*(3), 847–866. doi: 10.5194/gmd-7-847-2014

Philippon, M., Roger, J., Lebrun, J.-F., Thinon, I., Foix, O., Mazzotti, S., ... Cornée, J.-J. (2024). Forearc crustal faults as tsunami sources in the upper plate of the Lesser Antilles subduction zone: The case study of the Morne Piton fault system. *Natural Hazards and Earth System Sciences*, *24*(9), 3129–3154. doi: 10.5194/nhess-24-3129-2024

Plicka, V., Gallovič, F., Zahradník, J., Serpetsidaki, A., Sokos, E., Vavlas, N., & Kiratzi, A. (2022). The 2020 Samos Mw7 earthquake: Source model depicting complexity and rupture directivity. *Tectonophysics*, *843*, 229591. doi: 10.1016/j.tecto.2022.229591

Pulido, N., & Dalguer, L. A. (2009). Estimation of the High-Frequency Radiation of the 2000 Tottori (Japan) Earthquake Based on a Dynamic Model of Fault Rupture: Application to the Strong Ground Motion Simulation. *Bulletin of the Seismological Society of America*, *99*(4), 2305–2322. doi: 10.1785/0120080165

Ramos, M. D., Thakur, P., Huang, Y., Harris, R. A., & Ryan, K. J. (2022). Working with Dynamic Earthquake Rupture Models: A Practical Guide. *Seismological Research Letters*, *93*(4), 2096–2110. doi: 10.1785/0220220022

Rauch, D. (1980). *Seismic Interface Waves in Coastal Waters: A Review* (Tech. Rep. No. SACLANTCEN Report SR-42). SACLANT ASW Research Centre.

Rayleigh, L. (1885). On Waves Propagated along the Plane Surface of an Elastic

Solid. *Proceedings of the London Mathematical Society*, *s1-17*(1), 4–11. doi: 10.1112/plms/s1-17.1.4

Rea, R., Scala, A., Bernardi, F., Elia, L., Lorito, S., Colombelli, S., ... Zollo, A. (2025). Feasibility study of an integrated earthquake and tsunami early warning system. *Scientific Reports*, *15*(1), 43124. doi: 10.1038/s41598-025-25832-5

Reilinger, R., McClusky, S., Paradissis, D., Ergintav, S., & Vernant, P. (2010). Geodetic constraints on the tectonic evolution of the Aegean region and strain accumulation along the Hellenic subduction zone. *Tectonophysics*, *488*(1-4), 22–30. doi: 10.1016/j.tecto.2009.05.027

Rekoske, J., Kutschera, F., Yun, J., Oryan, B., Gabriel, A., May, D., ... Ben-Zion, Y. (2026). Expanding Earthquake Science Education With Quakeworx Interactive Web-based Tools. In *Presented at the 2026 SSA Annual Meeting, Pasadena, CA, 14–18 April.* Seismological Society of America.

Ren, C., Yue, H., Cao, B., Zhu, Y., Wang, T., An, C., ... Li, Z. (2022). Rupture process of the 2020 Mw = 6.9 Samos, Greece earthquake on a segmented fault system constrained from seismic, geodetic, and tsunami observations. *Tectonophysics*, *839*, 229497. doi: 10.1016/J.TECTO.2022.229497

Ren, Z., Liu, H., Zhao, X., Wang, B., & An, C. (2019). Effect of kinematic fault rupture process on tsunami propagation. *Ocean Engineering*, *181*, 43–58. doi: 10.1016/j.oceaneng.2019.03.045

Rettenberger, S., Meister, O., Bader, M., & Gabriel, A.-A. (2016). ASAGI: A Parallel Server for Adaptive Geoinformation. In *Proceedings of the Exascale Applications and Software Conference 2016* (pp. 1–9). Association for Computing Machinery. doi: 10.1145/2938615.2938618

Rice, J. R. (1992). Fault Stress States, Pore Pressure Distributions, and the Weakness of the San Andreas Fault. *International Geophysics*, *51*, 475–503. doi: 10.1016/S0074-6142(08)62835-1

Roger, J. H. M., Faugère, Y., Hébert, H., Delepoulle, A., & Dibarboure, G. (2026). First mapping of a tsunami wavefield by SWOT satellite: Observation data and preliminary numerical simulation of the 19 May 2023 tsunami near the Loyalty Islands. *Natural Hazards and Earth System Sciences*, *26*(2), 943–954. doi: 10.5194/nhess-26-943-2026

Roten, D., Olsen, K. B., Day, S. M., Cui, Y., & Fäh, D. (2014). Expected seismic shaking in Los Angeles reduced by San Andreas fault zone plasticity. *Geophysical Research Letters*, *41*(8), 2769–2777. doi: 10.1002/2014GL059411

Royden, L. H., & Papanikolaou, D. J. (2011). Slab segmentation and late Cenozoic disruption of the Hellenic arc. *Geochemistry, Geophysics, Geosystems*, *12*(3). doi: 10.1029/2010GC003280

Sachpazi, M., Laigle, M., Charalampakis, M., Diaz, J., Kissling, E., Gesret, A., ... Hirn, A. (2016). Segmented Hellenic slab rollback driving Aegean deformation and seismicity. *Geophysical Research Letters*, *43*(2), 651–658. doi: 10.1002/2015GL066818

Saito, T. (2019). *Tsunami Generation and Propagation.* Springer Japan. doi: 10.1007/978-4-431-56850-6

Saito, T., Baba, T., Inazu, D., Takemura, S., & Fukuyama, E. (2019). Synthesizing sea surface height change including seismic waves and tsunami using a dynamic rupture scenario of anticipated Nankai trough earthquakes. *Tectonophysics*, *769*, 228166. doi: 10.1016/j.tecto.2019.228166

Saito, T., & Furumura, T. (2009). Three-dimensional tsunami generation simulation due to sea-bottom deformation and its interpretation based on the linear theory. *Geophysical Journal International*, *178*(2), 877–888. doi: 10.1111/j.1365-246X.2009.04206.x

Saito, T., & Tsushima, H. (2016). Synthesizing ocean bottom pressure records including seismic wave and tsunami contributions: Toward realistic tests of monitoring systems. *Journal of Geophysical Research: Solid Earth*, *121*(11),

8175–8195. doi: 10.1002/2016JB013195

Satake, K. (2014). Advances in earthquake and tsunami sciences and disaster risk reduction since the 2004 Indian ocean tsunami. *Geoscience Letters*, *1*(1), 15. doi: 10.1186/s40562-014-0015-7

Schmidt, D., Wilcock, W., LeVeque, R., Gonzalez, F., Cram, G., Manalang, D., ... Bodin, P. (2019). Earthquake and Tsunami Early Warning on the Cascadia Subduction Zone: A Feasibility Study for an Offshore Geophysical Monitoring Network. In *Seattle: University of Washington* (p. 81 pp.).

Scholte, J. G. (1947). The Range of Existence of Rayleigh and Stoneley Waves. *Geophysical Supplements to the Monthly Notices of the Royal Astronomical Society*, *5*(5), 120–126. doi: 10.1111/j.1365-246X.1947.tb00347.x

Schwarze, H., Madariaga, R., & Ruiz, S. (2026). P-Wave Reverberations in the Water Column of the Chilean Subduction Trench. *Geophysical Research Letters*, *53*(3), e2025GL117113. doi: 10.1029/2025GL117113

Seabold, S., & Perktold, J. (2010). Statsmodels: Econometric and Statistical Modeling with Python. In *Python in Science Conference* (pp. 92–96). doi: 10.25080/Majora-92bf1922-011

Sementsov, K. A., Baba, T., Kolesov, S. V., Tanioka, Y., & Nosov, M. A. (2025). The effect of earthquake fault rupture kinematics on tsunami generation: A numerical study of real events. *Geophysical Journal International*, *240*(2), 920–941. doi: 10.1093/gji/ggae413

Sepúlveda, I., Haase, J. S., Carvajal, M., Xu, X., & Liu, P. L. F. (2020). Modeling the Sources of the 2018 Palu, Indonesia, Tsunami Using Videos From Social Media. *Journal of Geophysical Research: Solid Earth*, *125*(3), e2019JB018675. doi: 10.1029/2019JB018675

Sepúlveda, I., & Liu, P. L. F. (2016). Estimating tsunami runup with fault plane parameters. *Coastal Engineering*, *112*, 57–68. doi: 10.1016/j.coastaleng.2016.03.001

Sepúlveda, I., Nilsson, B., Yu, Y., Carvajal, M., Brandin, M., Gabriel, A.-A., & Sandwell, D. (2026). SWOT detects dispersive tsunami tied to a near-trench source in the 2025 Kamchatka earthquake. *Science*, *391*(6792), 1368–1372. doi: 10.1126/science.aeb8634

Shen, Z., & Wu, W. (2024). Ocean Bottom Distributed Acoustic Sensing for Oceanic Seismicity Detection and Seismic Ocean Thermometry. *Journal of Geophysical Research: Solid Earth*, *129*(3), e2023JB027799. doi: 10.1029/2023JB027799

Sochacki, J. S., George, J. H., Ewing, R. E., & Smithson, S. B. (1991). Interface conditions for acoustic and elastic wave propagation. *GEOPHYSICS*, *56*(2), 168–181. doi: 10.1190/1.1443029

Sokos, E., Gallovič, F., Evangelidi, C. P., Serpetsidaki, A., Plicka, V., Kostelecký, J., & Zahradník, J. (2020). The 2018 Mw 6.8 Zakynthos, Greece, Earthquake: Dominant Strike-Slip Faulting near Subducting Slab. *Seismological Research Letters*, *91*(2A), 721–732. doi: 10.1785/0220190169

Sokos, E., Zahradník, J., Gallovič, F., Serpetsidaki, A., Plicka, V., & Kiratzi, A. (2016). Asperity break after 12 years: The Mw6.4 2015 Lefkada (Greece) earthquake. *Geophysical Research Letters*, *43*(12), 6137–6145. doi: 10.1002/2016GL069427

Spence, W. (1986). The 1977 Sumba earthquake series: Evidence for Slab pull force acting at a subduction zone. *Journal of Geophysical Research: Solid Earth*, *91*(B7), 7225–7239. doi: 10.1029/JB091iB07p07225

Spudich, P., Guatteri, M., Otsuki, K., & Minagawa, J. (1998). Use of fault striations and dislocation models to infer tectonic shear stress during the 1995 Hyogo-Ken Nanbu (Kobe) earthquake. *Bulletin of the Seismological Society of America*, *88*(2), 413–427. doi: 10.1785/BSSA0880020413

Stiros, S. C. (2001). The AD 365 Crete earthquake and possible seismic clustering during the fourth to sixth centuries AD in the Eastern Mediterranean: A

review of historical and archaeological data. *Journal of Structural Geology*, *23*(2-3), 545–562. doi: 10.1016/S0191-8141(00)00118-8

Stoneley, R. (1924). Elastic waves at the surface of separation of two solids. *Proceedings of the Royal Society of London. Series A, Containing Papers of a Mathematical and Physical Character*, *106*(738), 416–428. doi: 10.1098/rspa.1924.0079

Styron, R., & Pagani, M. (2020). The GEM Global Active Faults Database. *Earthquake Spectra*, *36*(1_suppl), 160–180. doi: 10.1177/8755293020944182

Sun, Y.-S., Melgar, D., Ruiz-Angulo, A., Ganas, A., Taymaz, T., Crowell, B., ... Eken, T. (2024). The 2020 Mw 7.0 Samos (Eastern Aegean Sea) Earthquake: Joint source inversion of multitype data, and tsunami modelling. *Geophysical Journal International*, *237*(3), 1285–1300. doi: 10.1093/gji/ggae082

Talley, L. D., Pickard, G. L., Emery, W. J., & Swift, J. H. (2011). Chapter 8 - Gravity Waves, Tides, and Coastal Oceanography. In L. D. Talley, G. L. Pickard, W. J. Emery, & J. H. Swift (Eds.), *Descriptive Physical Oceanography (Sixth Edition)* (pp. 223–244). Academic Press. doi: 10.1016/B978-0-7506-4552-2.10008-3

Tanioka, Y., & Satake, K. (1996). Tsunami generation by horizontal displacement of ocean bottom. *Geophysical Research Letters*, *23*(8), 861–864. doi: 10.1029/96GL00736

Taufiqurrahman, T., Gabriel, A.-A., Ulrich, T., Valentová, L., & Gallovič, F. (2022). Broadband Dynamic Rupture Modeling With Fractal Fault Roughness, Frictional Heterogeneity, Viscoelasticity and Topography: The 2016 Mw 6.2 Amatrice, Italy Earthquake. *Geophysical Research Letters*, *49*(22), e2022GL098872. doi: 10.1029/2022GL098872

Taymaz, T., Yilmaz, Y., & Dilek, Y. (2007). The geodynamics of the Aegean and Anatolia: Introduction. *Geological Society Special Publication*, *291*, 1–16. doi: 10.1144/SP291.1

Taymaz, T., Yolsal-Çevikbilen, S., Irmak, T. S., Vera, F., Liu, C., Eken, T., ... Keleş, D. (2022). Kinematics of the 30 October 2020 Mw 7.0 Néon Karlovásion (Samos) earthquake in the Eastern Aegean Sea: Implications on source characteristics and dynamic rupture simulations. *Tectonophysics*, *826*, 229223. doi: 10.1016/j.tecto.2022.229223

Tian, D., Fröhlich, Y., Leong, W. J., Grund, M., Schlitzer, W., Jones, M., ... Luis, J. M. F. (2026). PyGMT: Bridging Python and the Generic Mapping Tools for Geospatial Visualization and Analysis. *Geochemistry, Geophysics, Geosystems*, *27*(7), e2026GC013105. doi: 10.1029/2026GC013105

Tinti, E., Casarotti, E., Ulrich, T., Taufiqurrahman, T., Li, D., & Gabriel, A. A. (2021). Constraining families of dynamic models using geological, geodetic and strong ground motion data: The Mw 6.5, October 30th, 2016, Norcia earthquake, Italy. *Earth and Planetary Science Letters*, *576*, 117237. doi: 10.1016/J.EPSL.2021.117237

Tinti, E., Fukuyama, E., Piatanesi, A., & Cocco, M. (2005). A Kinematic Source-Time Function Compatible with Earthquake Dynamics. *Bulletin of the Seismological Society of America*, *95*(4), 1211–1223. doi: 10.1785/0120040177

Tinti, E., Spudich, P., & Cocco, M. (2005). Earthquake fracture energy inferred from kinematic rupture models on extended faults. *Journal of Geophysical Research: Solid Earth*, *110*(B12), 1–25. doi: 10.1029/2005JB003644

Tinti, S., Armigliato, A., Pagnoni, G., & Zaniboni, F. (2005). Scenarios of giant tsunamis of tectonic origin in the Mediterranean. *ISET Journal of Earthquake Technology*, *42*(4), 171–188. doi: 10.63898/EYRV2273

Tonegawa, T., & Araki, E. (2024). High-Frequency Tsunamis Excited Near Torishima Island, Japan, Observed by Distributed Acoustic Sensing. *Geophysical Research Letters*, *51*(11), e2024GL108714. doi: 10.1029/2024GL108714

Triantafyllou, I., Gogou, M., Mavroulis, S., Lekkas, E., Papadopoulos, G. A., &

Thravalos, M. (2021). The Tsunami Caused by the 30 October 2020 Samos (Aegean Sea) Mw7.0 Earthquake: Hydrodynamic Features, Source Properties and Impact Assessment from Post-Event Field Survey and Video Records. *Journal of Marine Science and Engineering*, *9*(1), 68. doi: 10.3390/JMSE9010068

Ulrich, T., Gabriel, A.-A., Ampuero, J.-P., & Xu, W. (2019). Dynamic viability of the 2016 Mw 7.8 Kaikōura earthquake cascade on weak crustal faults. *Nature Communications*, *10*(1), 1213. doi: 10.1038/s41467-019-09125-w

Ulrich, T., Gabriel, A. A., & Madden, E. H. (2022). Stress, rigidity and sediment strength control megathrust earthquake and tsunami dynamics. *Nature Geoscience*, *15*(1), 67–73. doi: 10.1038/s41561-021-00863-5

Ulrich, T., Vater, S., Madden, E. H., Behrens, J., van Dinther, Y., van Zelst, I., ... Gabriel, A. A. (2019). Coupled, Physics-Based Modeling Reveals Earthquake Displacements are Critical to the 2018 Palu, Sulawesi Tsunami. *Pure and Applied Geophysics*, *176*(10), 4069–4109. doi: 10.1007/s00024-019-02290-5

Uphoff, C., Rettenberger, S., Bader, M., Madden, E. H., Ulrich, T., Wollherr, S., & Gabriel, A.-A. (2017). Extreme scale multi-physics simulations of the tsunamigenic 2004 sumatra megathrust earthquake. In *Proceedings of the International Conference for High Performance Computing, Networking, Storage and Analysis* (pp. 1–16). ACM. doi: 10.1145/3126908.3126948

Ursell, F. (1953). The long-wave paradox in the theory of gravity waves. *Mathematical Proceedings of the Cambridge Philosophical Society*, *49*(4), 685–694. doi: 10.1017/S0305004100028887

U.S. Geological Survey. (2020). *M 7.0 - 13 km NNE of Néon Karlovásion, Greece.* https://earthquake.usgs.gov/earthquakes/eventpage/us7000c7y0/executive.

Vinh, P. C. (2013). Scholte-wave velocity formulae. *Wave Motion*, *50*(2), 180–190. doi: 10.1016/j.wavemoti.2012.08.006

Wilcox, L. C., Stadler, G., Burstedde, C., & Ghattas, O. (2010). A high-order discontinuous Galerkin method for wave propagation through coupled elastic–acoustic media. *Journal of Computational Physics*, *229*(24), 9373–9396. doi: 10.1016/j.jcp.2010.09.008

Wilson, A., & Ma, S. (2021). Wedge Plasticity and Fully Coupled Simulations of Dynamic Rupture and Tsunami in the Cascadia Subduction Zone. *Journal of Geophysical Research: Solid Earth*, *126*(7), e2020JB021627. doi: 10.1029/2020JB021627

Wirp, S. A., Gabriel, A. A., Schmeller, M., H. Madden, E., van Zelst, I., Krenz, L., ... Rannabauer, L. (2021). 3D Linked Subduction, Dynamic Rupture, Tsunami, and Inundation Modeling: Dynamic Effects of Supershear and Tsunami Earthquakes, Hypocenter Location, and Shallow Fault Slip. *Frontiers in Earth Science*, *9*, 177. doi: 10.3389/feart.2021.626844

Wirp, S. A., Kutschera, F., Ulrich, T., Bader, M., Lorito, S., & Gabriel, A. A. (2026). Hellenic Arc tsunami generation from Mw 8+ 3-D margin-wide dynamic rupture earthquake scenarios. *Geophysical Journal International*, *246*(3), ggag181. doi: 10.1093/gji/ggag181

Wong, J. W. C., Fan, W., & Gabriel, A.-A. (2024). A Quantitative Comparison and Validation of Finite-Fault Models: The 2011 Tohoku-Oki Earthquake. *Journal of Geophysical Research: Solid Earth*, *129*(10), e2024JB029212. doi: 10.1029/2024JB029212

Wu, W., Shen, Z., Peng, S., Zhan, Z., & Callies, J. (2023). Seismic Ocean Thermometry Using CTBTO Hydrophones. *Journal of Geophysical Research: Solid Earth*, *128*(9), e2023JB026687. doi: 10.1029/2023JB026687

Xiao, H., Spica, Z. J., Li, J., & Zhan, Z. (2024). Detection of Earthquake Infragravity and Tsunami Waves With Underwater Distributed Acoustic Sensing. *Geophysical Research Letters*, *51*(2), e2023GL106767. doi: 10.1029/2023GL106767

1911 Yolsal-Çevikbilen, S., & Taymaz, T. (2012). Earthquake source parameters along the
1912 Hellenic subduction zone and numerical simulations of historical tsunamis
1913 in the Eastern Mediterranean. *Tectonophysics*, *536–537*, 61–100. doi:
1914 10.1016/J.TECTO.2012.02.019
1915 Zheng, Y., Fang, X., Liu, J., & Fehler, M. C. (2013). *Scholte waves generated by*
1916 *seafloor topography* (No. arXiv:1306.4383). arXiv. doi: 10.48550/arXiv.1306
1917 .4383

This is a non-peer reviewed preprint submitted to *EarthArXiv*

Supporting Information for "Source Representation and Earthquake-Ocean Coupling in Tsunami Generation by the 2020 Samos Normal-Faulting Earthquake"

Fabian Kutschera[1], Alice-Agnes Gabriel[1,2]

[1]Institute of Geophysics and Planetary Physics, Scripps Institution of Oceanography, University of California San Diego, La Jolla, CA, USA

[2]Department of Earth and Environmental Sciences, Ludwig-Maximilians-Universität München, Munich, Germany

Table of Contents

- Captions for Movies S1 to S5 (files uploaded separately)
- Text S1
- Figures S1 to S16

Movie S1. Slip rates for Dynamic Rupture Models B & C, which show how each of the ruptures evolves spontaneously, both with an initial bilateral rupture propagation, followed by an up-dip propagation with surface-breaking slip, before the ruptures continue to break unilaterally to the west until they arrest. The gray contours are the 3 s isochrones of the rupture time.

Movie S2. Tsunami generation comparison for the first 360 s using Kinematic Rupture Model A as a time-dependent source for 3D fully coupled (top row) and 2D non-linear shallow water equation (middle row) modeling, together with their difference (bottom row). Here, the sea surface height anomaly (ssha) has been masked for bathymetry deeper than 100 m and processed with a 2D spatial Butterworth low-pass filter using a cut-off wavelength $\lambda_c = 2$ km. Annotations in the lower-left corner indicate the conditional mean ssha of the most extreme 0.1% of wave crests and troughs. In the bottom row, these metrics are calculated from the difference field between the fully coupled and one-way linked simulations.

Movie S3. Tsunami generation comparison for the first 360 s using Dynamic Rupture Model B as a time-dependent source for 3D fully coupled (top row) and 2D non-linear shallow water equation (middle row) modeling, together with their difference (bottom row). Here, the sea surface height anomaly (ssha) has been masked for bathymetry deeper than 100 m and processed with a 2D spatial Butterworth low-pass filter using a cut-off wavelength $\lambda_c = 2$ km. Annotations in the lower-left corner indicate the conditional mean ssha of the most extreme 0.1% of wave crests and troughs. In the bottom row, these metrics are calculated from the difference field between the fully coupled and one-way linked simulations.

Movie S4. Tsunami generation comparison for the first 360 s using Dynamic Rupture Model C as a time-dependent source for 3D fully coupled (top row) and 2D non-linear shallow water equation (middle row) modeling, together with their difference (bottom row). Here, the sea surface height anomaly (ssha) has been masked for bathymetry deeper than 100 m and processed with a 2D spatial Butterworth low-pass filter using a cut-off wavelength $\lambda_c = 2$ km. Annotations in the lower-left corner indicate the conditional mean ssha of the most extreme 0.1% of wave crests and troughs. In the bottom row, these metrics are calculated from the difference field between the fully coupled and one-way linked simulations.

Movie S5. Tsunami generation for the first 360 s using the Okada Model as an instantaneous source to inform 2D non-linear shallow water equation tsunami modeling. Here, the sea surface height anomaly (ssha) has been masked for bathymetry deeper than 100 m and processed with a 2D spatial Butterworth low-pass filter using a cut-off wavelength $\lambda_c = 2$ km. Annotations in the lower-left corner indicate the conditional mean ssha of the most extreme 0.1% of wave crests and troughs.

Text S1: Data processing and spectral analysis

For a consistent comparison of the initial tsunami generation between the hydrodynamic output of GeoClaw and the sea surface output of SeisSol (Section 3.2), we spatially clip the GeoClaw fixed grid output to the geographic extent of the SeisSol water layer, only retaining water-covered ("wet") cells. We evaluate the SeisSol sea surface output at element centroids, project it into geographic coordinates, and interpolate it onto the clipped GeoClaw grid using a two-dimensional nearest-neighbor interpolator. Although linear interpolation can also be performed, it yields virtually identical results.

To analyze the spatio-temporal characteristics of the simulated sea surface wavefield, we compute the two-dimensional frequency–wavenumber (f–k) spectrum from the space-time data, for which we place densely spaced synthetic receivers (distance of 25 m) along two north–south trending profiles (Fig. S3). The input wavefield, defined on this regular temporal and spatial grid, is first windowed along the spatial dimension using a Hann taper to reduce spectral leakage in the wavenumber domain. A two-dimensional fast Fourier transform (FFT) is then applied to the windowed data to convert it from the time–space domain into the f-k domain. Following the FFT, the zero-frequency and zero-wavenumber components are shifted to the center of the spectrum. The resulting spectra are converted to amplitude, normalized by their maximum value, and expressed in decibels. We consider only positive temporal frequencies and amplitudes down to –80 dB to suppress numerical noise.

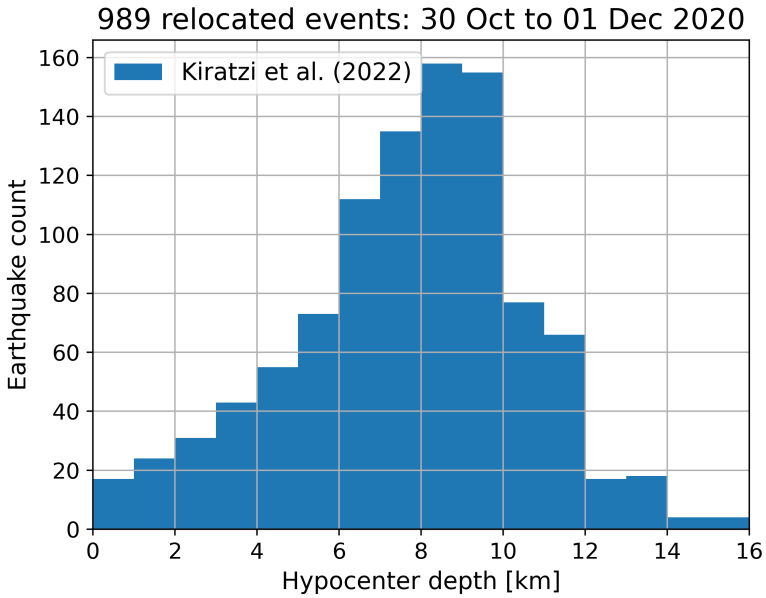


Figure S1. Histogram of aftershock occurrence versus hypocenter depth, showing that about 81.2% of events are concentrated at shallow depths (< 10 km), with 57.5% between 6 and 10 km. This dataset by Kiratzi et al. (2022) includes nearly 1,000 relocated events, covering the period from 30 October to 1 December 2020.

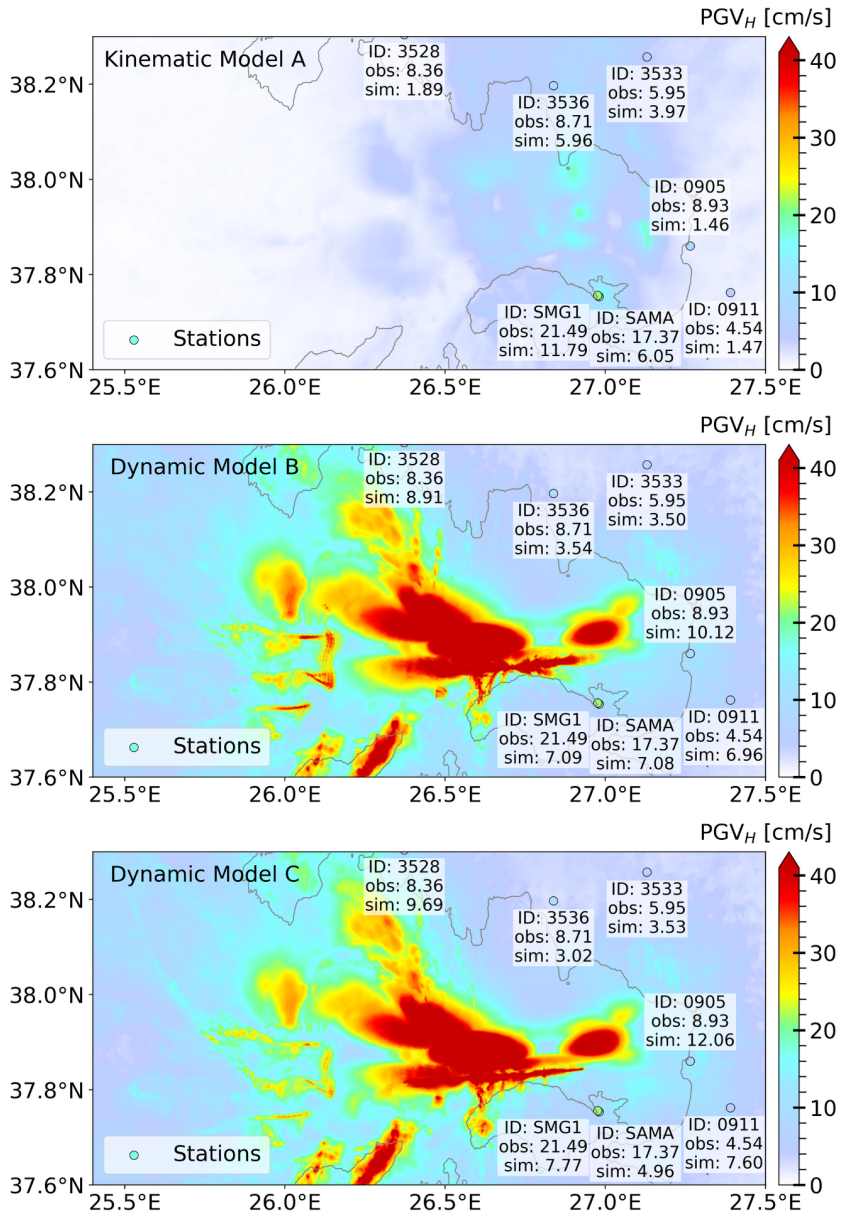


Figure S2. Comparison of horizontal peak ground velocities (PGV_H) for Kinematic Rupture Model A and the two Dynamic Rupture Models B & C, evaluated against observations from Askan et al. (2021) at the seven stations close to the coast (i.e., near the water layer).

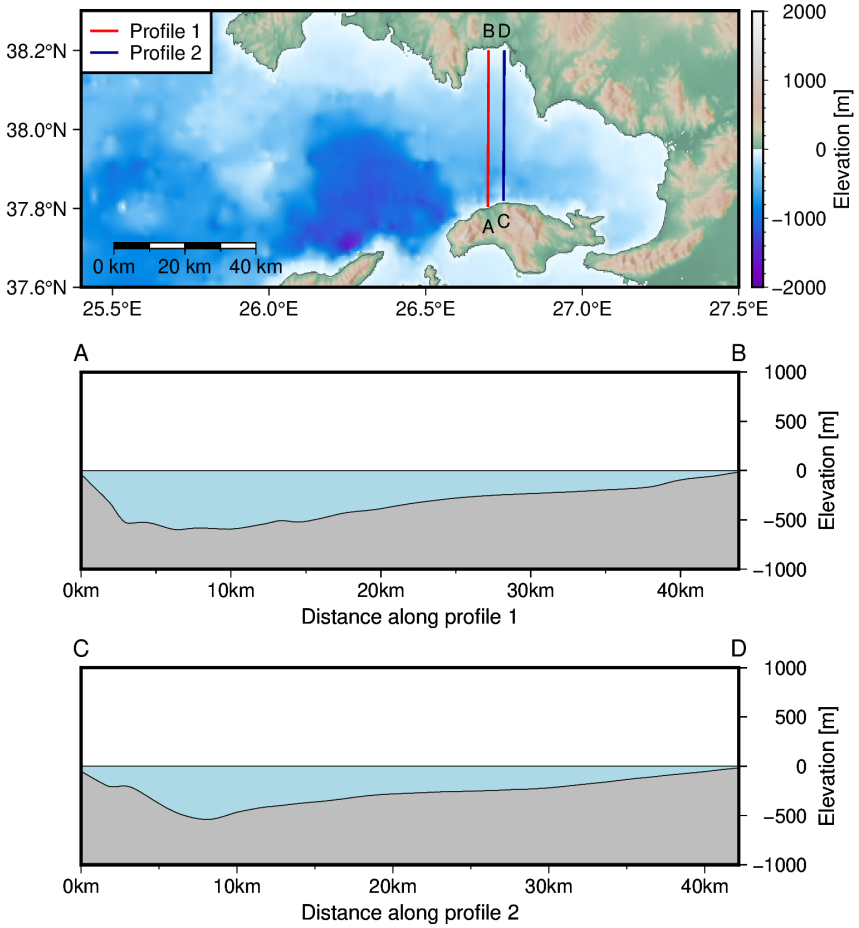


Figure S3. Gridded bathymetry data (GEBCO Bathymetric Compilation Group, 2022) for the seafloor surrounding Samos Island, with the north–south bathymetry profiles along A–B (Profile 1; same as Fig. 1b) and C–D (Profile 2) depicted below.

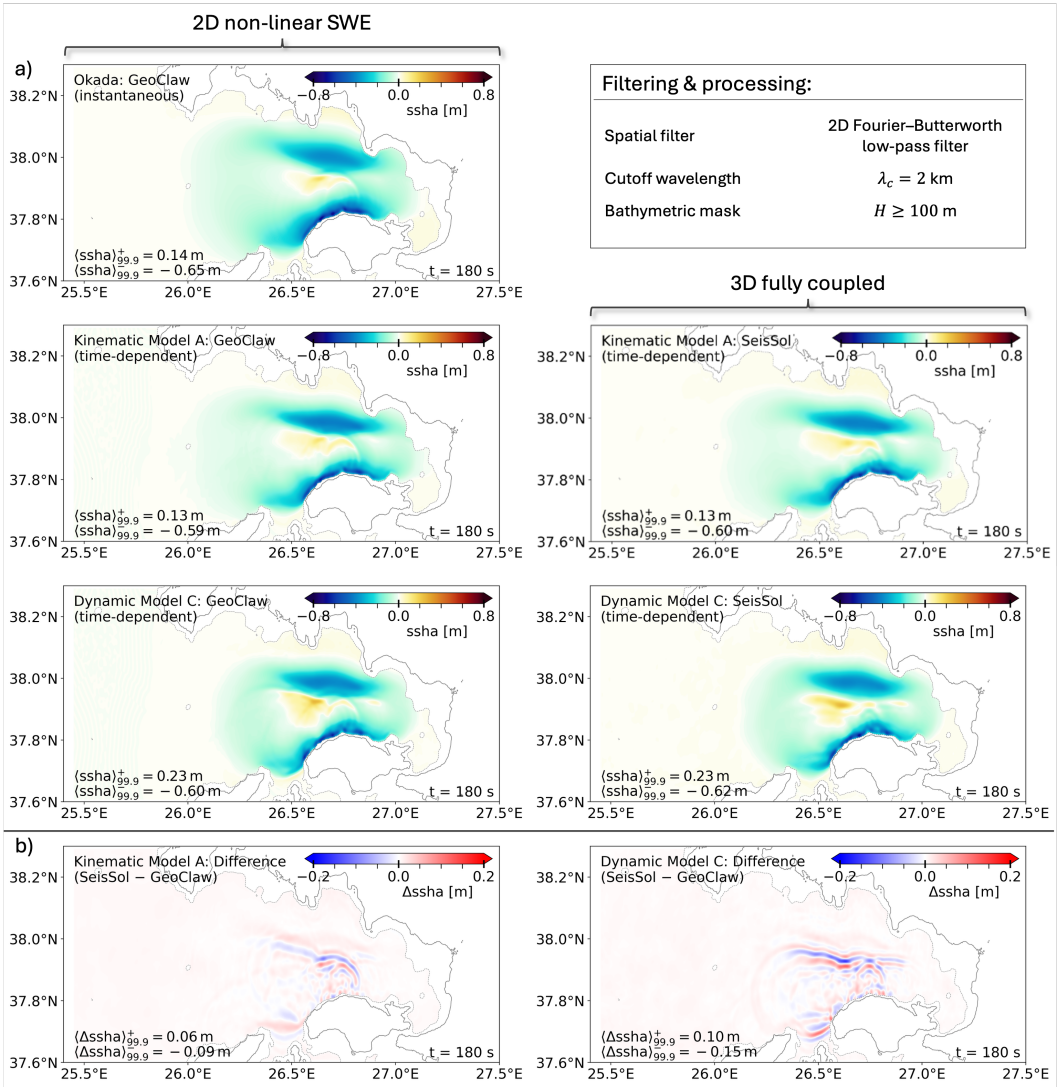


Figure S4. a) Similar to Fig. 6, but with snapshots of tsunami generation after 3 min. First column: three models of the tsunami using the non-linear shallow water equation (SWE) solver GeoClaw (Berger et al., 2011), informed by the instantaneous Okada displacement (Okada, 1985), and the time-dependent seafloor displacements of the Kinematic Rupture Model A and Dynamic Rupture Model C. Second column: fully coupled (3D time-dependent) tsunami generation with SeisSol (Gabriel et al., 2025) from the Kinematic Rupture Model A and the Dynamic Rupture Model C. Snapshots of the tsunami as generated by the Dynamic Rupture Model B are shown in Fig. S5. Annotations in the lower-left corner indicate the conditional mean sea surface height anomaly (ssha) of the most extreme 0.1% of wave crests and troughs. b) Differences in the generated tsunamis after 3 min between fully coupled (SeisSol) and one-way linked (GeoClaw) simulations of the same rupture models. Here, ssha metrics are calculated from the difference field between the fully coupled and one-way linked simulations.

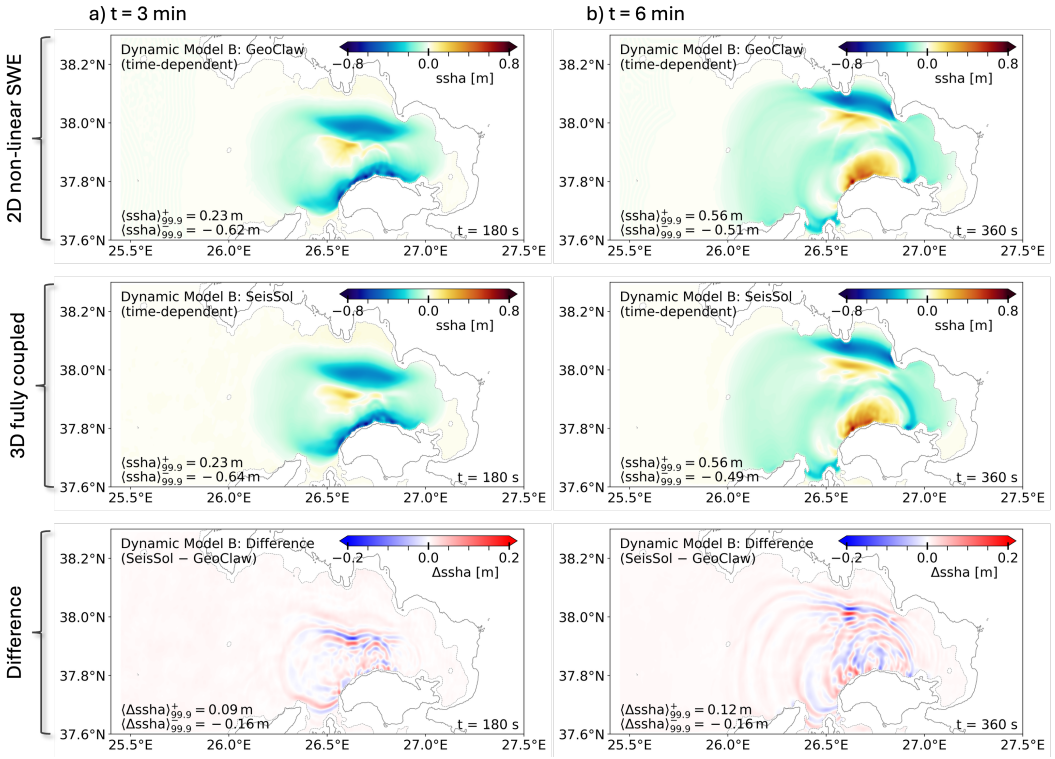


Figure S5. Snapshots of the tsunami generation following Dynamic Rupture Model B using the non-linear shallow water equation (SWE) solver GeoClaw (Berger et al., 2011), SeisSol (Gabriel et al., 2025), and their difference for a) 3 min and b) 6 min of simulated time. Each is masked by bathymetry deeper than 100 m and processed with a 2D spatial Butterworth low-pass filter using a cut-off wavelength $\lambda_c = 2$ km. Annotations in the lower-left corner indicate the conditional mean ssha of the most extreme 0.1% of wave crests and troughs. In the bottom row, these metrics are calculated from the difference field between the fully coupled and one-way linked simulations.

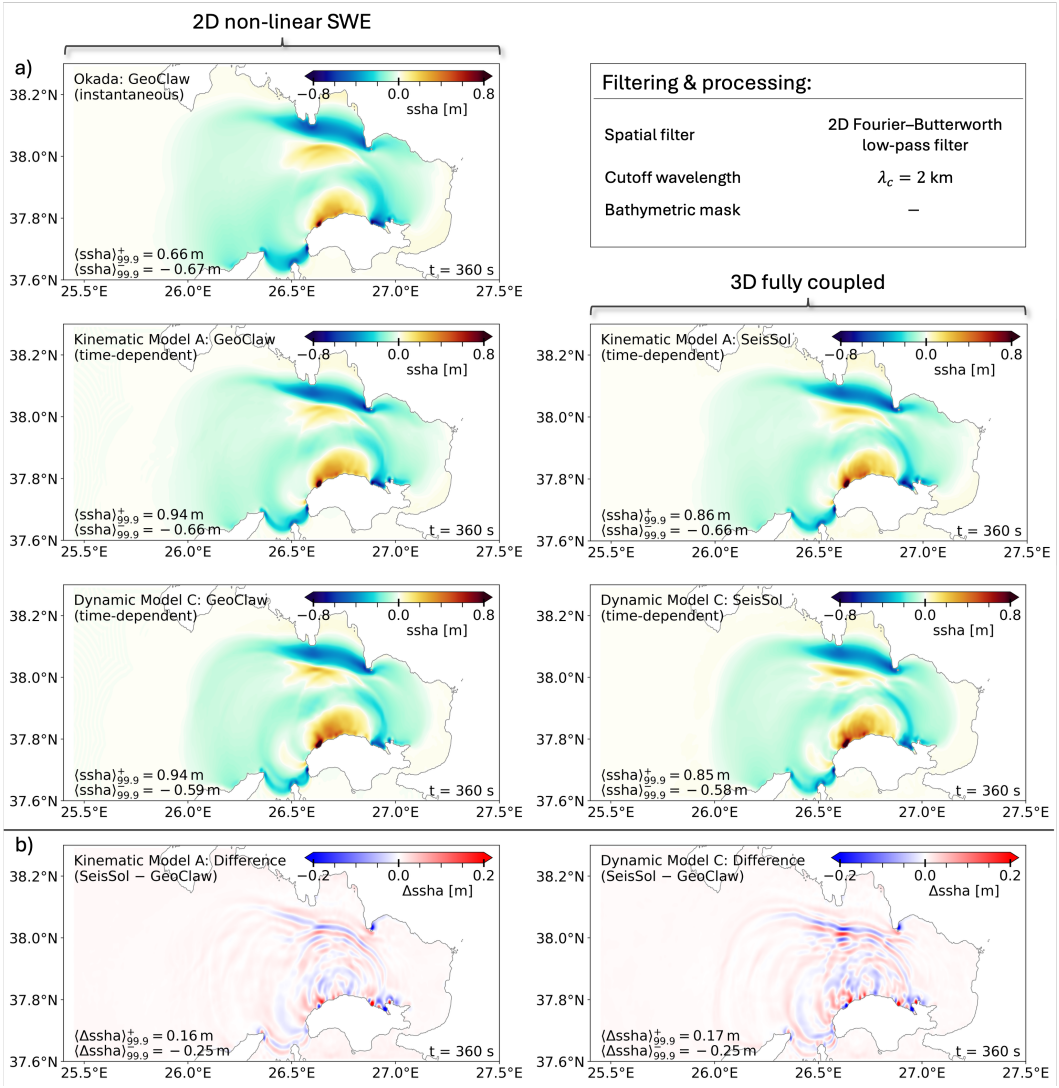


Figure S6. a) Snapshots of tsunami generation after 6 min without bathymetry masking and processed with a 2D spatial Butterworth low-pass filter using a cut-off wavelength $\lambda_c = 2$ km. First column: three models of the tsunami using the non-linear shallow water equation (SWE) solver GeoClaw (Berger et al., 2011), informed by the instantaneous Okada displacement (Okada, 1985), and the time-dependent seafloor displacements of the Kinematic Rupture Model A and Dynamic Rupture Model C. Second column: fully coupled (3D time-dependent) tsunami generation with SeisSol (Gabriel et al., 2025) from the Kinematic Rupture Model A and the Dynamic Rupture Model C. Snapshots of the tsunami as generated by the Dynamic Rupture Model B are shown in Fig. S5. Annotations in the lower-left corner indicate the conditional mean sea surface height anomaly (ssha) of the most extreme 0.1% of wave crests and troughs. b) Differences in the generated tsunamis after 6 min between fully coupled (SeisSol) and one-way linked (GeoClaw) simulations of the same rupture models. Here, ssha metrics are calculated from the difference field between the fully coupled and one-way linked simulations.

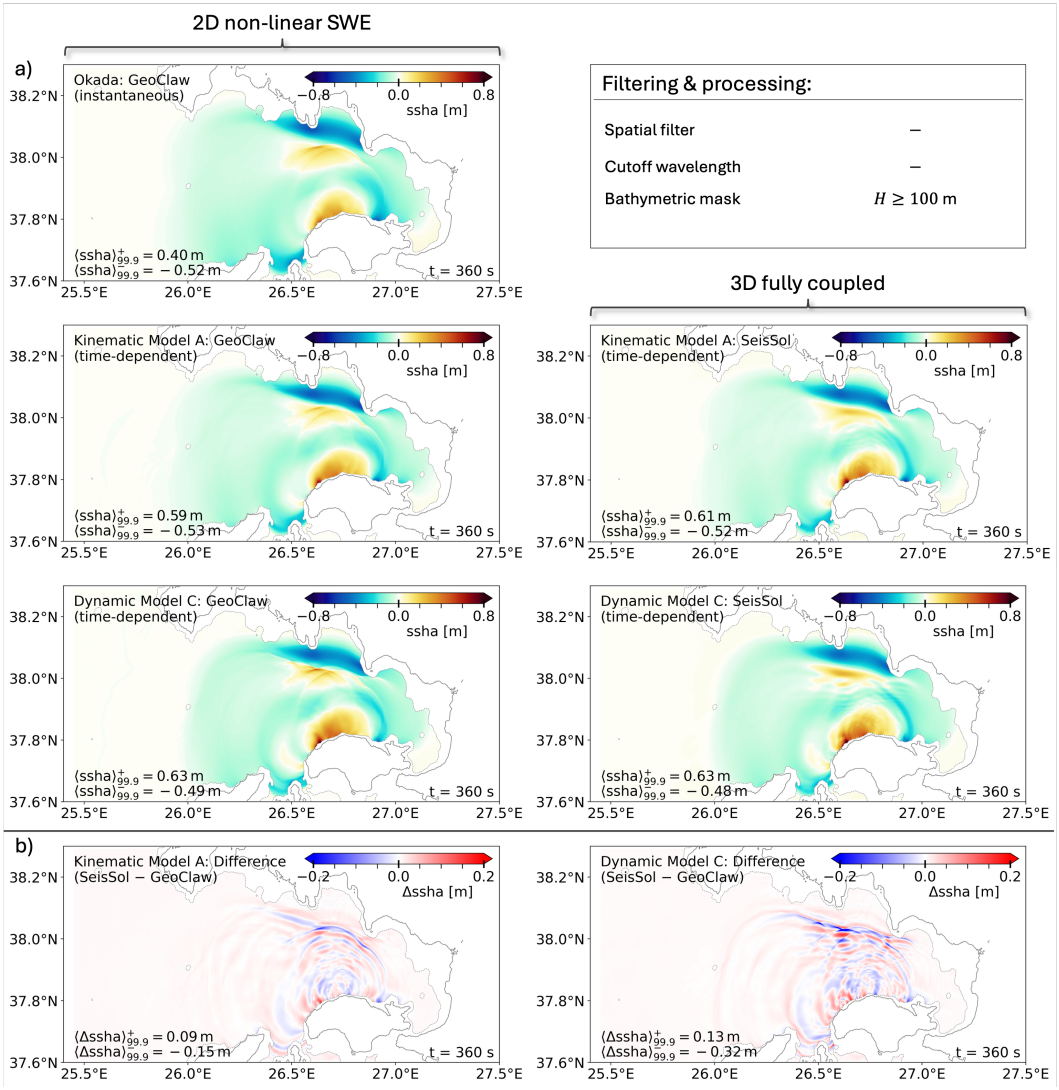


Figure S7. a) Snapshots of tsunami generation after 6 min, masked by bathymetry deeper than 100 m and no additional filter applied. First column: three models of the tsunami using the non-linear shallow water equation (SWE) solver GeoClaw (Berger et al., 2011), informed by the instantaneous Okada displacement (Okada, 1985), and the time-dependent seafloor displacements of the Kinematic Rupture Model A and Dynamic Rupture Model C. Second column: fully coupled (3D time-dependent) tsunami generation with SeisSol (Gabriel et al., 2025) from the Kinematic Rupture Model A and the Dynamic Rupture Model C. Snapshots of the tsunami as generated by the Dynamic Rupture Model B are shown in Fig. S5. Annotations in the lower-left corner indicate the conditional mean sea surface height anomaly (ssha) of the most extreme 0.1% of wave crests and troughs. b) Differences in the generated tsunamis after 6 min between fully coupled (SeisSol) and one-way linked (GeoClaw) simulations of the same rupture models. Here, ssha metrics are calculated from the difference field between the fully coupled and one-way linked simulations.

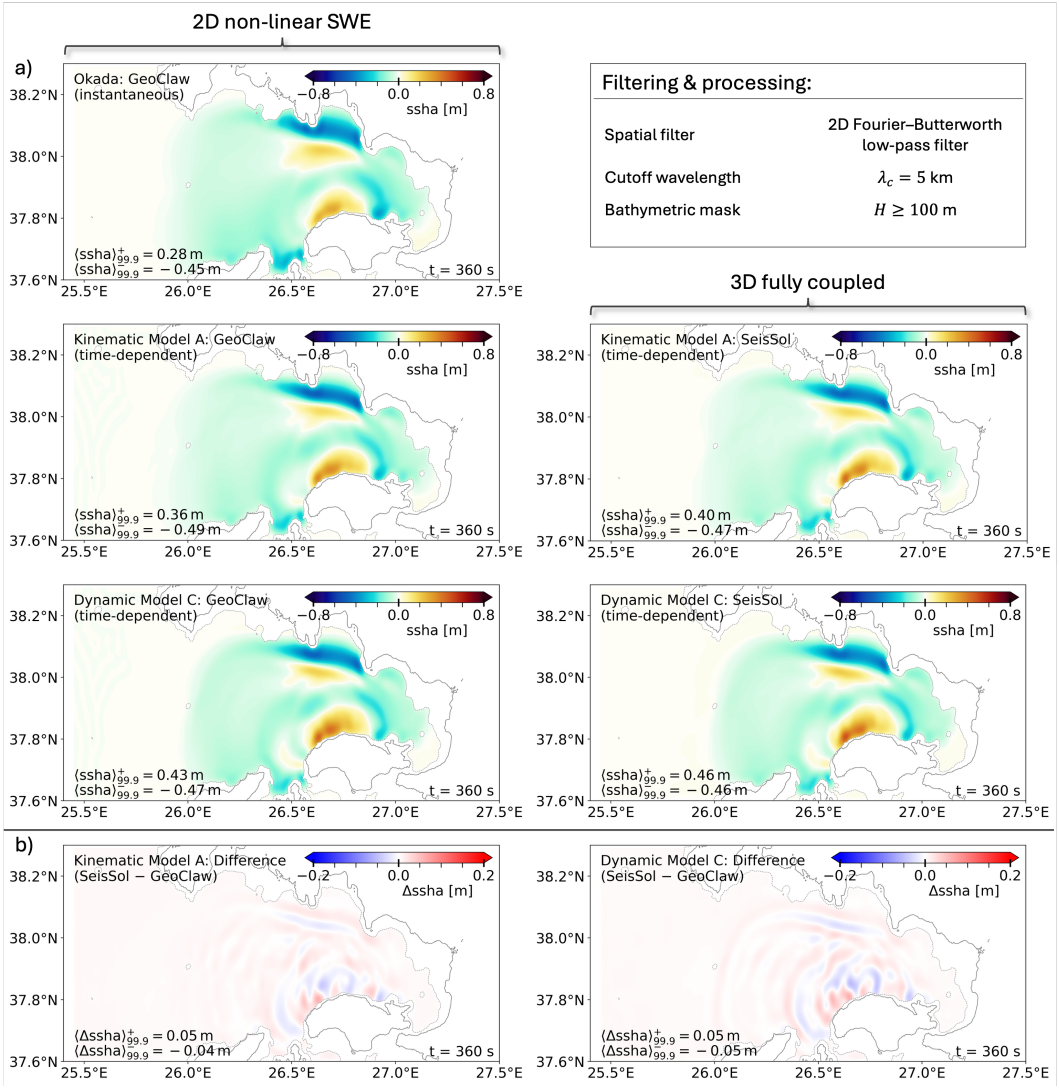


Figure S8. a) Snapshots of tsunami generation after 6 min, masked by bathymetry deeper than 100 m and processed with a 2D spatial Butterworth low-pass filter using a cut-off wavelength $\lambda_c = 5$ km. First column: three models of the tsunami using the non-linear shallow water equation (SWE) solver GeoClaw (Berger et al., 2011), informed by the instantaneous Okada displacement (Okada, 1985), and the time-dependent seafloor displacements of the Kinematic Rupture Model A and Dynamic Rupture Model C. Second column: fully coupled (3D time-dependent) tsunami generation with SeisSol (Gabriel et al., 2025) from the Kinematic Rupture Model A and the Dynamic Rupture Model C. Snapshots of the tsunami as generated by the Dynamic Rupture Model B are shown in Fig. S5. Annotations in the lower-left corner indicate the conditional mean sea surface height anomaly (ssha) of the most extreme 0.1% of wave crests and troughs. b) Differences in the generated tsunamis after 6 min between fully coupled (SeisSol) and one-way linked (GeoClaw) simulations of the same rupture models. Here, ssha metrics are calculated from the difference field between the fully coupled and one-way linked simulations.

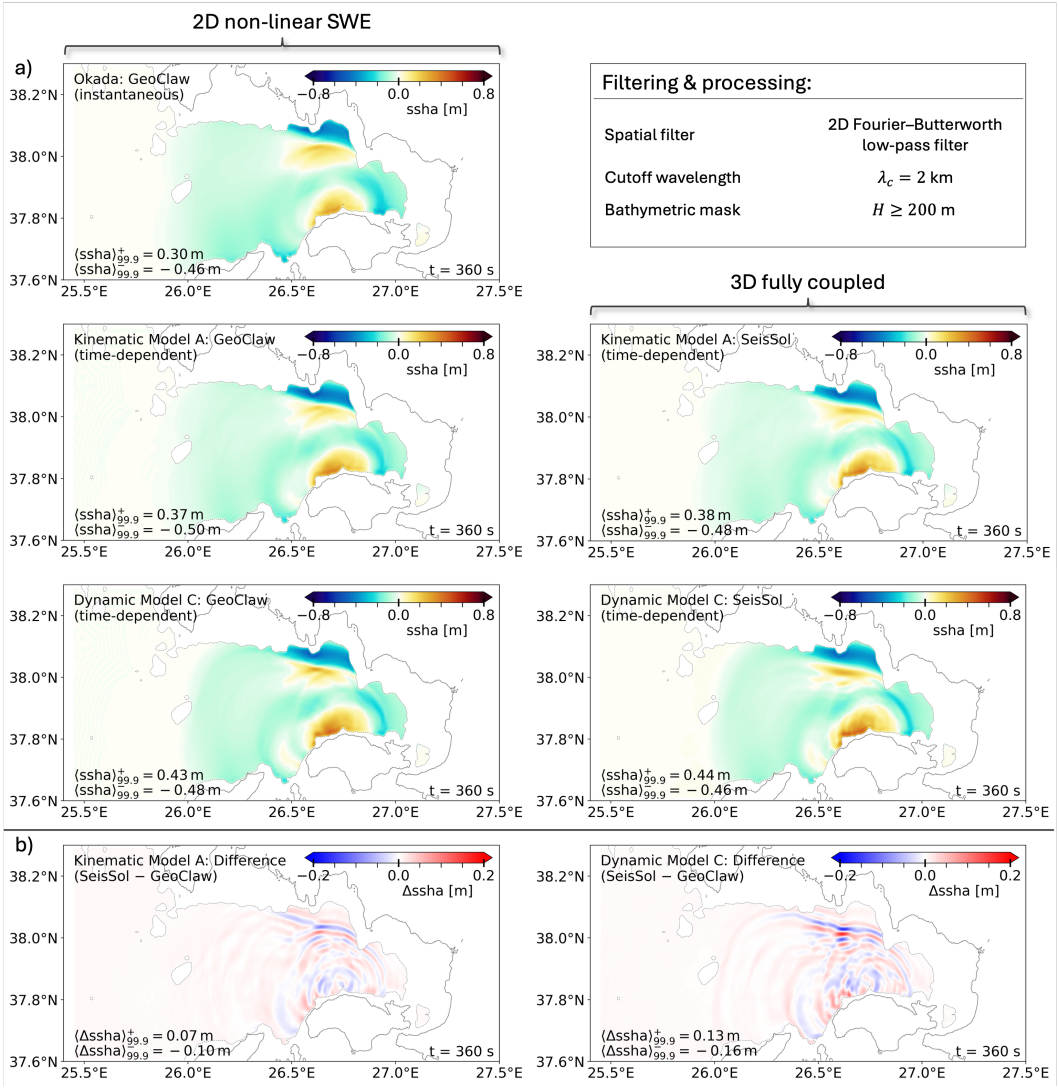


Figure S9. a) Snapshots of tsunami generation after 6 min, masked by bathymetry deeper than 200 m and processed with a 2D spatial Butterworth low-pass filter using a cut-off wavelength $\lambda_c = 2$ km. First column: three models of the tsunami using the non-linear shallow water equation (SWE) solver GeoClaw (Berger et al., 2011), informed by the instantaneous Okada displacement (Okada, 1985), and the time-dependent seafloor displacements of the Kinematic Rupture Model A and Dynamic Rupture Model C. Second column: fully coupled (3D time-dependent) tsunami generation with SeisSol (Gabriel et al., 2025) from the Kinematic Rupture Model A and the Dynamic Rupture Model C. Snapshots of the tsunami as generated by the Dynamic Rupture Model B are shown in Fig. S5. Annotations in the lower-left corner indicate the conditional mean sea surface height anomaly (ssha) of the most extreme 0.1% of wave crests and troughs. b) Differences in the generated tsunamis after 6 min between fully coupled (SeisSol) and one-way linked (GeoClaw) simulations of the same rupture models. Here, ssha metrics are calculated from the difference field between the fully coupled and one-way linked simulations.

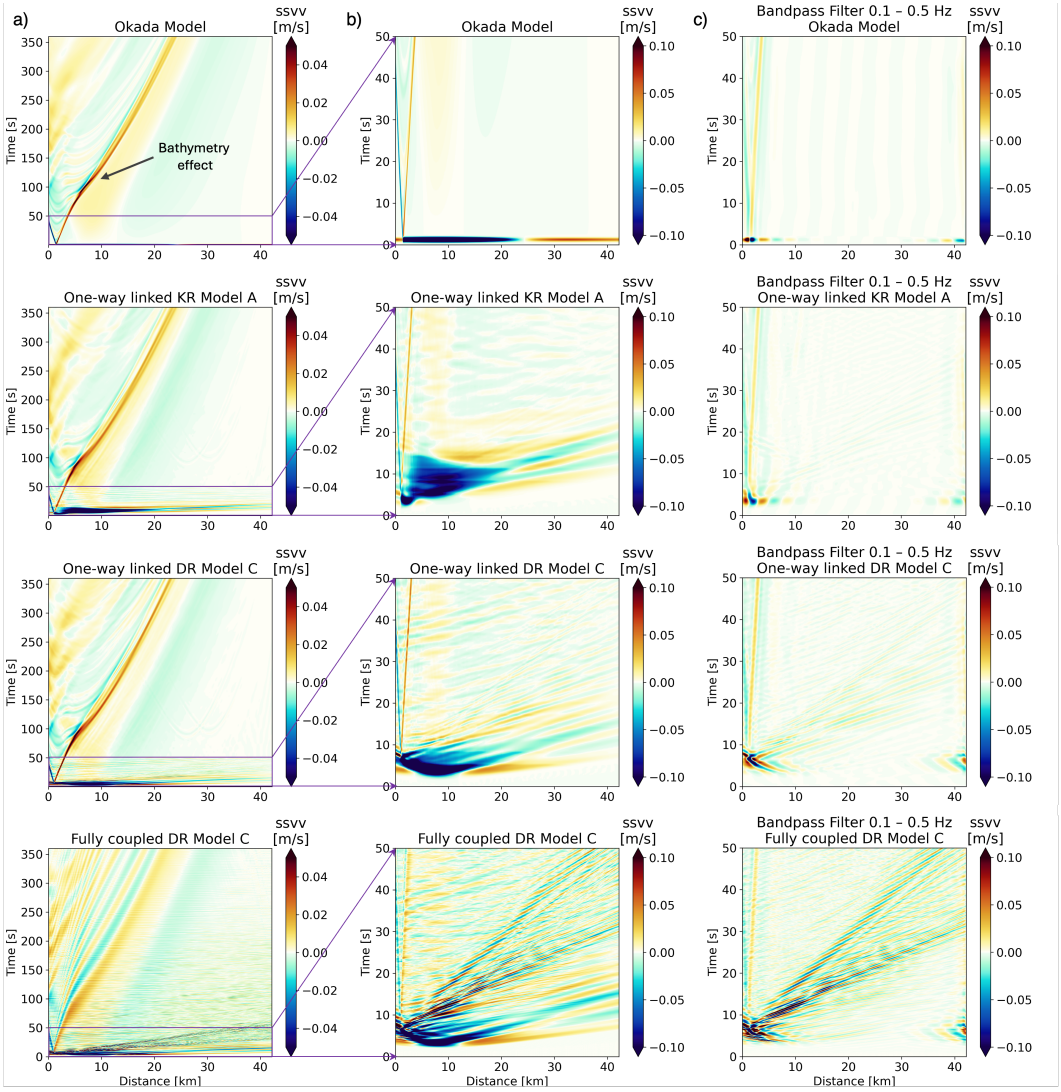


Figure S10. Similar to Fig. 9, but showing the space-time evolution of the tsunami generation along Profile 2 (see Fig. S3) for a) the first 6 min of simulation time, focusing on the tsunami (gravity wave) front. Note the curvature in the tsunami front due to a local bathymetry change. b) The first 50 s highlight the additional complexity of seismo-acoustic waves present in fully coupled models. Recall that the first 50 s of simulated time from the Kinematic Rupture (KR) Model A and Dynamic Rupture (DR) Model C are also used for the time-dependent sourcing of the one-way linked GeoClaw simulations, whereas the fully coupled simulations are inherently time-dependent. c) Same scale as b), but with a bandpass filter of 0.1–0.5 Hz applied, highlighting signals consistent with dispersive Scholte waves in the fully coupled simulation. Ocean acoustic modes are not clearly distinguishable in this frequency band.

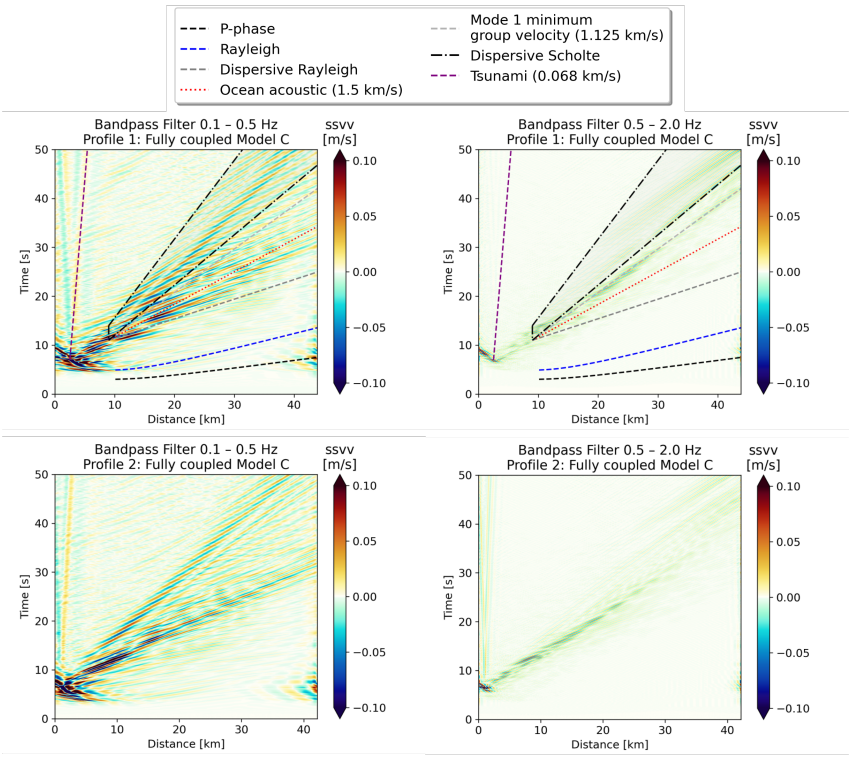


Figure S11. Bandpass-filtered space-time evolutions along Profile 1 (first row) and Profile 2 (second row). The first column shows the filtered signals between 0.1–0.5 Hz (same as in Figs. 9, S10), highlighting signals consistent with dispersive Scholte waves in the fully coupled simulation. The second column shows the filtered signals between 0.5–2.0 Hz, where the signature associated with the minimum group velocity of ocean acoustic mode 1 is more apparent.

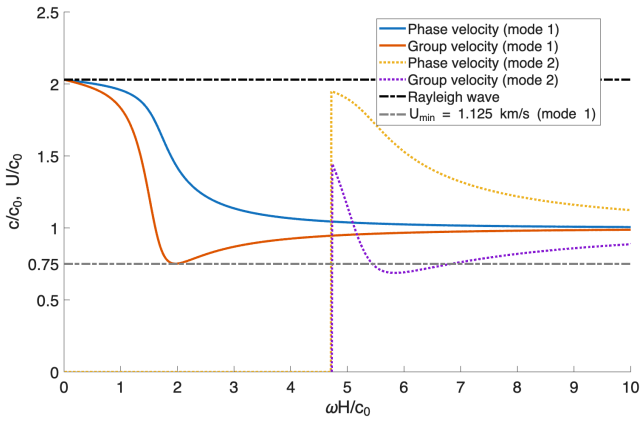


Figure S12. Phase (c) and group velocity (U), calculated following Abrahams et al. (2023), each normalized by the ocean sound speed $c_0 = 1500$ m s^{-1}, for the first two ocean acoustic modes as a function of non-dimensional angular frequency $\omega H/c_0$, where we assume an average ocean depth of 334.47 m along the full length of Profile 1. A density of $\rho = 1025$ kg m^{-3} (see Section 2.5.1), shear modulus $\mu = 0$ Pa, and 1st Lamé parameter $\lambda = 2306250000$ Pa are assumed for the overlying water (acoustic medium). We use the thickness-weighted average material parameters from the upper four layers (to a depth of 16 km) of the used velocity model (Novotný et al., 2001; Plicka et al., 2022) for the underlying solid Earth (elastic medium): $\rho = 3168$ kg m^{-3}, $\mu = 34505875000$ Pa, $\lambda = 40323095625$ Pa.

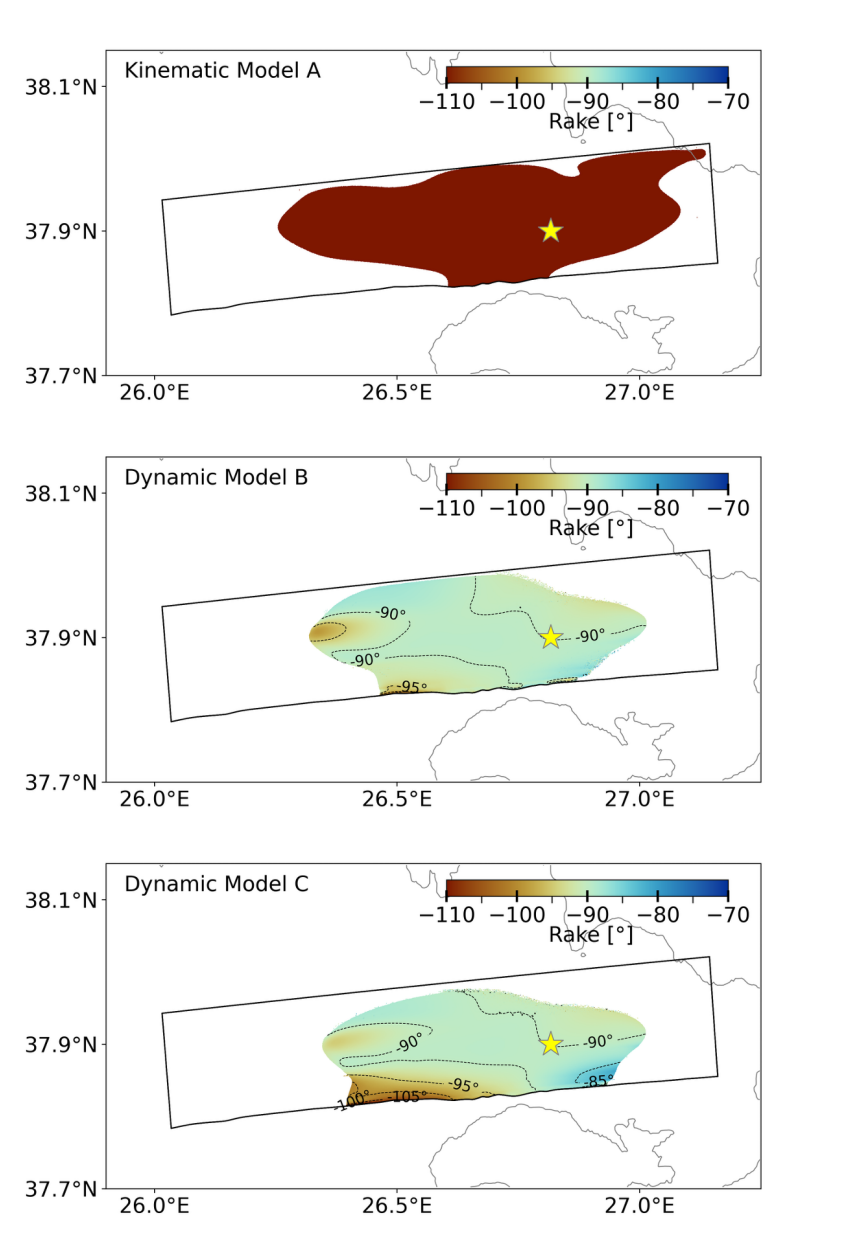


Figure S13. Rake at the end of the rupture simulations. Kinematic Rupture Model A has a constant rake of -110°, consistent with the reference finite-fault slip model of Plicka et al. (2022). Although the two dynamic rupture models prescribe pure normal faulting (rake of -90°), they exhibit dynamic rake rotation that introduces minor secondary strike-slip motion. This effect is more pronounced near the surface for Dynamic Rupture Model C with the depth-dependent initial effective normal stress setup. Note that here we consider only those parts of the fault where the final slip of the respective model exceeded 0.2 m.

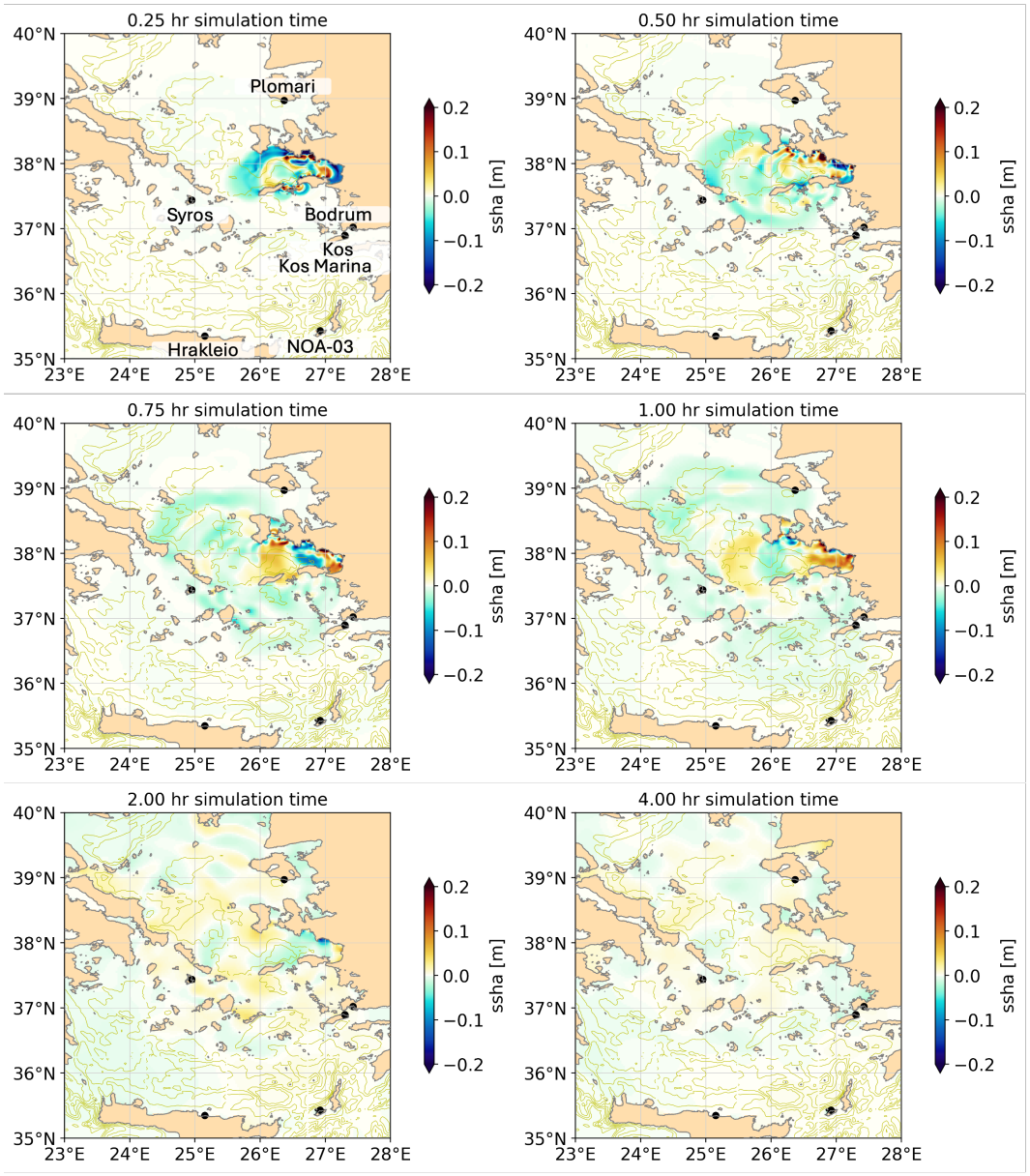


Figure S14. Snapshots of the tsunami propagation from the one-way linked Dynamic Rupture Model C across the entire Aegean Sea with tide gauges marked as black dots. Contour lines represent the bathymetry at 500 m levels.

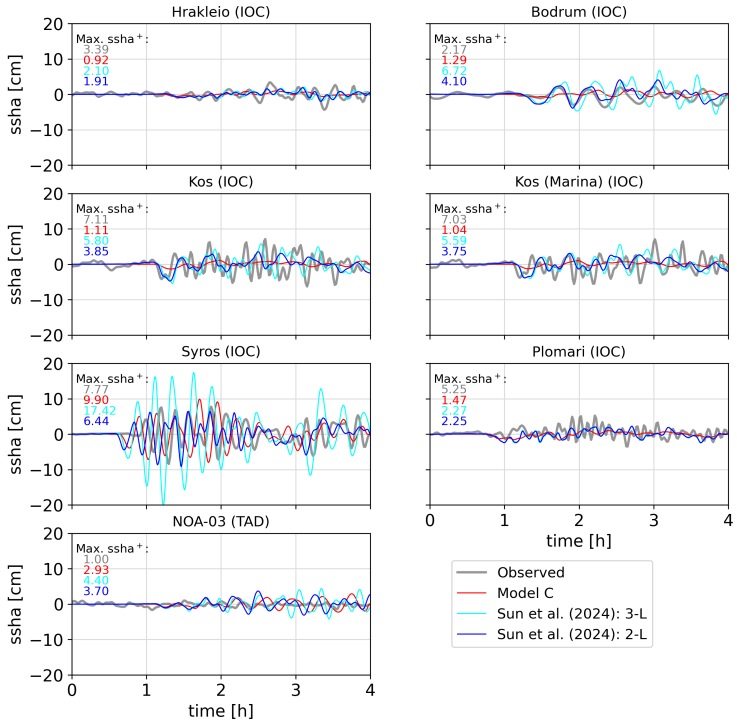


Figure S15. Simulated tsunami waveforms from the one-way linked Dynamic Rupture Model C (with 300 s low-pass filter, although of negligible influence) and from Sun et al. (2024) (for two different levels of bathymetric resolution) together with the de-tided (Section 2.5.2), observed waveforms at far-field tide gauges. Annotated on the left is the respective maximum (positive) sea surface height anomaly (ssha) amplitude.

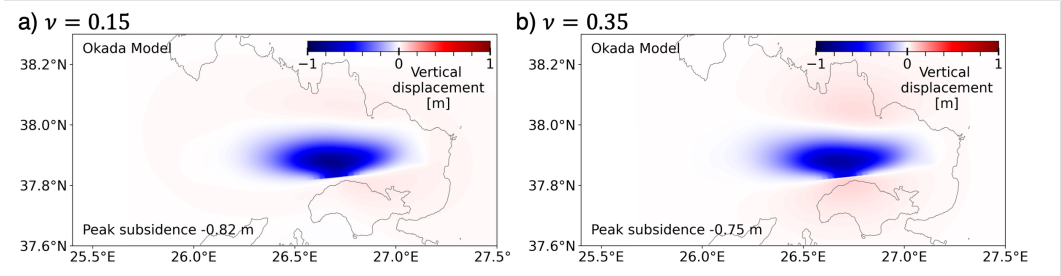


Figure S16. Sensitivity test of the Okada (Okada, 1985) approach as applied to the finite-fault model of Plicka et al. (2022) for Poisson's ratios ν of a) 0.15 and b) 0.35.